Eindhoven University of Technology

MASTER

Chassis and suspension design FSRTE02

van Berkum, A.

Award date:
2006

Link to publication

Chassis and suspension design FSRTE02

A. van Berkum

DCT 2006.23

Master's Thesis

Coach: Dr.ir. P.C.J.N. Rosielle
Supervisor: Prof.dr.ir. M. Steinbuch

Technische Universiteit Eindhoven
Department of Mechanical Engineering
Section Dynamics and Control Technology

Eindhoven, March 2006

Dutch summary

Achtergrond informatie
De Formula Student competitie is een competitie waaraan universiteiten vanuit de hele wereld deelnemen. In 2004 heeft het Formula Student Racing Team Eindhoven (FSRTE) voor het eerst deelgenomen in klasse 3. In deze klasse wordt het ontwerp beoordeeld. In 2005 heeft het FSRTE voor de 2^e keer meegedaan en dit keer in klasse 2 met een onafgebouwde wagen. Het doel voor 2006 is om deel te nemen met een rijdende auto in klasse 1. In deze klasse kan daadwerkelijk worden geraced met de zelfgebouwde eenzitter. Het maximale vermnogen ligt hierbij op 65 kW.

Opdracht
Het doel van de race is om studenten te leren om een raceteam op te zetten dat in staat is om een auto te ontwerpen, te bouwen en er uiteindelijk ook mee te kunnen racen.
Het team moet zich voorstellen dat ze een prototype moeten bouwen voor een bedrijf. Uiteindelijk wil het bedrijf 1000 auto's per jaar gaan maken voor de niet-professionele weekend courour. De auto mag niet meer dan €21.000 gaan kosten, maar tegelijkertijd moeten de prestaties en wegligging goed zijn. De uitdaging is om hier zo goed mogelijk aan te voldoen.

Doel
Het doel van dit project is om het ontwerp voor het chassis en de wielophanging van de FSRTE02 te maken, dat zo goed mogelijk voldoet aan de gestelde eisen.
Ook moet er een assemblage van de complete auto worden gemaakt in Unigraphics.

Conclusies
Het FSRTE02 chassis is grotendeels gebaseerd op het FSRTE01 chassis maar is geoptimaliseerd naar torsie strijfheid. De wielophangings eigenschappen zijn bepaald voor een goede wegligging. Het chassis is gemaakt van ALUCORE aluminium honingraat panelen. De delen zijn waterstraal gesneden en gebogen waarna ze aan elkaar gelijmd zijn. De dunne aluminium platen in het chassis zijn gesneden met laser voor een hoge presicie. De voorste en achterste rol beugels zijn buitenom geplaatst en van binnenuit bevestigd.Het dashboard is een sandwich structuur met een polyurethaan kern. De stuuroverbrenging is verzonken in het dashbord. Bij het ontwerp van de bevestigingspunten van de wielophanging is rekening gehouden met de maakbaarheid. De aandrijving wordt verzorgd door een 600 cc Suzuki motorblok dat via een ketting de achterwielen aandrijft. Voor het veerssysteem worden twee enkele veerdempers gebruikt. Spiraalveren zorgen voor de roll stijfheid en twee motorfiets stuurdempers worden gebruikt voor de roll demping. Alle onderdelen van het veersysteem en het anti-roll systeem zitten ingebouwd in een rechthoekige aliminium koker, "de suspension box".

Aanbevelingen
In het FSRTE02 ontwerp is weinig aandacht besteed aan de banden, hier zou uitgereider naar gekeken moetn worden. Ook zal er een keuze gemaakt moeten worden voor een specifike veerdemper zodat het ontwerp voor de suspensionbox definitief gemaakt kan worden.

Voor het FSRTE03 ontwerp moet er goed gekeken worden naar de manier waarop het Unigraphics model wordt opgebouwd. Er moet een zogenaamde "bottom up" assembly gemaakt worden die helemaal parametrisch opgebouwd is.

Het Aprilia SXV 5.5 blok is een alternatief voor de Suzuki. Het blok vraagt wel om een compleet andere auto. Carbon kan hierbij wellicht interressant zijn.

English summary

Background
The Formula Student competition is a competition in which university teams from all over the world compete. In the 2004 event the Formula Student Racing Team Eindhoven (FSRTE) competed with a design in class 3 and in 2005 the FSRTE competed with an unfinished car in class 2. This year's aim is to compete in the 2006 event in class 1.
In this class, a single seated race car has to be built. The maximum cylinder capacity is 600cc and an intake restrictor is obligated, reducing the maximum engine power to 65kW.

Objective
The objective is to design and build a car, manage and market it and finally to compete with the car in the race. Therefore, the teams have to assume that a manufacturing firm has engaged them to produce a prototype car for evaluation. In the future the firm is planning to produce 1000 cars each year for the nonprofessional weekend autocross racer. Therefore the car has to be produced at a cost below €21.000. On the other hand the car should have a very high performance in terms of acceleration, braking and handling qualities. The challenge is to design a prototype car that best meets these objectives.

General aim
The aim for this project is to make a design for the FSRTE02 chassis and suspension, considering the desired car handling and the regulations determined by the Formula Student organization. Furthermore all parts have to be assembled onto the chassis using Unigraphics.

Conclusions
The chassis shape is based on the earlier designed FSRTE01 but optimized on torsion stiffness. The suspension properties are set for optimum road holding.
The chassis consists out of two nearly symmetrical halfs made out of watercutted ALUCORE honeycomb sandwich panels. Thin plate part layouts are lasercutted to obtain high precision. The front and rear roll hoops are placed around the chassis and mounted from the inside. The dashboard is a sandwich structure with a polyurethane core. The steering system transmission is countersunk into the dashboard. The suspension mounting points are designed for make-ability. A Suzuki 600 cc motorcycle engine is used to drive the rear wheels using a chain. The suspension system is equipped with two monoshocks. Front and rear roll stiffness is added using helical springs. A motorcycle steering damper is used for roll damping. All is mounted into two suspension boxes front and rear.

Recommendations
In FSRTE02 design little attention is paid to the tires.
Furthermore work has to be done on the suspension boxes; they can be finalized when a specific monoshock is chosen. Considering the FSRTE03 design, attention has to be paid to the way the Unigraphics assembly is set up. So called "bottom up" assembly should be applied and the Unigraphics assembly should be completely parametric. The Aprilia SXV 5.5 engine has to be looked at seriously as alternative for the Suzuki engine. This engine demands a completely different design, a laminated carbon structure can be examined.

Preface

In september 2003 six enthusiastic students with a passion for wheels raised the Formula Student Racing Team Eindhoven or FSRTE. They were determined to join the Formula Student competition in the U.K., a racing competition among universities from all over the world. In november 2003, the FSRTE found Wouter Berkhout willing to be the head designer of the FSRTE01. The FSRTE was planning to compete in the design class of the 2004 event. In December 2003 I performed an internal traineeship for the FSRTE on the final drive for the FSRTE01. At that time I got enthusiastic for designing a race car. In july 2004, I visited the Formula Student event together with seven other students and my coach Nick Rosielle. The Technische Universiteit Eindhoven obviously had to compete with a built car. Half a year later in february 2005 I was asked to do the chassis and suspension design for the FSRTE02, several weeks later I started graduating.
In my point of view it had to be a continuation of the work of Wouter Berkhout.
The FSRTE02 chassis and suspension design had to be feasible, makeable and completely finished. Meanwhile the FSRTE01 was being built to compete in the 2005 event. This is when problems occurred, detailing was under estimated and little attention was paid to accuracy. This enhanced my effort to generate a fully detailed chassis and suspension design including building instructions. In september 2005, the FSRTE started with a new committee. Many students joined the team to help to realize the FSRTE02.
I enjoyed inspiring them to think of new ideas and helping them to design the parts.
It took me quite some effort to finish my graduation. I wanted a perfect final assembly so not a single part would interfere. While the chassis was being built I had to write my report but I also wanted to see if everything went right on the building site.

During the project Nick Rosielle has been my coach as head of the Constructions and Mechanisms group. His knowledge and common sense have been very useful for me. Therefore I want to thank him. Every week, the students of the constructions and mechanism group have been helpful and inspiring to me, so I would like to thank all of them. Furthermore I would like to thank Ton Serné, Igo Besselink and Antoine Schmeitz for their help on suspension geometry and tires.
And of course I would like to thank the FSRTE committees of 2005 and 2006 and the FSRTE team members for the pleasant corporation.

List of figures

List of tables

1 Introduction

1.1 Project backround

The Formula SAE competition is a competition in which university teams from all over the world compete. The main aims are to teach students to raise a team which is able to design and build a car, manage and market it and finally to compete with the car in the race.
Six different Formula SAE competitions are held in 2006:

1. Formula SAE held in Michigan, USA and organized by SAE
2. Formula SAE West held in California, USA and organized by SAE
3. Formula SAE Australasia held in Australia and organized by SAE Australasia
4. Formula SAE Brasil held in Brasil and organized by SAE Brasil
5. Formula SAE Italy held in Italy and organized by ATA
6. Formula Student held in the United Kingdom and organized by IMechE

All competitions use equal rules and have open registration policies accepting registrations by student teams representing universities in any country.

The Formula Student competition started in 1998 as demonstration event in which two U.S. cars and two U.K. cars competed.
Formula Student has three classes, The Formula Student Racing Team Eindhoven (FSRTE) started competing in the Formula Student competition in 2004, in class 3, which means only a design was presented and judged.
For 2005 the FSRTE competed with an unfinished car (designed in 2004), in class 2.
The aim for the 2006 event is to compete with a finished and fully tested car in class 1.

The main conclusion of the 2005 "unfinished car" experience was that a fully detailed design was needed in time. Therefore the aspects of planning and managing were reconsidered.

1.2 Objective

The teaching aspect of the competition can be seen in its objective. The objective stated by the organization is quoted below:
"For the purpose of this competition, the students are to assume that a manufacturing firm has engaged them to produce a prototype car for evaluation as a production item. The intended sales market is the nonprofessional weekend autocross racer. Therefore, the car must have very high performance in terms of its acceleration, braking, and handling qualities. The car must be low in cost, easy to maintain, and reliable. In addition, the car's marketability is enhanced by other factors such as aesthetics, comfort and use of common parts. The manufacturing firm is planning to produce four (4) cars per day for a limited production run and the prototype vehicle should actually cost below $25,000. The

challenge to the design team is to design and fabricate a prototype car that best meets these goals and intents. Each design will be compared and judged with other competing designs to determine the best overall car."

1.2.1 Project aim

The aim for this project is to make a design for the formula student **chassis and suspension 2006**, considering the desired car handling and the regulations determined the formula student organization. Furthermore the complete car's assembly will be made to ensure that all part will fit.

1.2.2 Project approach

In 2004 Wouter Berkhout designed the first formula student car on the Technische Universiteit Eindhoven. This car was built partly in 2005 and was then called the "FSRTE01", therefore the design of Wouter Berkhout will henceforth be referred to as the "FSRTE01". This design is studied intensively; also the recommendations were taken into account. Some effort has been put into an alternative and completely new chassis design. But a completely detailed and performable design was preferred and therefore the FSRTE01 chassis design has been used as a base for the FSRTE02 design.
First the general properties are determined for the FSRTE02 car, the car dimension and the tires determine the design forces. Then the chassis properties are determined. The chassis type choice is made by comparing a plate structure with a tubular spaceframe structure. A suitable and machineable material is chosen. The chassis shape is determined using FEM analysis to compare on stiffness. The FEM analysis is also used to check the chassis strength. Then the suspension properties are determined in chapter 4.
Chapter 5 describes the complete chassis design step by step using Unigraphics figures. The suspension design is treated in chapter 6. First the suspension properties are translated to a suspension lay-out in Unigraphics. Then several suspension system concepts are shown. The best concept is worked out and its assemblage is shown step by step. Finally the complete FSRTE02 assembly in Unigraphics is shown and the chassis construction process till thus far is described and illustrated using photographs.
This report will be finalized with conclusions and recommendations.

2 General FSRTE02 properties

In this chapter the general properties of the FSRTE02 are discussed.
First the engine is chosen and the matching car mass is determined. Then the car's dimensions are explained. The tires are chosen and shortly discussed.
Finally the design forces are calculated for different handling situations.

2.1 Engine

The engine is the heaviest part of the car. The maximum permitted cylinder capacity is 600cc, furthermore the engine must have an air intake restrictor of 19 mm.
The resulting engine power and mass play an important role in the overall car design. To be able to make an approximation of the total car mass two completely different competitors have been examined;

Figure 2.1: The DUT04 from Delft Uiversity of technology

The first car is an extremely light car, the DUT04 from Delft University of technology. Delft made a very small chassis with very small wheels (10 inch) almost like a go-kart. Its total mass is only 125 kg and a Yamaha WR 450F engine of 32kg (oil included) is used. The Yamaha has approximately 30 kW with an air intake restrictor.

Figure 2.2: The UT03 from the University of Toronto

The second car is the Formula student 2005 event winner, the UT03 from the University of Toronto. This car has a total mass of 213 kg and uses a Honda CBR-600 engine of 55 kg (oil included). This engine has about 60 kW with an air intake restrictor.
The UT03 is chosen to represent the lightest cars using a 600 cc, four cylinder engine.

The DUT04 has about **0.24 kW/kg**, while the the UT03 has **0.28 kW/kg**.
Therefore the UT03 will be faster on a straight track, but the DUT04 has the advantage
that it will be faster in tight and fast cornering due to its low mass. Each team has its own
view onto this subject.

But both cars do have in common their "car mass : engine mass" ratio of **3.9**.
So when saving mass on the engine one is also able to save mass on the rest of the car.

The FSRTE02 design depends on the engine choice, therefore two different engines are
considered, the aprilla SVX5.5 engine and the Suzuki GSX-R600.

2.1.1 The aprilia SXV5.5 engine

The aprilia SXV5.5 engine is an off-road motorcycle engine which is also used for
supermoto. The engine and its stock specifications are shown in figure 2.3.

Cycle	Four stroke
Cylinder line-up	2 cyl, 77º V-twin
Cylinder capacity	550 cm^3
Transmission	5-speed sequential
Starter	Electric
Carburetion	Injection
Cooling	Liquid
Valve actuation	Single overhead cam, 4 valves/cyl
Max. power	53 kW @ 11.500 rpm
Max. torque	Unknown
Bore x stroke	80 x 55 mm
Engine weight	31 kg (oil included)
Power: weight	1.71 kW/kg

Figure 2.3: The aprilia SXV5.5 engine and its specifications

This engine has very high power to weight ratio and would therefore be very suitable
for the formula student racing car. The expected power with an intake restrictor is 41 kW.

Using the SXV5.5 engine it should be possible to design a car of approximately 125 kg
using the "car mass : engine mass" ratio of 3.9. The power to weight ratio will then
become **0.33 kW/kg**.

2.1.2 The Suzuki GSX-R600 engine

This engine is used on the Suzuki GSX-R600 motorcycle which is a sports motorcycle. It is the most powerful 600 cc sports bike engine. The engine and its stock specifications are depicted in figure 2.4.

Cycle	Four stroke
Cylinder line-up	4 cyl, inline
Cylinder capacity	600 cm^3
Transmission	6-speed sequential
Starter	Electric
Carburetion	Injection
Cooling	Liquid
Valve actuation	DOHC
Max. power	88.3 kW @ 13000 rpm
Max. torque	69.6 Nm @ 10800 rpm
Bore x stroke	67 x 42.5 mm
Engine weight	55 kg (oil included)
Power:weight	1.61 kW/kg

Figure 2.4: The Suzuki GSX-R600 engine and its specifications

This engine is expected to have a maximum power of 65 kW with an air intake restrictor. The aim is to design 215 kg car using the "car mass : engine mass" ratio of 3.9. The power to weight ratio will then become **0.30 kW/kg**.

The main advantage is that the FSRTE already has two of these engines. Therefore this engine will be used in the FSRTE02.

2.2 Car dimensions

The formula student competition has two racing days, on the first day, three events take place; the acceleration test, the autocross and the skidpad test.
The first test is a straight run over 100 meter.
For the autocross event a tight sprint track must be completed in the quickest possible time. The maneuverability and handling qualities of the car are tested in this event.

The skidpad test is a very narrow track marked by cones, this test is designed to measure the cornering ability of the cars around a 15 meter diameter circle on a flat surface.
The average G-force can be calculated from the time it takes to complete the circle.
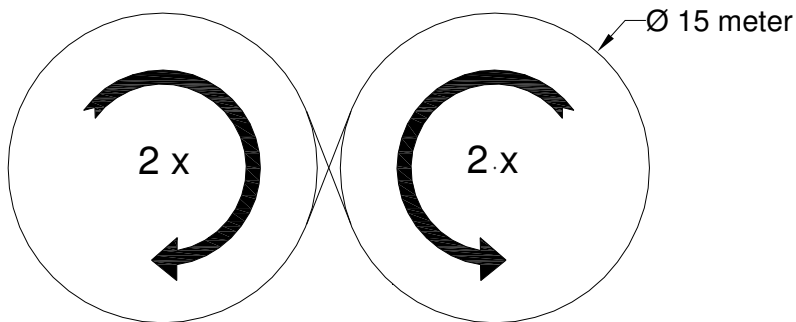
Figure 2.5: Skidpad track

The second racing day the endurance & fuel economy event takes place. This test is driven on a go-kart track, with a lot of tight corners. Some corners are even made narrower by cones. The average speed during this test is about 40 km/h, and top speed lies below 100 km/h.

Figure 2.6: Endurance and fuel economy event

Earlier research done by Wouter Berkhout on the final results of 2003, proved that a short wheelbase is very important for the endurance and autocross. A minimum wheelbase of 1525 mm is required by the rules; the FSRTE02 will get a wheelbase of **1550 mm** to stay on the safe side. The front and rear track are important in the slalom parts. Cars having a smaller rear track than the front track have scored best in 2003.
Therefore the FSTRE02 will front track of **1250 mm** and a rear track of **1200 mm**.

2.3 Tires

Tires play a very big role in the car's handling. All the forces act on four small contact patches on the tires. To be able to use the tire information a tire model is needed.
There are different suitable tires for the FSRTE02. Avon provides a lot of tire testing data, furthermore Avon tires were used on the FSRTE01 (which did not drive) so they are available. Therefore the Avon 3 ply pro-series tires will be used on the FSRTE02 and the corresponding data will be analyzed in this paragraph. The front tire size will be 7.0/20.0-13 and the rear tire size will be 8.2/22.0-13, this is based on the front to rear mass distribution ratio of 46/54 determined in appendix A.

2.3.1 Slip angle

When cornering the tires will make a slip angle to generate central tire forces.
Figure 2.7. shows a top view of the racecar during steady state cornering. Forces F_1-F_4 represent the four central tire forces. Angles α_1- α_4 are the corresponding slip angles. The central tire force is the tire force component pointing at the actual turning point C_1. Force F_5 represents the centrifugal force acting on the center of gravity CG. So when driving the described path at constant speed there will be force equilibrium with forces F_1-F_5 pointing at/from point C_1. When speed is increased C_2 will become the actual turning point, centrifugal force increases, slip angles and therefore central tire forces increase, and a new equilibrium arises.
When speed is zero, point C_0 will be the actual turning point, slip angles are zero, there are no central tire forces and no centrifugal force.
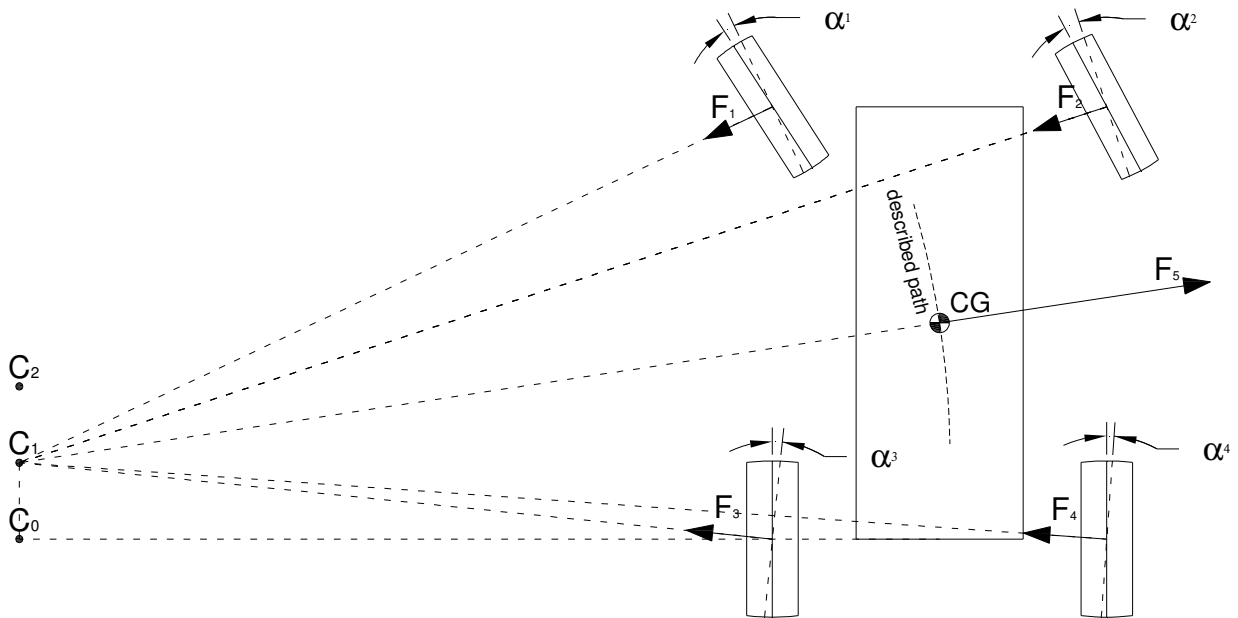
Figure 2.7: Force equilibrium during steady state cornering

In tire tests not the *tire central force* is measured but the *tire lateral force* is measured. The characteristics for the Avon 7.0/20.0-13 3 ply pro-series front tire are depicted in figure 2.8. The test is done at a camber angle of 2° and a tire pressure of 20 psi, measuring slip angles from -7° to 7° with different tire normal forces.
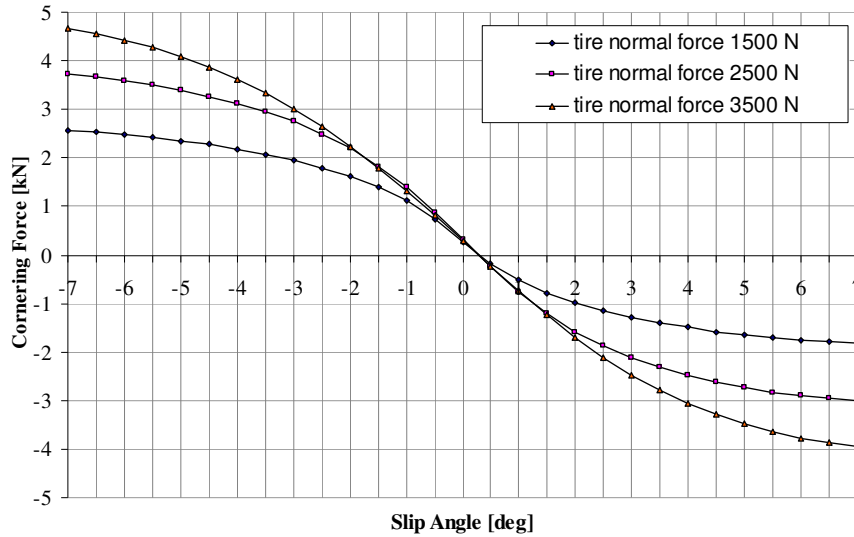
Figure 2.8: Avon 7.0/20.0-13 3 ply pro-series, cornering force against slip angle

To explain the difference between tire central force and tire lateral force a zoomed in picture of one tire is shown in figure 2.9. The tire lateral force is always perpendicular to the tire, while the tire central force is always pointing to the actual turning point of the car. The tire lateral force is resolved into tire central and *tire drag force*.
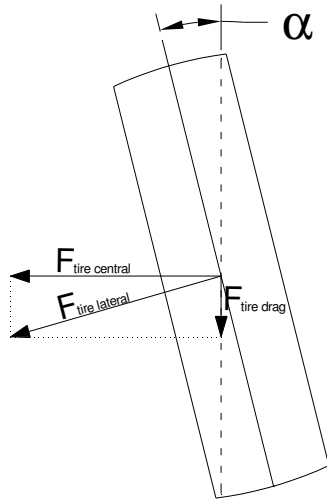
Figure 2.9: Forces acting on one tire

The drag force is a disadvantage; especially for a formula student car this will cost engine power. The equations for the $F_{tire\ central}$ and the $F_{tire\ drag}$ are:

$$F_{tire-central} = \cos(\alpha) \cdot F_{tire-lateral} \qquad \text{(equation 2.1)}$$

$$F_{tire-drag} = \sin(\alpha) \cdot F_{tire-lateral} \qquad \text{(equation 2.2)}$$

So the drag force needs to be as low as possible. On the other hand a large tire central force is needed. This can be achieved by a large $F_{tire\ lateral}$ at a low slip angle α. The $F_{tire\ lateral}$ is dependent on α as depicted in figure 2.10, the higher the initial slope the higher the $F_{tire\ lateral}$ at a low slip angle.

This is also known as a high *cornering stiffness C_α*.
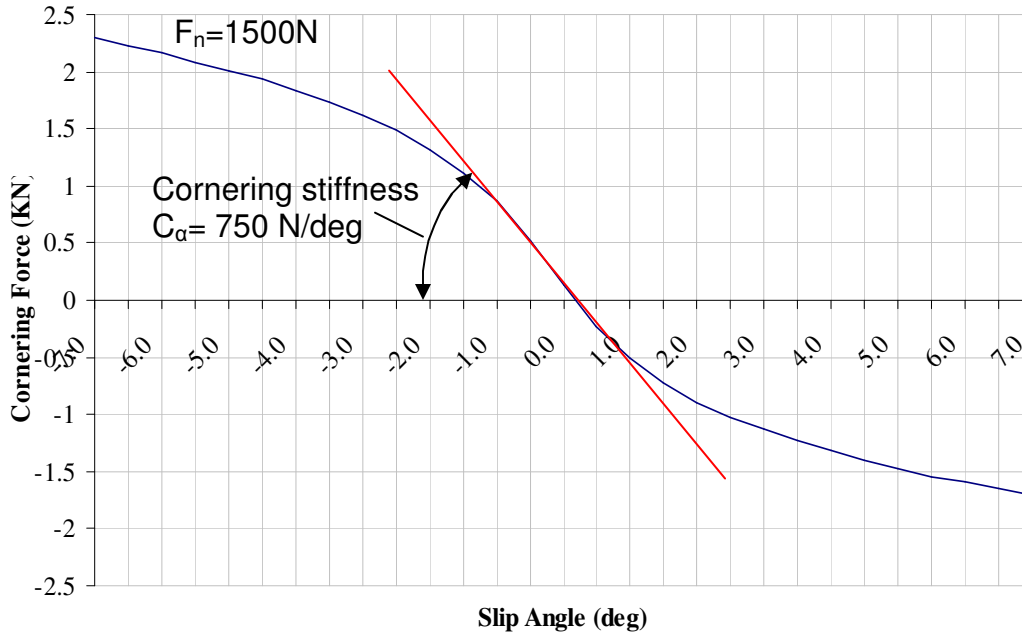
Figure 2.10: Avon 7.0/20.0-13 3 ply pro-series, cornering stiffness at F_n is 1500 N

The cornering stiffness is dependent on the normal force F_n, the higher the normal force, the higher the cornering stiffness. Therefore the *cornering stiffness coefficient C_s* is introduced which is the cornering stiffness C_α divided by the normal force F_n, stated below in equation 2.3. C_s is a non-dimensional constant tire parameter.

$$C_s = \frac{C_a}{F_n}$$

(equation 2.3)

In case of the Avon 7.0/20.0-13 3 ply pro-series front tire the C_α *is 750 N/deg* at a normal fore F_n of 1500 N. This means the front tire cornering stiffness coefficient **C_s=0.5 /deg.** This is good value for racing tires as it helps to keep the tire drag forces low. Furthermore a high cornering stiffness coefficient has a positive effect on road-holding, higher stiffness means a higher natural frequency, so a slalom can be done faster.

2.3.2 Friction model

The standard friction model is stated in equation 2.4.

$$F = \mu \cdot F_n \qquad\qquad\text{(equation 2.4)}$$

This friction model can also used for simple tire modeling. The more normal force F_n in the contact patch the more force between the tire and the ground plane (road surface) can be transmitted. The friction coefficient μ provides a boundary for the tire performance.

A very often used method is the friction ellipse, this ellipse shows the friction coefficient μ of the tire in both directions. Figure 2.11 shows the tire and its two main friction directions.
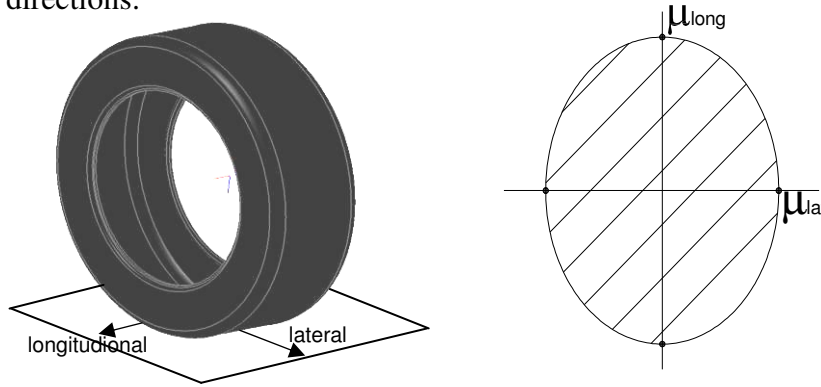
Figure 2.11: Tire on surface with lateral and longitudinal μ

The friction ellipse shows the μ distribution, with μ_{long} and μ_{lat} the friction coefficients in longitudinal and lateral direction. The $\mu_{long}/\mu_{lat}=1$ for this kind of racing tires, this means the friction ellipse is actually a friction circle. This produces realistic values for acceleration and cornering performances in paragraph 2.4.

Another important tire characteristic is that the friction coefficient decreases as normal force increases. This is a linear relation. This relation is extracted from the data in figure 2.8 by calculating the friction coefficients, for different normal forces (1500 N, 2500N, and 3500 N) using equation 2.4. This is done at a slip angle of 7°, larger slip angles are not interesting because of rapidly increasing drag forces (equation 2.2). The result is plotted in figure 2.12

$$\mu_{long}= \mu_{lat} = 1.74 - 1.28e\text{-}4*F_{N\text{-}f}$$
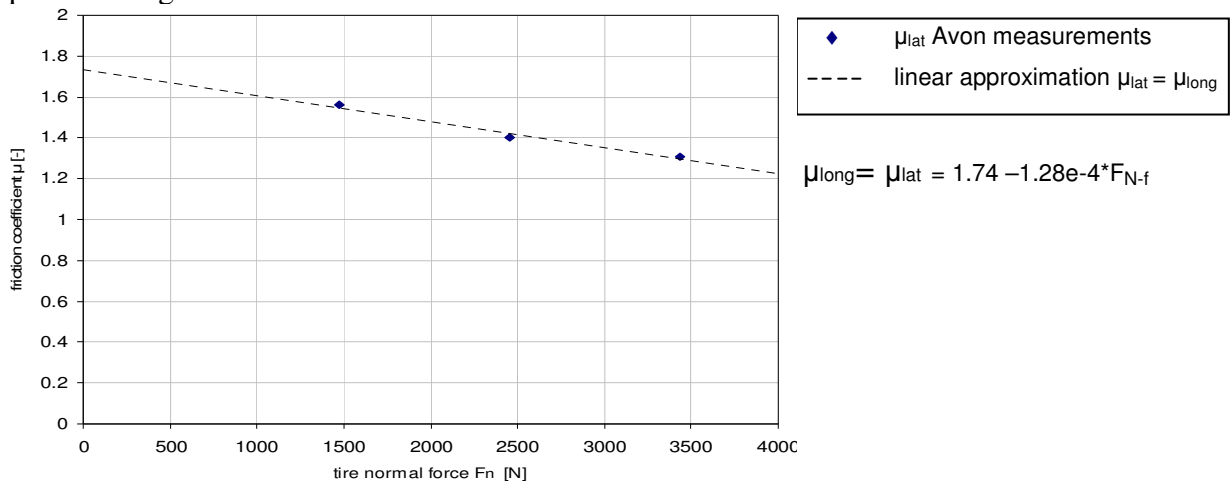
Figure 2.12: μ_{lat} and μ_{long} at a slip angle of 7° for the front tire on dry road

The corresponding linear relation for the front tire on a dry road is shown in equation 2.5.

$$\mu_{long} = \mu_{lat} = 1.74 - 1.28 \cdot 10^{-4} \cdot F_{n-f}$$ (equation 2.5)

Furthermore, functions are made for the tires on a wet surface using the assumption that the μ on a wet surface is 0.5 times the μ on a dry surface. Appendix B shows all the graphs and the corresponding linear relations for the front and rear tires.
The results will be used later on, to calculate the design forces.

2.4 Design forces

In Formula one monocoque design, forces are calculated looking at different handling situations. An example of this can be seen in figure 2.13.
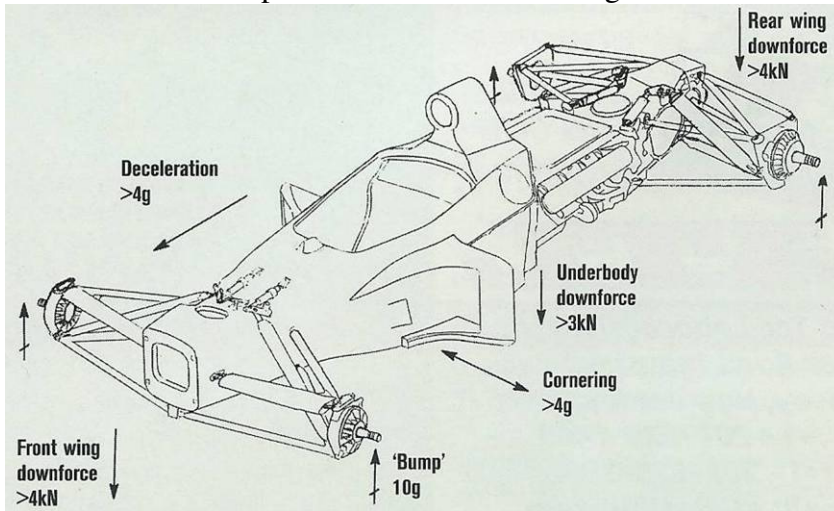
Figure 2.13: Forces acting on a formula one car taken (copied from "racecar engineering" nov 2003)

In case of the FSRTE02 aerodynamic forces are not taken into account. So the forces that do act, are braking and accelerating forces, cornering forces and bump forces.

In case of acceleration or braking longitudinal load transfer takes place. When cornering lateral load transfer takes place. Bump forces occur when a bump is taken. In the following paragraph the corresponding forces will be calculated.

2.4.1 Bump forces

Formula one bump force can be up to 10 G which means the load on every wheel can become 10 times the static load on that wheel.
For the FSRTE02 bump forces are assumed to be 2 G or smaller. The main reason is that the FSRTE02 has no large aerodynamic forces. Furthermore speeds are much lower on the go-kart circuit, so bumps are taken slower. Table 2.1 hows the maximum bump force values per wheel.

	Front wheel	Rear wheel
Bump force [N]	1330	1560

Table 2.1: Bump Forces

2.4.2 Braking and accelerating forces

The car mass will be 215 kg, together with the driver mass of 80 kg this results in a total mass of 295 kg. Without load transfer, 46% of this mass will be on the front wheels and 54% will be on the rear wheels, this is calculated in appendix A.
During braking or accelerating the front/rear load distribution will change.
While braking, load is transferred to the front axle and when accelerating load is transferred to the rear axle. In competition one should always brake and accelerate as fast as possible. This is limited by the tire longitudinal friction coefficient μ_{long}.
When braking, all tires are producing friction forces; this gives a force-equilibrium which is depicted in figure 2.14.

With:
$\quad$ **F_g** $\quad$ **gravity force**
$\quad$ **F_{cg}** $\quad$ **inertia force**
$\quad$ **$F_{N\text{-}f,r}$** $\quad$ **normal force front and rear wheels**
$\quad$ **$F_{B\text{-}f,r}$** $\quad$ **brake force, front and rear tires**
$\quad$ **a, b** $\quad$ **distances rear/front axle to center of gravity**
$\quad$ **h_{cg}** $\quad$ **height center of gravity**
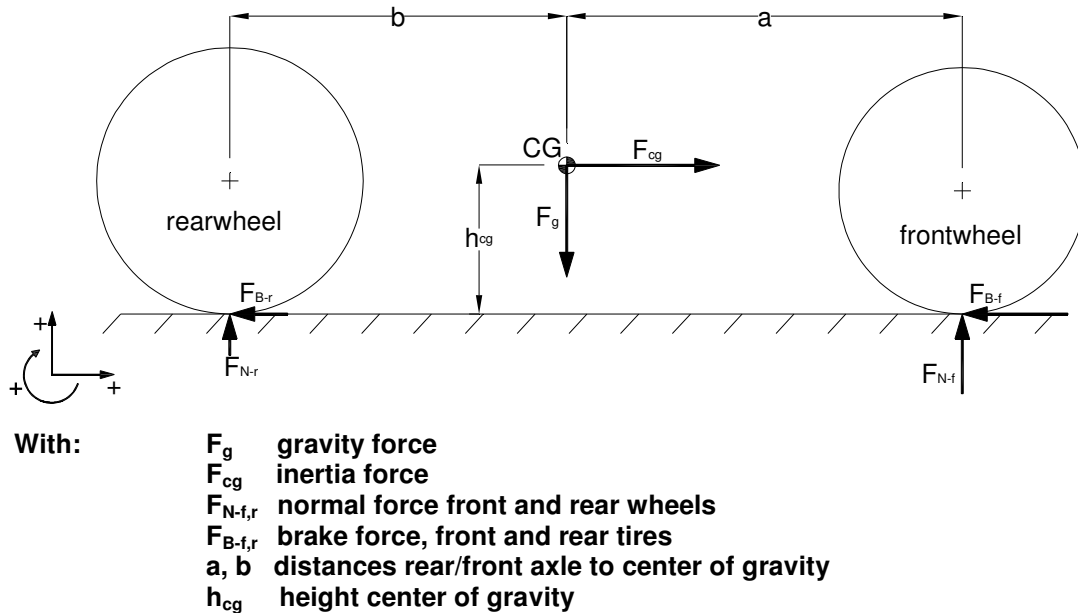
Figure 2.14: Force equilibrium during maximum braking

To find the brake distribution during maximum braking four equations must be solved; the equilibrium of moments around *CG*:

$$\sum M_{cg} = 0 \qquad \text{(equation 2.6)}$$
$$b \cdot F_{N\text{-}r} + h_{cg} \cdot (F_{B\text{-}f} + F_{B\text{-}r}) - a \cdot F_{N\text{-}f} = 0$$

And the force the equilibrium in vertical direction:

$$\sum F_y = 0 \qquad \text{(equation 2.7)}$$
$$F_{N\text{-}f} + F_{N\text{-}r} - F_g = 0$$

$F_{B,f}$ and $F_{B,r}$ can be written as functions of $F_{N,f}$ and $F_{N,r}$ using equation 2.4.

$$F_{B\text{-}f} = \mu_{long-f} \cdot F_{N\text{-}f} \qquad \text{(equation 2.8)}$$
$$F_{B\text{-}r} = \mu_{long-r} \cdot F_{N\text{-}r} \qquad \text{(equation 2.9)}$$

In paragraph 2.3.2 and appendix B, functions were derived for μ_{long-f} and μ_{long-r} on dry and wet road, these functions are substituted into equations 2.8 and 2.9.

Table 2.2 shows the results of solving the system of equations for dry and wet road.

	Dry road braking forces [N]	Wet road braking forces [N]
F_{N-f}	2230	1800
F_{N-r}	660	1090
$F_{LT-brake}$	900	470
F_{B-f}	3240	1360
F_{B-r}	1250	990
F_{cg}	4490	2350

Table 2.2: Braking forces

The braking load transfer force $F_{LT-brake}$ is the normal force change on the front and rear
wheels compared to the static situation, it will be used to calculate pitch angles.
By dividing the inertia force F_{cg} through the gravity force F_g the braking G's can be
calculated. On dry road the FSRTE02 brakes with 1.55 G and on a wet road the
deceleration is 0.81 G.

A similar calculation can be made for maximum acceleration. The main difference is that
the acceleration force is only applied on the rear wheels.
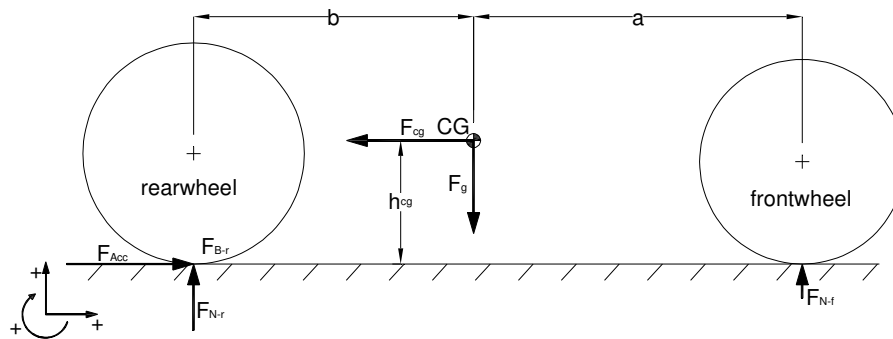
Figure 2.15: Force equilibrium during maximum acceleration

	Dry road acceleration forces [N]	Wet road acceleration forces [N]
F_{N-f}	610	1020
F_{N-r}	2280	1870
F_{LT-acc}	720	310
F_{acc}	3600	1550
F_{cg}	3600	1550

Table 2.3: Acceleration forces

The acceleration on a wet and a dry road are respectively 1.24 G and 0.54 G.

2.4.3 Cornering forces

Lateral load transfer takes place when cornering. The force equilibrium on the rear of the car during cornering at constant speed is depicted below in figure 2.16.
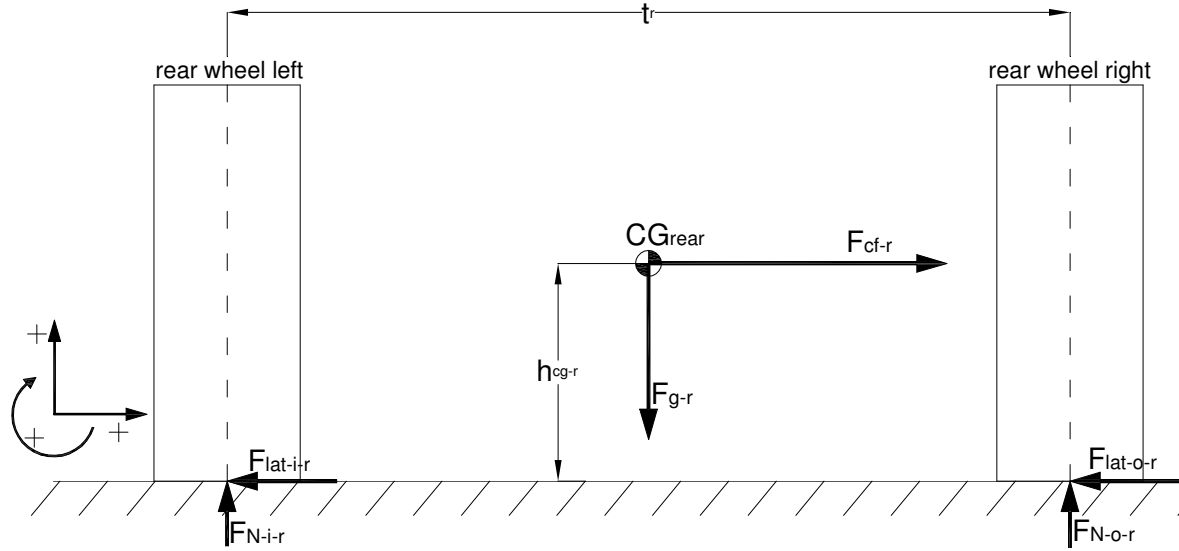
With:

	$F_{g\text{-}r}$	gravity force rear (54 % of total gravity force)
	$F_{cf\text{-}r}$	centrifugal force rear (54 % of total centrifugal force)
	$F_{N\text{-}i,o\text{-}r}$	normal force inner and outer rear wheels
	$F_{lat\text{-}i,o\text{-}r}$	lateral force inner and outer rear wheels
	t_r	track width rear
	$h_{cg\text{-}r}$	height center of gravity rear (calculated in appendix A)

Figure 2.16: Force equilibrium during maximum cornering

The equilibrium of moments around *CG*:

$$\sum M_{cg\text{-}r} = 0$$

$$\tfrac{1}{2} \cdot t_r \cdot F_{N\text{-}i\text{-}r} + h_{cg-r} \cdot (F_{lat\text{-}i\text{-}r} + F_{lat\text{-}o\text{-}r}) - \tfrac{1}{2} \cdot t_r \cdot F_{N\text{-}o\text{-}r} = 0$$

The equilibrium in vertical direction:

$$\sum F_y = 0$$

$$F_{N\text{-}i\text{-}r} + F_{N\text{-}o\text{-}r} - F_{g\text{-}r} = 0$$

$F_{lat\text{-}i\text{-}r}$ and $F_{lat\text{-}o\text{-}r}$ can be written as functions of $F_{N\text{-}i\text{-}r}$ and $F_{N\text{-}o\text{-}r}$ using equation 2.4.

$$F_{lat\text{-}i\text{-}r} = \mu_{lat-r} \cdot F_{N\text{-}i\text{-}r}$$

$$F_{lat\text{-}o\text{-}r} = \mu_{lat-r} \cdot F_{N\text{-}o\text{-}r}$$

μ_{lat} is a function of the tire normal force and is calculated in paragraph 2.3.2 and appendix B for both wet and dry road. A similar force equilibrium can be made for the front wheels. The lateral force equilibrium results, for both rear and front wheels, are stated in table 2.4.

	Dry road cornering forces [N]	Wet road cornering forces [N]
F_{N-i-r}	20	380
F_{N-o-r}	1540	1180
$F_{lat-i-r}$	40	370
$F_{lat-o-r}$	2640	1050
F_{cg-r}	2680	1420
F_{N-i-f}	130	390
F_{N-o-f}	1200	1170
$F_{lat-i-f}$	220	330
$F_{lat-o-f}$	1910	760
F_{cg-f}	2130	1090

Table 2.4: Cornering forces

The maximum lateral acceleration is 1.69 G

A low center of gravity is preferred, the reason for that can be now explained.
In figure 2.17 a graph is made in which the F_{lat-r} is plotted as a function of F_{N-r}.
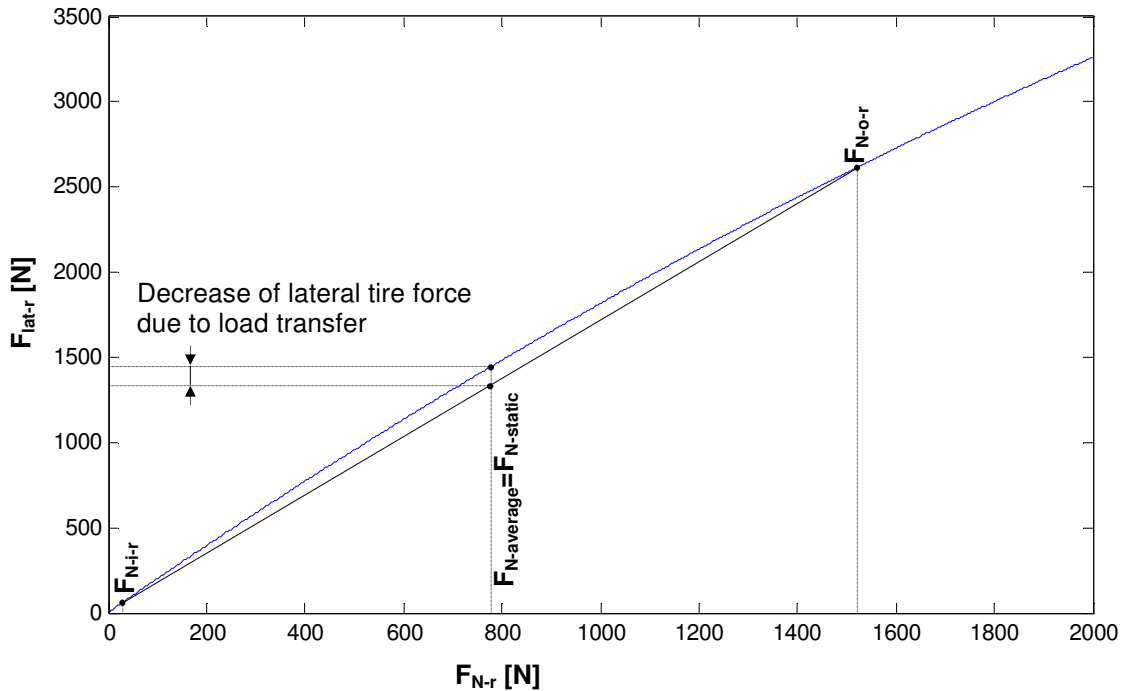
Figure 2.17: F_{lat-r} plotted as a function of F_{N-r}

Lines are drawn at the F_{N-o-r} and F_{N-i-r} values for maximum cornering.
The difference between F_{N-o-r} and F_{N-i-r} depends on center of gravity height h_{cg-r}, the higher h_{cg-r} the larger the difference. The $F_{N-static}$ represents driving straight, this is equal to the average of F_{N-o-r} and F_{N-i-r}, the $F_{N-average}$. But the corresponding maximum lateral forces differ. This indicated difference is the average decrease of lateral force of one tire. To get the total loss of two tires this value has to be doubled.
The conclusion is, the more load transfer the bigger the loss of lateral force.

3 Chassis properties

3.1 Chassis requirements

The chassis must be able to withstand the suspension forces. Therefore strong chassis points are needed there. The suspension will be adjustable; the most important parameter is the roll-stiffness. To be sure that the adjustment has the expected effect the chassis must have sufficient stiffness.
To quantify this requirement an aim is set. The aim is that the chassis deformation contributes less than 10% to the wheel travel displacement.
Therefore a torsion test is done with a FEM analysis in paragraph 3.4.1.

3.2 Chassis type

In the Formula Student competition two chassis types are used. The classic tubular space frames and the box structures (monocoque). To compare these two, they will be analyzed on specific stiffness.

A comparison is made between a square section plate construction and a frame of trusses (tubular space frame, figure 3.3) on specific stiffness. To make it a fair comparison both structures have to fit in the volume $w*w*l$ and have to have the same material volume (identical mass). Furthermore the square section plate construction has a constant wall thickness and the trusses in the frame have an equal and constant truss section area. Depicted in figure 3.1 are the limiting volume $w*w*l$ and the three loadcases, tension, bending (in two directions) and torsion, that will examined.
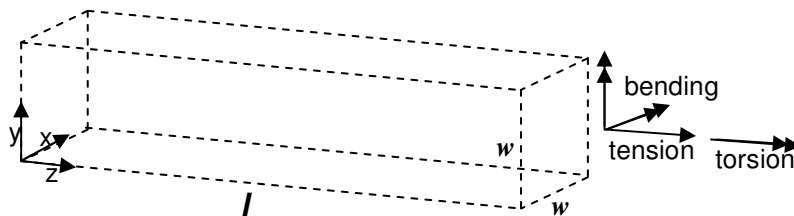
Figure 3.1: Limiting volume

First the most optimal geometry for both constructions within the volume is determined. Starting with the closed section tube, three possible configurations are drawn in figure 3.2.

Relative stiffness under:	tension	1	1	1
	bending	1	≈8	≈64
	torsion	1	≈8	≈64
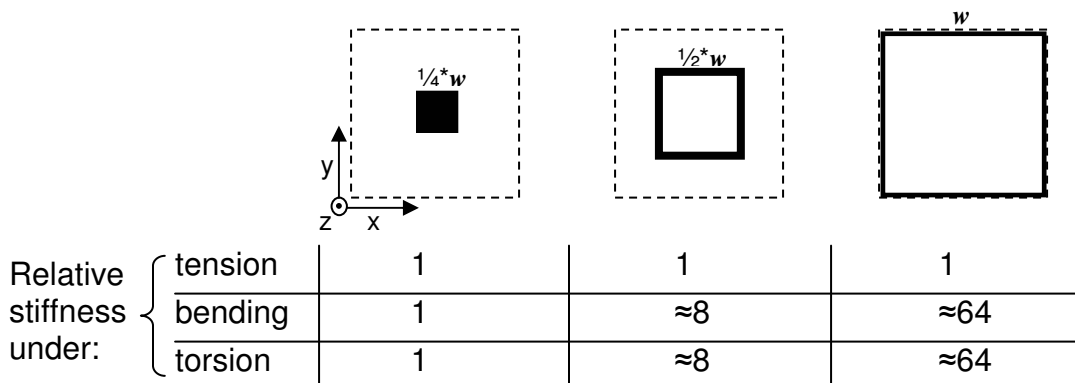
Figure 3.2: Three possible configurations for the closed section tube

The bending and torsion stiffness rises as the outside dimensions of the tube are chosen larger. So the best geometry in term of stiffness is to maximize the outside dimensions of the cross-section within the given area *w x w*.

The best geometry for a tubular space frame within the volume is a traditional framework depicted in figure 3.3. The angle α is 45º which is very close to the optimal angle for maximum torsion stiffness.
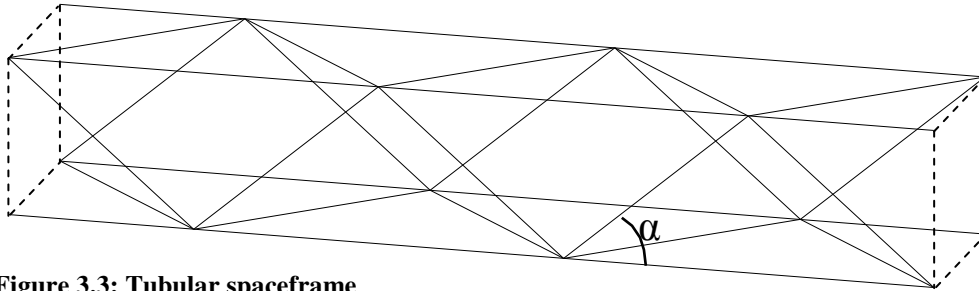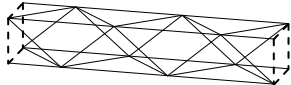
Figure 3.3: Tubular spaceframe

Now both constructions can be compared on specific stiffness having identical material volume i.e. identical mass. This is done in table 3.1, depicted below.

	tubular spaceframe	plate construction	ratio plate over tube
Stiffness in tension Comparing both axial loaded areas will do, in the tubular spaceframe the diagonal trusses stay unloaded.	$A_{load,t} = \dfrac{4 \cdot w \cdot t}{1 + \sqrt{2}}$	$A_{load,p} = 4 \cdot w \cdot t$	$\dfrac{A_{load,p}}{A_{load,t}} \approx 2.4$
Bending stiffness (4 point bending test) Bending stiffness is linear with the area moment of inertia I, so those are being compared.	$I_t = \dfrac{w^3 \cdot t}{(1 + \sqrt{2})}$	$I_p = \dfrac{2 \cdot w^3 \cdot t}{3}$	$\dfrac{I_p}{I_t} \approx 1.6$
Torsion stiffness *E* and *G* are material constants the multiplication factor of 2.6 is based on the assumption that υ=0.3	$k_t = \dfrac{w^3 \cdot t \cdot E}{2 \cdot l \cdot (2 + \sqrt{2})}$	$k_p = \dfrac{w^3 \cdot t \cdot G}{l}$	$\dfrac{k_p}{k_t} \approx 2.6$

This comparison is from TUE lecture note 4007 "design principles"

Table 3.1: Comparison tubular spaceframe and plate construction on specific stiffness

The plate construction has more stiffness in all loadcases, therefore the FSRTE02 will get a box structure chassis.

3.3 Chassis material

The box structure will be made from sandwich panels. These are lightweight, and have a high stiffness perpendicular to the panel. A simple sandwich panel consists out of three layers. The outer layers are thin aluminum sheets which are best for in-plane shear, pressure and tensile forces. The core material is a low density material glued between the outer sheets.

Different core materials can be used to produce the sandwich panel, appendix C gives an overview of core materials with densities around 60 kg/m^3, together with their main properties.

Most core types have their own specific application. The PU (polyurethane) is the most common foam type. The more expensive foam types like PVC-X (Polyvinylchloride-cross linked) and PVC-L (Polyvinylchloride-linear) foams have higher strength and stiffness. The most stiff and strong foam type is PMI (polymethacrylamide) with the brand name Rohacell and is used for helicopter blades due to its good heat properties. Furthermore two types of honeycomb structures are examined, aluminium honeycomb and Nomex paper honeycomb. Both structures have a much higher strength and stiffness than the foam-cores with the aluminium honeycomb having the highest stiffness.

The ALCAN factory produces sandwich panels called ALUCORE panels. These panels consist of a 9 mm aluminum honeycomb core and two 0.5 mm thick aluminum skins. These prefabricated aluminum honeycomb panels will be the building material for the FSRTE02 chassis thereby limiting the gluing work on the assembly.

3.3.1 ALUCORE honeycomb panel properties

The properties of the prefabricated honeycomb panels are important for FEM analysis of the chassis. The equivalent thickness is calculated in case of bending load, considering only the aluminium cover sheets . In figure 3.4 two plates are depicted, the left plate is the honeycomb panel and the right plate is a solid panel of 6.5 mm thickness. Both have an equal second moment of area while the honeycomb panel weighs 3.3 kg/m^2 and the solid plate weighs 17.6 kg/m^2.
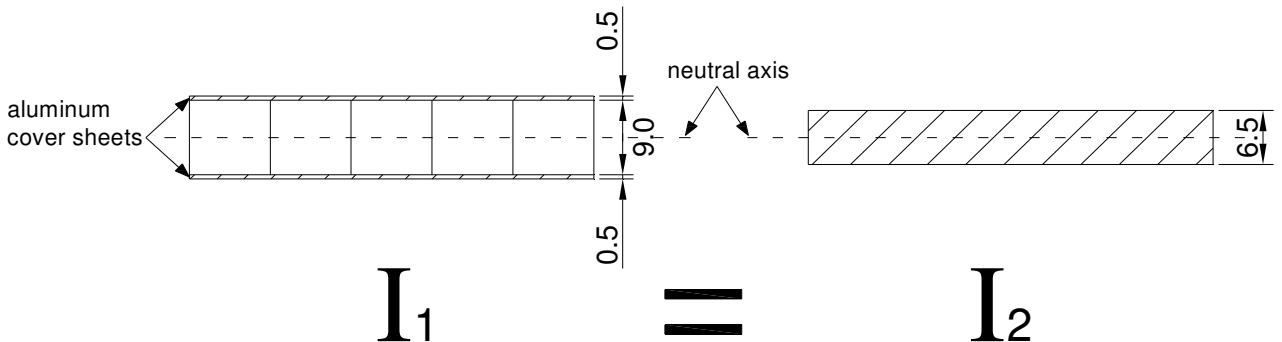
Figure 3.4: Honeycomb panel compared to a solid plate for out of plane bending load

3.3.2 ALUCORE honeycomb panel cutting

Due to the chassis layout the different honeycomb panels will get complex shapes. Using a laser- or water cutting machine complex shaped sheets can be produced accurately and fast.

Laser cutting is a faster technique but can not be used for cutting the ALUCORE honeycomb panels because of reflection of the laser beam. However laser cutting will be used to cut the solid plate layouts.

Water cutting offers a good alternative for cutting the ALUCORE. Figure 3.5 shows the water cutting machine and a test piece that has made.

Figure 3.5: Water cutting

3.3.3 ALUCORE honeycomb panel bending

According to the ALCAN company it should be possible to bend the panels on a press brake shown in figure 3.6.
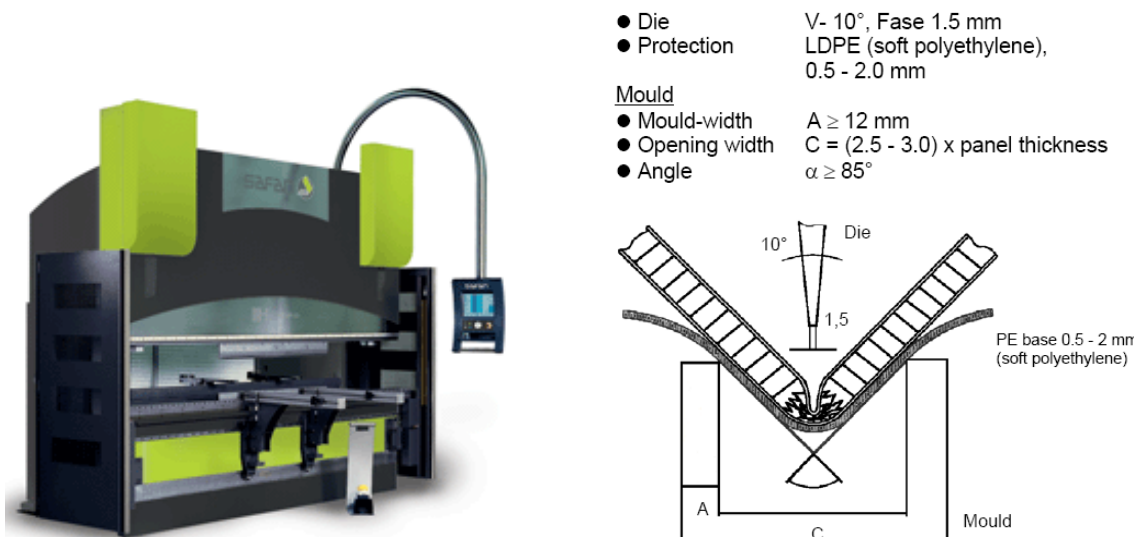
Figure 3.6: SAFAN hydraulic press brake with ALCAN bending instructions

Bending tests have been done with different moulds and protection sheets. Figure 3.7 shows the best press brake setup and its result.
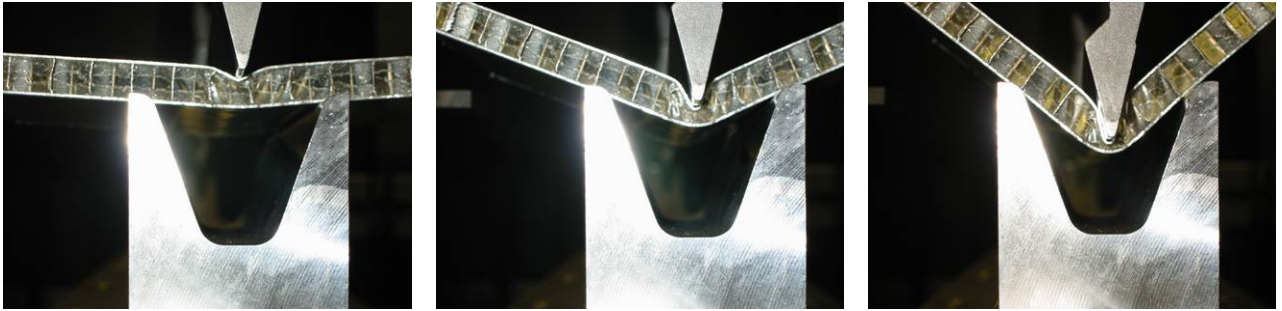
Figure 3.7: Bending on the SAFAN press brake and measuring the outer skin radius

The results of this test were satisfying, the outer skin radius corresponds perfect to the values given by ALCAN and the bend looks smooth from the outside. Having done these tests ensures the use of bending for the FSRTE02 chassis.

Three zones are distinguished in the bent corner, these are depicted in figure 3.8.
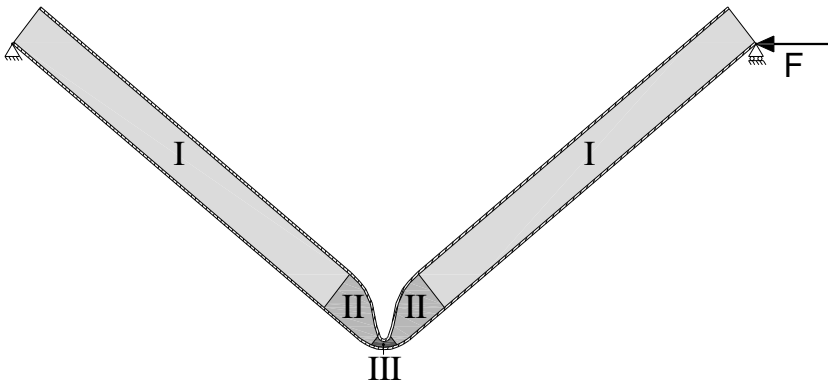
Figure 3.8: Bent corner with different deformation zones and the applied FEM loadcase

In zone I the honeycomb structure is undeformed. In zone II the honeycomb offers no strength and stiffness to the construction anymore, all honeycomb walls are buckled. Zone III has been deformed so extreme it adds strength and stiffness again. The bending stiffness is linear with the cubic height. The height of zone III is 20% of the original height. This means the bending stiffness of zone III is assumed to be approximately 1% of the zone I stiffness. Figure 3.8 shows the load case used for the FEM analysis.

Four different options for finishing the bent corner are compared on strength and stiffness using a FEM analysis. The strength is determined by looking at the maximum Von Mises stress. The stiffness is compared by looking at the displacement at the point where the force *F* is applied. All values are indexed to the values of option A in figure 3.9a.
Figure 3.9a shows the bent corner without any finish. In figure 3.9b the inner skin is brought back by gluing in a sharp edged corner profile. Figure 3.9c shows the same principle as 3.9b only the bend radius of the corner profile is enlarged.
The last option is shown in figure 3.9d, now the remaining gap is filled with glue.
To reduce weight micro balloons can be added to the glue.

Maximum Von Mises Stress: 142.3 Mpa
Stiffness bent corner: 30 Nm/rad

Maximum Von Mises Stress: 25.66 Mpa
Stiffness bent corner: 389 Nm/rad

Maximum Von Mises Stress: 10.28 Mpa
Stiffness bent corner: 1810 Nm/rad

Maximum Von Mises Stress: 11.26 Mpa
Stiffness bent corner: 740 Nm/rad
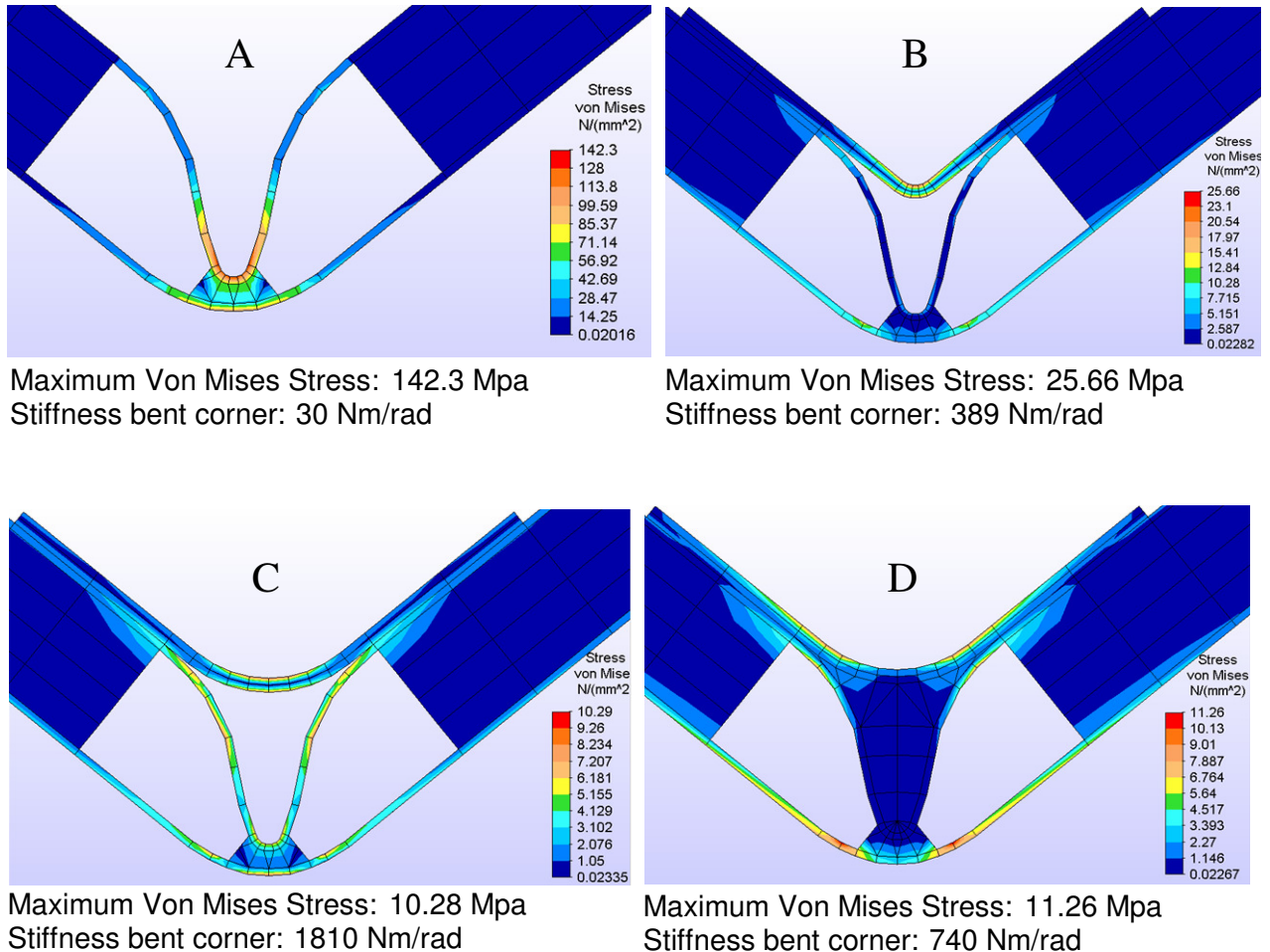
Figure 3.9 a, b, c, d : Four bend finish options and their FEM results

Option C shows the best results, it has the highest stiffness (60 x stiffness option A). Furthermore, option C has the highest strength due to the equal stress distribution.
If one compares option D with option C it turns out that filling the remaining gap with glue, only weakens the bent corner and adds more mass.

The bent corner finishing will be done by gluing in a corner profile with an inner radius of 8 mm.

3.3.4 ALUCORE honeycomb panel gluing

The honeycomb panels will be glued using Araldite 2015, a two component epoxy paste adhesive. The maximum shear strength is 16.5 N/mm^2 (tested by Viba) for aluminium–aluminium joints.
This test has been carried out by gluing two 25 mm strips together with an overlap of 12.5 mm creating a gluing spot of 25x12.5 mm

To convince the Formula Student jury of the strength of gluing, a special test can be done. Two 5052-aluminium tensile test strips are made. These strips are glued on two large aluminium blocks. This is depicted in figure 3.10.
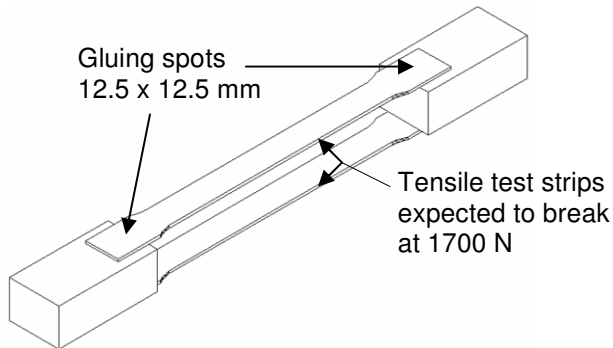
Figure 3.10: Gluing test to convince the jury

Using the a gluing spot of 12.5 x 12.5 = 156 mm^2 a tensile force of 156 x 16.5 ≈ 2500 N can be generated causing the aluminium tensile test strips to break (F=>1700).

3.4 Chassis shape

The most important aspects of the chassis shape are chassis stiffness and strength, ergonomics and crash safety, always carefully taking into account the mass.
The ergonomics determine the shape and the size of the driver compartment together with the side-impact which is set by the rules.
The front impact can be added later to the design.

A FEM analysis is done to examine stiffness and strength.

Three different chassis analyzed with FEM and compared on torsion stiffness.
- The FSRTE01 chassis designed by Wouter Berkhout.
- The second chassis is a low and wide edged chassis, and will therefore be called TUB chassis. This chassis could be suitable for the Aprilia engine (see paragraph 2.1.1)
- The FSRTE02 chassis, based on the FSRTE01 but optimized on stiffness

3.4.1 Chassis torsion stiffness

Torsion stiffness is the most important stiffness. If the chassis torsion stiffness and suspension stiffness would be of the same order, suspension stiffness would be less useful. Tuning of the suspension is then difficult and ineffective, one should not be guessing on adjustments. Therefore chassis torsion stiffness should be high compared to suspension stiffness.

The average axle force is approximately 1500 N. The torsion test is done by applying a moment of 1500*1.25= 1875 N on the chassis. The corresponding load case is depicted in figure 3.11. The rear tire road contact points are constrained in x, y and z direction and x and z direction respectively. On the front tire road contact point patches two forces of 1500 N each are applied in z and –z direction. This load case corresponds with a 2 G bump taken by a single front wheel so the resulting stresses are also representing a realistic bump situation.
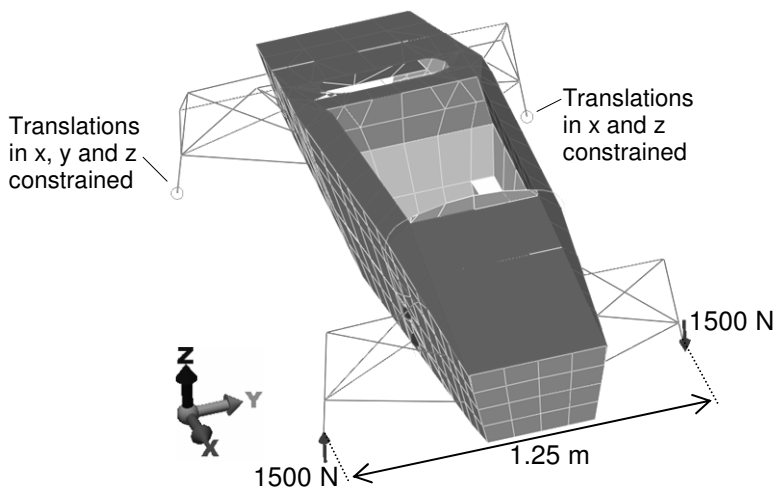
The FEM results are depicted in figure 3.12 a, b and c.
Figure 3.11: FEM torsion test loadcase

	FSRTE02		
Maximum Von Mises stress	16.4 N/mm²	40 %	
Torsion stiffness	575 kNm/rad	303 %	

	TUB		
Maximum Von Mises stress	25.6 N/mm²	62 %	
Torsion stiffness	260 kNm/rad	137 %	

	FSRTE01		
Maximum Von Mises stress	41.6 N/mm²	100 %	
Torsion stiffness	190 kNm/rad	100 %	

A — Stress von Mises N/(mm^2): 16.44, 14.81, 13.17, 11.54, 9.906, 8.273, 6.64, 5.006, 3.373, 1.74, 0.1066

B — Stress von Mises N/(mm^2): 25.64, 23.08, 20.52, 17.96, 15.4, 12.84, 10.28, 7.722, 5.162, 2.602, 0.04226

C — Stress von Mises N/(mm^2): 41.6, 37.46, 33.33, 29.19, 25.05, 20.91, 16.78, 12.64, 8.503, 4.365, 0.2281

Figure 3.12: Torsion stiffness of three different chassis

The FSRTE02 chassis has been optimized for torsion stiffness.

The main changes that have resulted in a 3 times higher torsion stiffness compared to the FSRTE01 chassis, are stated below.

- A rear cover around the engine has been added. It is expected to add about 1.5 kg of weight but it offers much more torsion stiffness.
- The FSRTE01 has torsion tubes to reduce the loss of stiffness due to the hole in which the driver is seated. The cross section of these torsion tubes is enlarged without limiting the driver's freedom of movement.
- Furthermore the torsion tubes where made longer, so the forces in the tubes are spread better into the rest of the car. Now they extend from the engine cylinder head, through the seat panel around the dashboard to the front suspension unit.

The aim is that the chassis deformation contributes less than 10% to the wheel travel displacement. Therefore the chassis torsion stiffness is compared to the suspension roll stiffness. It turns out that the roll stiffness is **3.8%** of the chassis torsion stiffness.

3.4.2 Chassis strength

The chassis strength has only been examined for the FSRTE02 chassis.

Therefore different loadcases have been applied, for maximum acceleration, maximum braking and maximum cornering situations using the forces calculated in paragraph 2.4. The graphical results are depicted in appendix D, the maximum occurring Von Mises stresses are stated in table 3.2.

Load case	Maximum occurring Von Mises stress
Maximum acceleration	3.5 N/mm^2
Maximum braking	9.3 N/mm^2
Maximum cornering	26.3 N/mm^2

Table 3.2: Maximum occurring Von Mises stress on different load cases

All stresses stay well below the yield stress of aluminium 3003 of 140 N/mm^2 so the FSRTE02 chassis has sufficient strength.

4 Suspension properties

All passenger cars are equipped with a suspension system to cope with bumps in the road. The larger the bumps the larger the wheel travel.

A go-kart does not have a suspension system but its chassis only consists of an almost flat tubular frame which can deform to keep all four wheels on the road surface.

The racetrack is partly a go-kart circuit and partly an airport runway, which means there are no large bumps to expect. Therefore a car without a suspension system might be an option; nevertheless the Formula Student rules require a fully operational suspension system. Spring and shock absorbers must be added front and rear with a usable wheel travel of 51 mm.

The FSRTE02 is constructed with a suspension system. Comfort is not an issue; the longest event takes 20 minutes. Bumps will be small so the minimum required wheel travel of 51 mm will be used. Furthermore the rules require the wheel travel to be divided into 25.4 mm jounce and 25.4 mm rebound with a ground clearance of 50 mm to prevent the car from hitting the ground. A double wishbone suspension system is to be used with pushrods to transmit the spring and shock absorber forces to the uprights.

A double wishbone system has the most adjustment possibilities and can be constructed with a low mass.

When cornering the lower triangle is always loaded more than the upper triangle.

The use of pushrods decreases the forces on the lower suspension triangle, therefore pushrods are preferred. Furthermore an adjustable anti-roll system is added to control the cars roll angle and to be able to set the under- and over steering properties.

4.1 Suspension stiffness and damping

Normal passenger cars have a natural bump frequency around 0.8-1.4 HZ, while racecars have frequencies up to 5-6 Hz. Such high stiffness is needed to have a stable ground clearance for the aerodynamics. The aerodynamic force pushing the car on the road can be considered as an increase of weight.

The main aim of the stiffness is to keep wheel normal force variations as small as possible to reach maximum tire grip.

The suspension stiffness of the FSRTE02 will have a natural frequency of 2.5 Hz. Equation 4.1 can be used to calculate the wheel rates front and rear.

$$\omega_{bump} = \sqrt{\frac{C_{wheel}}{m}}$$
(equation 4.1)

With C_{wheel} the suspension stiffness or wheel rate of a single wheel, m the mass resting on this wheel and ω_{wheel} the natural frequency in rad/sec.

The wheel rates front and rear are **16800 N/m** and **19600 N/m** respectively.

The wheel damping is determined by setting the non-dimension damping ratio ξ to 0.5 which is a commonly used value. To calculate the damping value equation 4.2 can be used.

$$d_{wheel} = 2 \cdot \xi \cdot \varpi_{bump} \cdot m$$
(equation 4.2)

The wheel damping for each front and rear wheel are **1070 Ns/m** and **1250 Ns/m**.

4.2 Lateral suspension properties

4.2.1 Roll center height

The most important parameter in the lateral suspension design is the roll center.
If lateral force is applied at the roll center the chassis will not roll.
The graphical determination of the roll center is shown in figure 4.1.
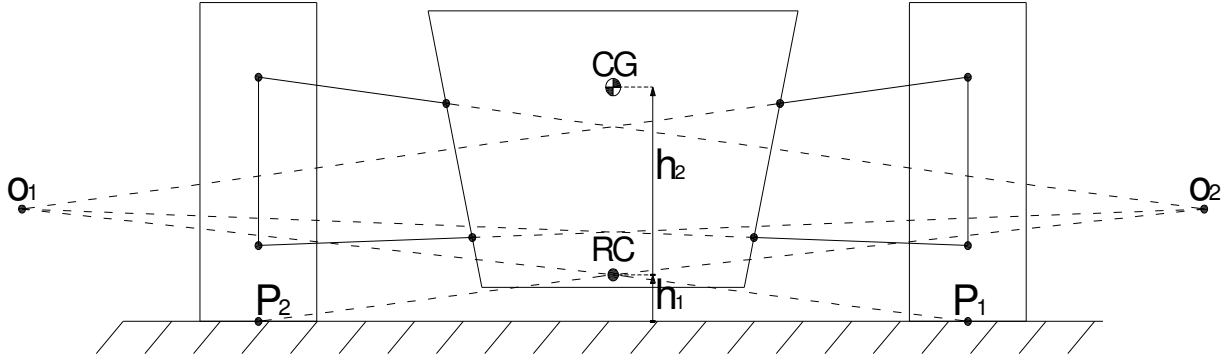
Figure 4.1: Graphical roll center determination

First the wishbone lines are extended creating intersection points O_1 and O_2. Then lines are drawn from these intersection points to the contact patch points P_1 and P_2. The intersection of these two lines represents the roll center. The roll center can drift during roll due to the movement of the wishbones. A roll moment can be formulated:

$$M_{roll} = h_2 \cdot F_{cg} \qquad \text{(equation 4.3)}$$

The roll moment in combination with the roll stiffness causes the chassis to roll.
Passenger car body roll is typically around 5° while race car chassis roll is 2° or less.
In Formula one body roll is minimized for aerodynamics. A large roll angle also affects camber angles. Some roll is needed however to get a natural cornering feeling.
Therefore the FSRTE02 chassis roll will be **2°**.

Constructing a roll center above the center of gravity *CG* will create a negative h_2 and a negative roll moment causing the chassis to roll into the curve like a motorcycle.

If the roll center is placed on the center of gravity *CG* the roll moment during cornering will be zero. And no roll stiffness has to be added to suppress the chassis roll.

Creating a roll center below the center of gravity *CG* will create a positive h_2 and a positive roll moment causing the chassis to roll out of the curve, which is a natural movement when driving the car. 2° Of chassis roll can be achieved using a small roll moment with little roll stiffness or using a large roll moment with a large roll stiffness. But what will happen when the roll center is placed below the road surface? Therefore two lateral force equilibriums for static curving are drawn in figure 4.2.a and 4.2.b. In the first situation the roll center lies above the road surface and in the second situation the roll center lies below the road surface which means h_1 is negative. The used forces are, the lateral tire forces F_{lat}, the tire normal forces F_N and the so called load transfer force F_{LT}.

Figure 4.2 a: Force equilibrium RC above road   **b: Force equilibrium RC below road**
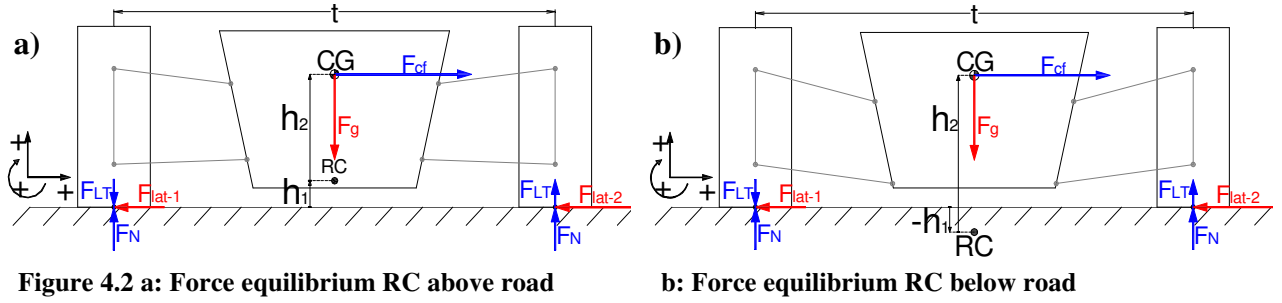
The equilibrium of moments around RC:

$$F_{LT} \cdot \tfrac{1}{2} \cdot t + F_{LT} \cdot \tfrac{1}{2} \cdot t + F_N \cdot \tfrac{1}{2} \cdot t - F_N \cdot \tfrac{1}{2} \cdot t - (F_{lat-1} + F_{lat-2}) \cdot h_1 - F_{cf} \cdot h_2 = 0$$

Substituting $F_{lat-1} + F_{lat-2}$ by F_{lat} result in equation 4.4:

$$F_{LT} = \frac{F_{lat} \cdot h_1}{t} + \frac{F_{cf} \cdot h_2}{t} \qquad\qquad \text{(equation 4.4)}$$

This function can be split in two parts, the so called geometric load transfer and the elastic load transfer

$$F_{LT-geo} = \frac{F_{lat} \cdot h_1}{t} \quad \text{and} \quad F_{LT-elastic} = \frac{F_{cf} \cdot h_2}{t}$$

If a fast steering input (step) is given on t_0 the front tires will make a drift angle and lateral tire forces F_{lat-1} and F_{lat-2} build up immediately.
Initially the car will not make a curve, but F_{lat-1} and F_{lat-2} will be led through the A-arms to the roll center where they act on the chassis. Due to the tire elasticity it takes till t_1 before the car will be driving the curve statically and the centrifugal force F_{cf} has reached its maximum. This can be seen in the force time graphs of figure 4.3.a and 4.3.b. These graphs also show the F_{LT-geo}, $F_{LT-elastic}$ and F_{LT} as a function of time. When the roll center lies below the road surface the load transfer will become negative first due to the F_{LT-geo} growing fast. This has a negative effect in fast steering situations like slaloming.

Figure 4.3 a: Time force graphs with RC above road   **b: Time force graphs with RC below road**
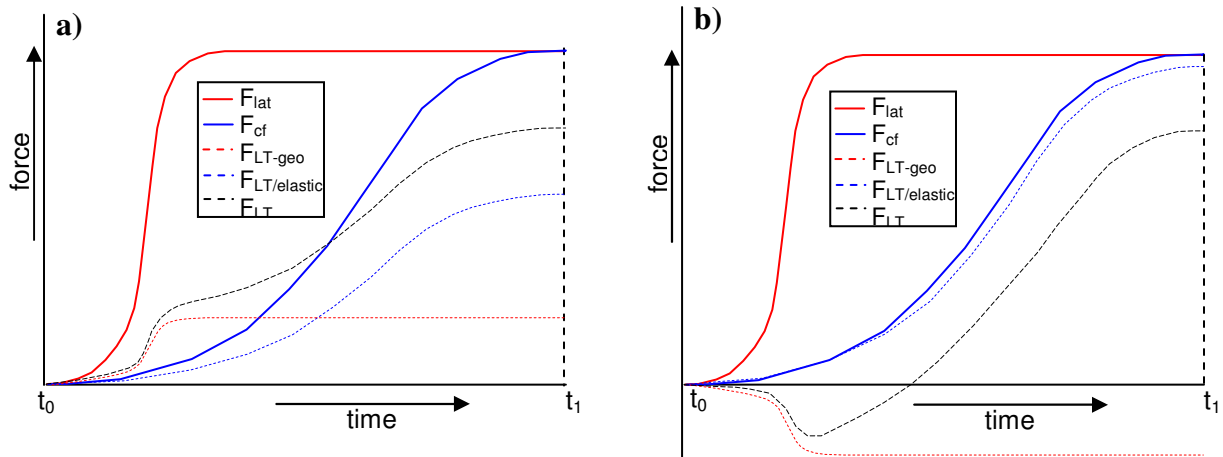
So the roll center has to be between the center of gravity and the road surface. Placing the roll center close to the road surface enlarges the roll moment and more roll stiffness is needed. Adding more roll stiffness will create a less independent suspension. An extreme situation occurs when roll stiffness is set to infinity. If one wheel is lifted then, the opposite wheel will travel the same distance too and unsprung mass is doubled.
So a high roll center is preferred to keep the suspension independent.

On the other hand there is the so called jacking effect. The jacking effect will cause the chassis center of gravity to rise in a corner. This is unwanted because the load transfer force F_{LT} will enlarge and the maximum F_{lat} will decrease.

The FSRTE02 suspension will have its roll center placed as low as possible, to prevent the jacking effect. Furthermore the roll moments rear and front will be chosen equal to minimize torque in the chassis.

The front roll center height is chosen h_{1-f} = **10 mm** above the road, h_{2-f} then becomes 316-10 = **306 mm**, using the front center of gravity height h_{cg-f} from appendix A. The front lateral centrifugal force during maximum cornering F_{cg-f}=2130 N (calculated in paragraph 2.4.3). The front roll moment is **650 Nm** during maximum lateral acceleration (calculated using equation 4.3)
Using $M_{roll-f}=M_{roll-r}$ the corresponding rear roll center height is determined; h_{1-r}=**97 mm**.

4.2.2 Roll stiffness and damping

The roll angle front and rear consists of two parts;

The first part is the roll angle due to the tire stiffness. In appendix E the radial tire stiffness front and rear are extracted from the Avon tire data at a tire pressure of 20 psi. The front and rear stiffness's are 200 N/mm and 210 N/mm respectively.
Combining this stiffness with the lateral load transfer force the tire compression can be calculated. This results in a chassis roll of **0.3°** front and **0.3°** rear due to radial tire compression.

The second part is caused by roll moment around the roll center. The maximum permitted chassis roll angle is 2°. So 2°-0.3°=**1.7°** of roll is permitted on roll stiffness front and rear.
With the $M_{roll-f}=M_{roll-r}$= 650 Nm the required roll stiffness front and rear becomes:

$$C_{roll,f,r} = \frac{650}{1.7^o \cdot (\pi/180)} = \textbf{22000 Nm/rad}$$

So the total roll stiffness becomes $C_{roll,f} + C_{roll,r} = C_{roll}$ = 44000 Nm/rad
The roll damping is determined by setting the non-dimension damping ratio ξ to 0.5. Unigraphics is used to calculate J_{roll}=9 kgm^2. Equation 4.4 is used to calculate the roll damping coefficient

$$d_{roll} = 2 \cdot \xi \cdot \sqrt{C_{roll}} \cdot \sqrt{J_{roll}} = 630 \text{ Nms/rad}$$

This is the roll damping for the whole car. The roll damping is delivered by two dampers one on the front and one on the rear. Therefore $d_{roll,f}= d_{roll,r}$= 630/2 = **315 Nms/rad.**

4.2.3 Camber

Camber is defined as the angle between the tire and the road in rear view.
Figure 4.4 shows three situations for the outer wheel; in the left situation the wheel is not cambered in other words the camber angle is zero. The middle situation shows a negative camber angle. The right wheel is cambered positive.
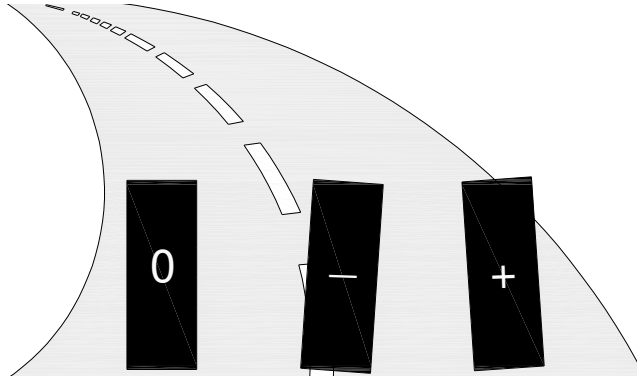
Figure 4.4: Three different outer wheel camber situations in a left corner

The last situation is preferred, a positive cambered wheel can generate a higher friction coefficient during cornering. Avon provides lateral tire force data for different camber angles. Table 4.1 shows the lateral front tire force at a slip angle of -7° at camber angles of 1°, 1.5^0 and 2°. It can be seen that the lateral front tire force rises as the camber angle rises.

Camber angle Avon 7.0/20.0-13 front tire	Lateral tire force [N] At a slip angle of -7°
1	4460
1.5	4490
2	4520

Table 4.1: Camber angle and lateral tire force

Large camber angles are not useful. Because the contact patch starts to become smaller. Avon tires were tested with camber angles of 1°, 1.5^0 and 2°, so that area is of interest. Therefore the camber angle in cornering for the FSRTE02 is set on 2°.

Figure 4.5 shows a suspension geometry with parallel A-arms. When cornering at maximum lateral acceleration resulting in 2° of body roll, the wheels will camber -2° too.
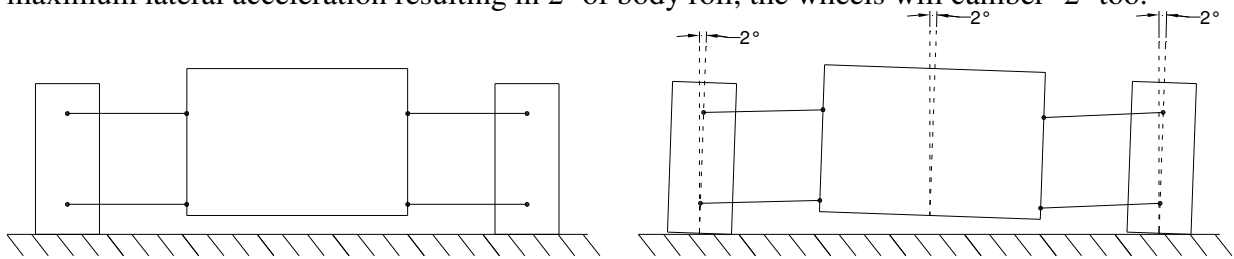
Figure 4.5: Parallel A-arm, body roll causes negative camber on both wheels

This is unwanted; it can partly be solved by using the wheel travel to create positive camber in cornering. Figure 4.6 shows such a geometry; the right wheel pivots about the imaginary pivoting point O_1 causing this wheel to camber positive in a left curve. The y-coordinate of point O_1 determines the camber change rate, the closer point O_1 lies to the right wheel the more camber change will take place when the wheel travels upwards. This is limited by line AB, placing point O_1 between this line and the right wheel will result in impracticable wishbone geometry.
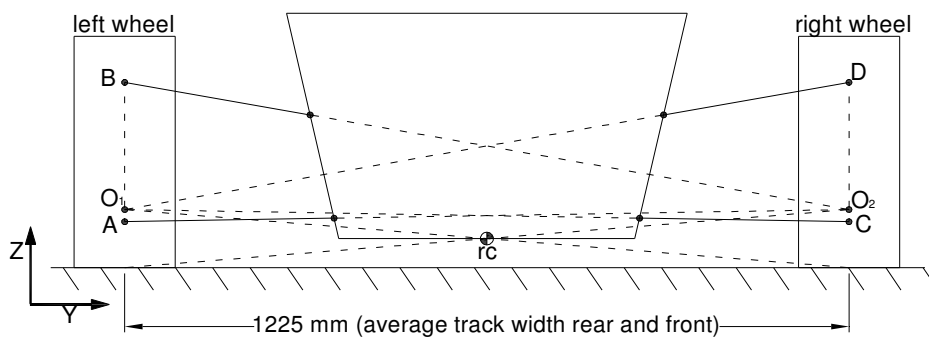
Figure 4.6: Suspension lay-out with camber change rate

The largest possible camber change rate is reached with points O_1 and O_2 on lines AB and CD. It will be arctan(1/1225)=**0.0468 deg/mm**

The suspension roll angle of 1.7^o causes a wheel travel of tan(1.7)*1225=**36 mm**. This means the inner wheel travels **in** 36/2=**18 mm** and the outer wheel travels **out** 36/2=**18mm**.
The positive camber change will be 18*0.0468=**0.85^o**
This means that the wheels will camber -2°+0.85^o= **-1.15**^{o} during maximum lateral acceleration.
By giving the wheel a **static camber** angle of **3.15**^{o} when driving straight, the camber angle during maximum cornering becomes 3.15-1.15=**2°**.

4.3 Longitudinal suspension design

The longitudinal suspension design affects the cars behavior during accelerating and braking. Pitch angles occur when accelerating or braking. In figure 4.7 the different causes of pitching are shown.
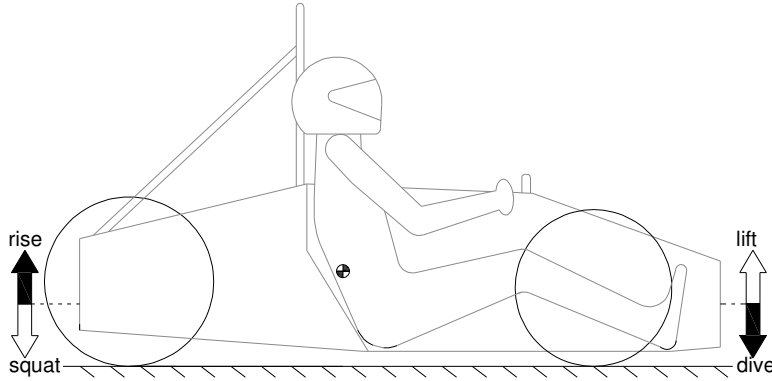
Figure 4.7: Pitching causes

The white arrows show the effects during acceleration; these are called lift and squat.
The black arrows indicate the effects of braking; these are called dive and rise.
These effects extend the time needed to reach a static accelerating or braking situation.
It takes longer to reach the equilibriums from figure 2.14 and 2.15.
Squat, dive and rise can be limited by applying anti-squat, anti- dive and anti-rise respectively on the suspension design.

4.3.1 Acceleration; squat effect

To compensate for the squatting effect the traction forces are used.
Figure 4.8 shows the double wishbone suspension in side view, the rear suspension has a pole *C* which can be considered as an imaginary pivoting point.
Figure 4.8 also shows the forces during accelerating.
The acceleration force is generated by the driveshaft torque. This means that acceleration force is effectively applied on the car at hub height. The F_{N-f} and F_{N-r} have been split up into the static part, $F_{N-f-stat}$ and $F_{N-r-stat}$, and the load transfer part F_{LT-acc}.
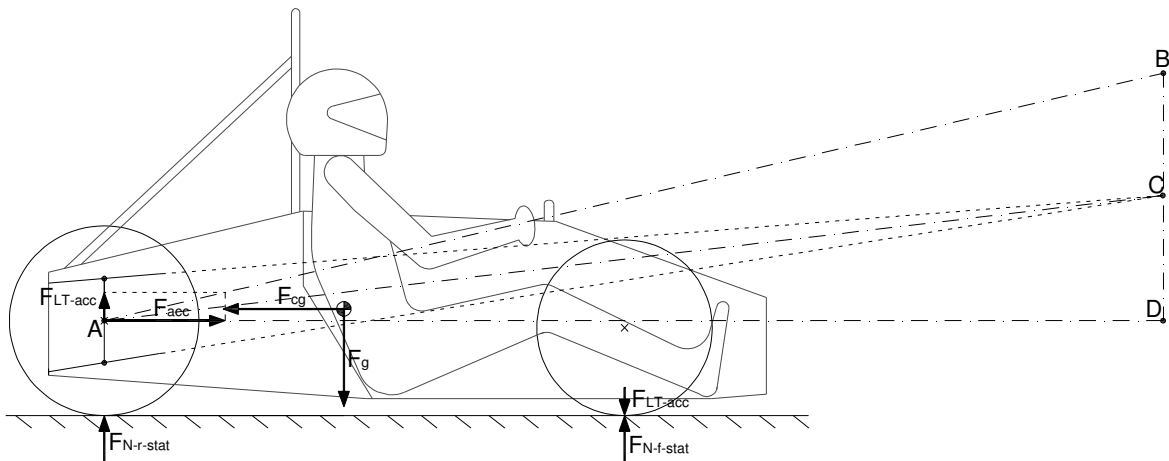
Figure 4.8: Anti-squat geometry

If the pole of the rear suspension is placed on line *A-B* in figure 4.8, the combined force of F_{acc} and $F_{LT\text{-}acc}$, points to point *B* which means no moment around *B* will be generated. In other words the car will not squat, this is called 100% anti-squat.
Practically only 50 % anti-squat is applied due to the chassis shape, which means half of the load transfer force F_{LT} is compensated and the other half still causes the rear spring to compress. This means distance *CD* is 50% of the distance *BD* as shown in figure 4.8.
Note: no anti-lift can be applied because there is no traction force on the front wheels to compensate for the decreased normal force $F_{N\text{-}f}$.
Finally the pitch effects can be calculated. In paragraph 2.4.2 $F_{LT\text{-}acc}$ for wet and dry roads are determined. Combining these forces with the suspension stiffness front and rear, the spring compression can be calculated. The results are in table 4.2

	Wheel travel front [mm]	Wheel travel rear [mm]	Pitch angle [deg]
Dry road	-21	+9	-1.1
Wet road	-9	+4	-0.5

Table 4.2: Wheel travel and pitch angle during maximum acceleration.

4.3.2 Braking; dive and rise effect

Both the diving and rising can be decreased by applying an anti-dive and anti-rise geometry. The force equilibrium during braking is drawn in figure 4.9

Figure 4.9: Anti-rise and ainti-dive geometry

Due to the use of inboard brakes on the rear of the car the rear braking force $F_{B\text{-}r}$ is effectively applied at hub height. The load transfer $F_{LT\text{-}brake}$ has been moved along its line of action to the rear hub center. Now line *AB* can be drawn, this is the so called 100% anti-rise line. If the pole of the rear suspension would be on this line the rear braking force exactly compensates rising of the car.

However the angles of the rear upper and lower A-arms in side view are already determined in paragraph 4.3.1 by setting an anti-squat percentage of 50 percent. This corresponds with line *AC* in figure 4.9 and 16% anti-rise. In other words the distance *DC* is 16% of the distance *DB*. And 84% of the load transfer force $F_{LT\text{-}brake}$ is led through the pushrod to the spring.

The front suspension side view is to be determined yet. The line *EF* shows the 100% anti-dive line. The anti-dive percentage will be set 50 %, when using higher anti-dive values, the front wheels tend to attack road irregularities. This means distance *HG* is 50% of distance *HF* and 50% of the load transfer force $F_{LT\text{-}brake}$ is led through the pushrod to the spring. Table 4.3 shows the wheel travel and pitch angle front and rear during maximum braking.

	Wheel travel front [mm]	Wheel travel rear [mm]	Pitch angle [deg]
Dry road	+13	-17	+1.1
Wet road	+7	-9	+0.6

Table 4.3: Wheel travel and pitch angle during maximum braking

4.4 Steering properties

Steering properties have large influence on the car's road holding. Different properties are considered: Ackermann, kingpin inclination, scrub radius, caster and bumpsteer.

4.4.1 Steering geometry

When using a "full Ackermann" steering geometry the steering arms are pointing inwards when using a rearward placed rack. When making a curve the front axles intersection point always lies on the rear axle. This intersection point corresponds with the actual turning point when speed is zero. In this way no tire scrub occurs because all tires are centered on the same point rolling on different radii. "Full Ackermann" is used on the traditional London taxi, and the "Lunar Rover" which drove on the moon.

When centrifugal forces increase slip angles are needed to build up the necessary lateral tire forces and the actual turning point moves forward. With "full Ackermann" steering the slip angle of the inner wheel will always be larger than the outer wheel slip angle. This is unwanted, the slip angles should be equal in case of zero load transfer to have the highest total lateral force. In reality load transfer will take place and the outer wheel normal force will be much higher than the inner wheel normal force causing a loss of friction coefficient.

To counterbalance for this loss the slip angle on the outer wheel has to be larger than the inner wheel slip angle. This can be reached by choosing a "negative Ackermann" steering geometry.

Often a "parallel" steering system is used which means that the steering angles left and right are always equal.

So at low speeds and sharp cornering an Ackermann geometry could be used to prevent tire scrub which causes tire wear and rolling resistance.

At higher speeds and fast cornering on the tire's performance limits, a "parallel" or "negative Ackermann" steering geometry is needed.

The exact geometry is not calculated, the upright will be constructed with adjustable linkage geometry. It can be adjusted from a "parallel" geometry with the steering arm pointing rearwards to a "full Ackermann" steering system.

4.4.2 Kingpin inclination and scrub radius

The kingpin is constructed by connecting the upper and lower upright pivoting points. Extending this line to the ground shows the scrub radius. The scrub radius causes steering moment when riding a bump. When the kingpin is leaning inward in the frontview this is called kingpin inclination or KPI. This can be used to change the scrub radius.

Figure 4.7 shows a schematic section of the front tire, the chosen rim has an offset of 21 mm from the rim midline, then the brake disk is placed with an inward offset of 9 mm. The clearance between the rim's inside and the brake disk is needed to mount the braking caliper. The lower pivoting point is placed as close as possible to the brake disk (38 mm from midline). If the upper pivoting point is placed straight above the lower pivoting point the scrub radius would be 38 mm. KPI angle also introduces undesirable camber changes. Some KPI is applied which has reduced the scrub radius to 24 mm.
The king pin inclination angle is arctan(23/240)=**5.5°**.
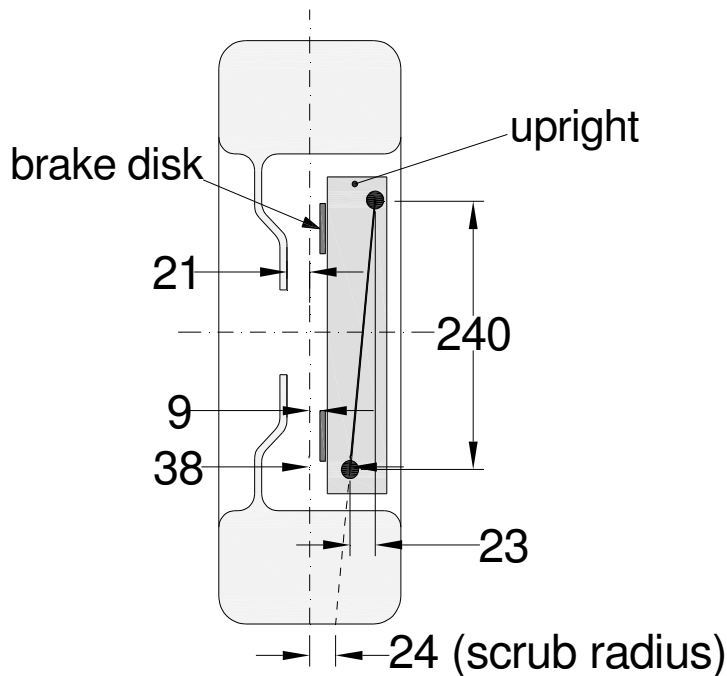
Figure 4.10: Front wheel in front view with king pin inclination and scrub radius

4.4.3 Caster and trail

Caster angle is defined as the angle of the king pin in side view. It influences mechanical trail. Mechanical trail is used to create steering stability (just like a shopping trolley wheel). Mechanical trail also causes steering moment. The tire lateral force is applied at the tire contact patch, the mechanical trail functions as an arm rotating about the king pin creating a moment on the king pin. This moment is felt by the driver through the steering system. Besides the mechanical trail there is pneumatic trail, this trail is caused by the tires. It reduces as the slip angle grows this is the feeling that one gets if the front tires start sliding. The pneumatic trail can even become negative. To make the steering system self centering, the mechanical trail has to be in the order of the pneumatic trail.

Furthermore caster can be used to counterbalance the camber changes due to the king pin inclination angle.

The FSRTE02 front wheel side view is depicted in figure 4.8. The pneumatic trail lies in the order of 35 mm, therefore the mechanical trail has been chosen **35 mm** too.
The king pin intersects the front wheel axis. The caster angle is arctan(32/240)=**7.6º**.
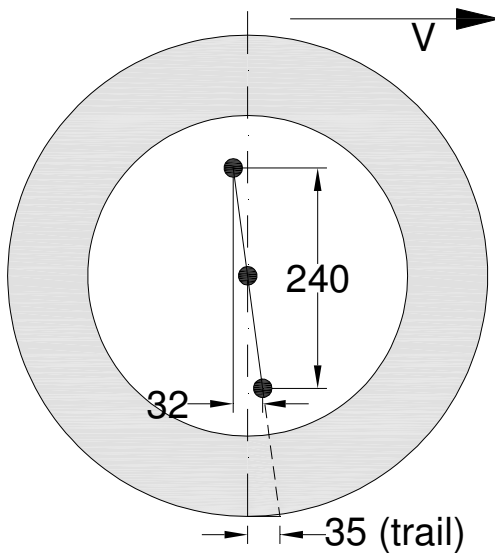
Figure 4.11: Front wheel in side view with caster angle and trail

4.4.4. Bump steer

Both the front and rear suspension have a tie rods which can be used to adjust toe in and out. The front tie rods a coupled via the steering rack which enables us to steer the front wheels. These tie rods can cause the wheels to make a steering angle when riding a bump. This is referred to as bump steer.

By choosing the correct coordinate for tie rod connection point bump steer can be prevented. This coordinate can be determined geometrically; this is done in figure 4.12.
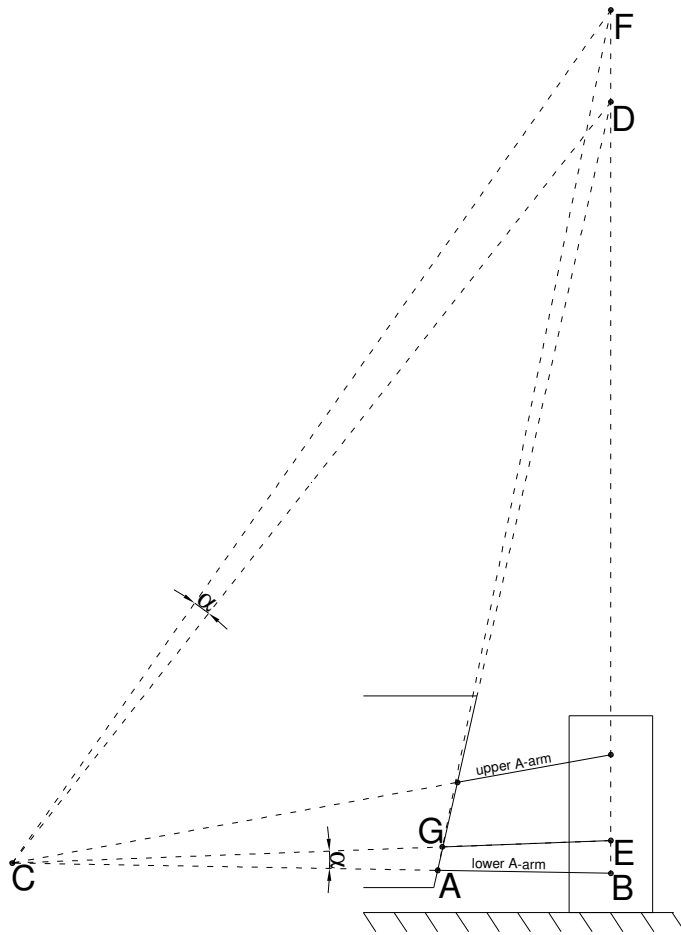
Figure 4.12: Graphical determination of anti-bump steer geometry

First points *A* and *B* are determined by extending the suspension lines. Then a line is drawn from the steering arm connection point *E* to point *C*. Now a line from point *B* through point *E* is drawn. The angle *α* in figure 4.12 between the lower A-arm and line *AC* is used to determine point *F*, by drawing line *CF*. Then line *AF* is drawn which intersects line *CE* in point *G*. If the steering rack-steering rod connection point is placed in point *G* no bump steer occurs.

This is verified by using Matlab Simmechanics, which simulates the 3D model. The result is plotted in figure 4.13.
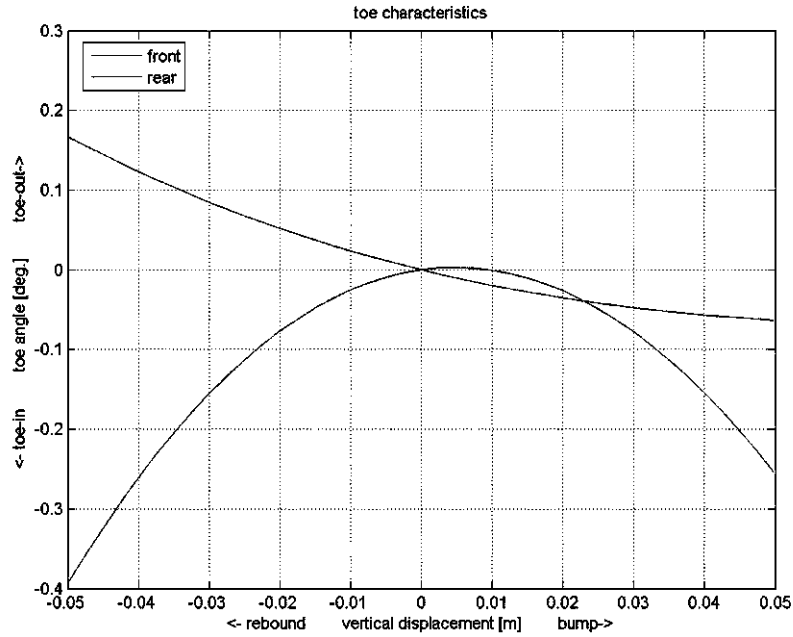
Figure 4.13: Toe characteristics of front and rear wheels

Although the anti bump steer geometry is applied some bump steer will still occur. This is because the imaginary pivoting points (*C, D* and *F*) do not stay constant over the wheel travel. But within this wheel travel of 51 mm in total, the toe in and out angles stay within an acceptable range.

5 Chassis design

5.1 Main structure

The FSRTE02 chassis shape is tested with a FEM analysis. In that stage the materials and the material thicknesses were already determined. Thereupon all the parts were designed in detail using Unigraphics. In this paragraph the parts are shown and explained step by step.

5.1.1 ALUCORE side panels

First the ALUCORE sidepanels were designed. The main thought has been to maximize bent edges length thereby minimizing the glued edges. Unfortunately it was not possible to fold the whole chassis from a single ALUCORE panel because the standard panel size was not large enough. Therefore two chassis halfs are designed. They are joint using two strips of aluminium to glue both (nearly) symmetrical parts together. Unigraphics sheet metal has been used to create the layout of the ALUCORE panels.
This is depicted in figure 5.1a, b and c.

glue
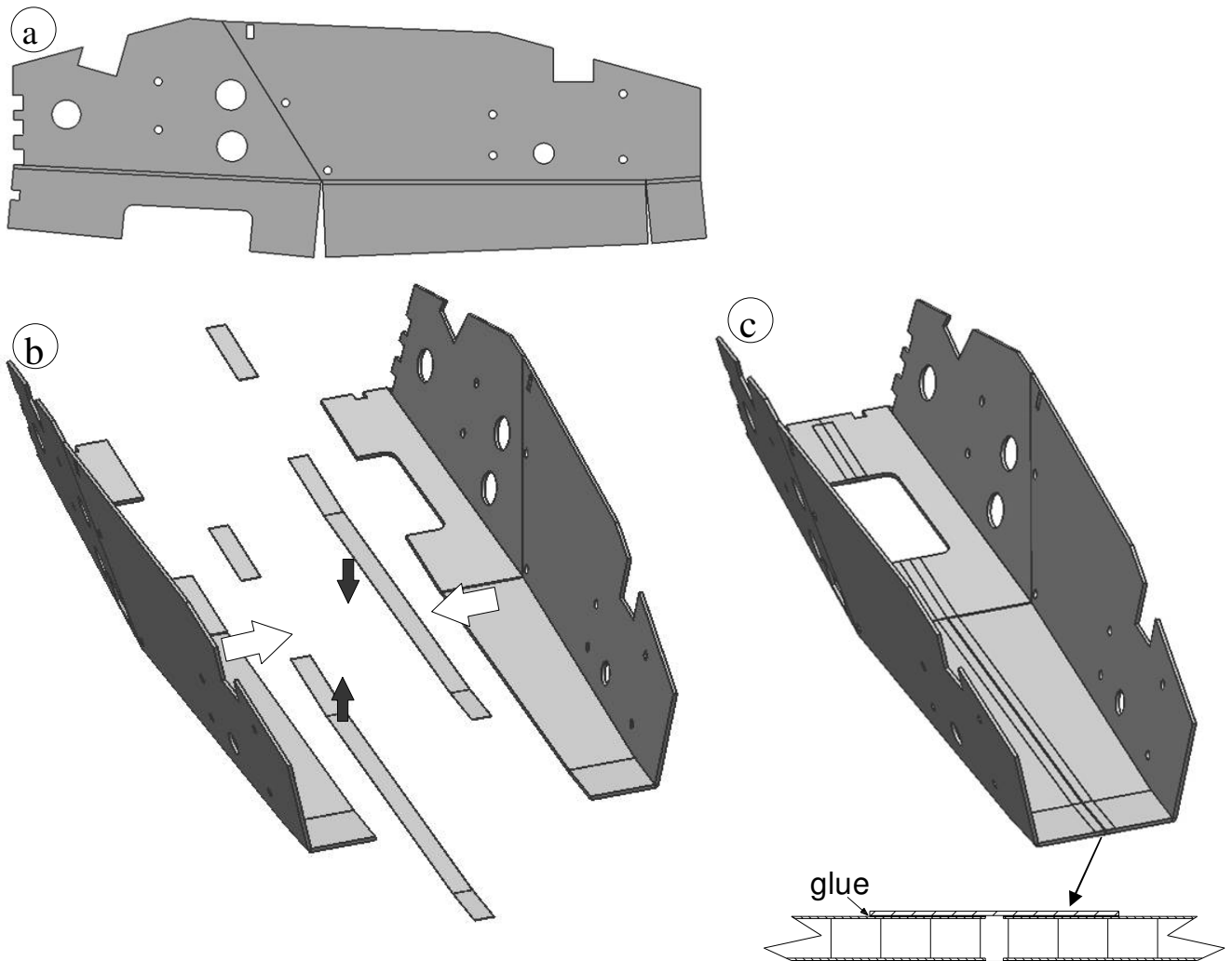
Figure 5.1 a: Layout ALUCORE panels   b: Joining both symmetrical half's   c: Gluing both half's

5.1.2 ALUCORE front and seat panel

The front and seat panel also ALUCORE panels. Figure 5.2a shows the placement of these panels. Figure 5.2b shows the detailed attachment cross sections in points 1, 2 and 3 from figure 5.2a.
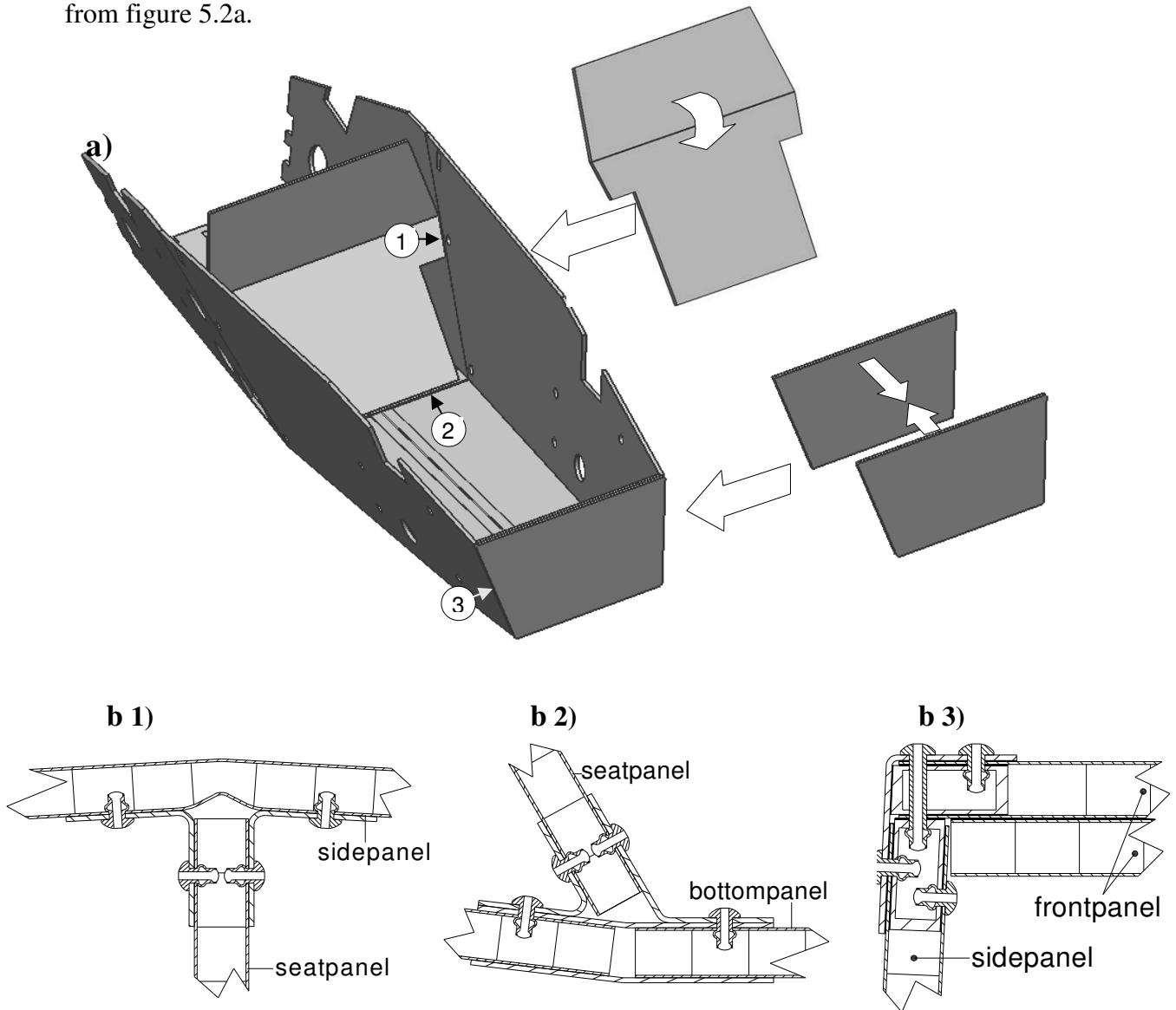
Figure 5.2 a: Placement of front and seatpanel   b: Attachment details

Detail b3 shows the joint of the double layer ALUCORE frontpanel and the sidepanel. The honeycomb structure will be locally removed on the edges and a milled rectangular section tube will be glued in. Blind rivets are used every 100-150 mm to localize and clamp the parts together for gluing. According to the glue manufacturer VIBA, the optimal glue layer thickness is 0.05-0.1 mm. Depending on surface levelness and roughness glue layers can be made as 0.01 mm.

5.1.3 Rearframe

The rearframe consists out of I-section profiles and will be milled out of a 25 mm thick aluminium plate. The monolithic rearframe will have a mass of 1.87 kg.

The rearframe will be used to attach the rearward connection rods to the chassis. In topview the connection rods meet the rearframe at different angles. The angles are calculated using Unigraphics and assimilated in the rearframe by milling six flat faces. The faces reach through slots in the sidepanels. These faces will later be used to bolt on mounting points for the connection rods. In this way a universal mounting point type can be used on all suspension connection points. The rules require a jacking point at the rear. Therefore a round tube is bolted onto the two milled blocks reaching through slots in the bottompanel. Figure 5.3 shows the rearframe and its placement in the chassis.
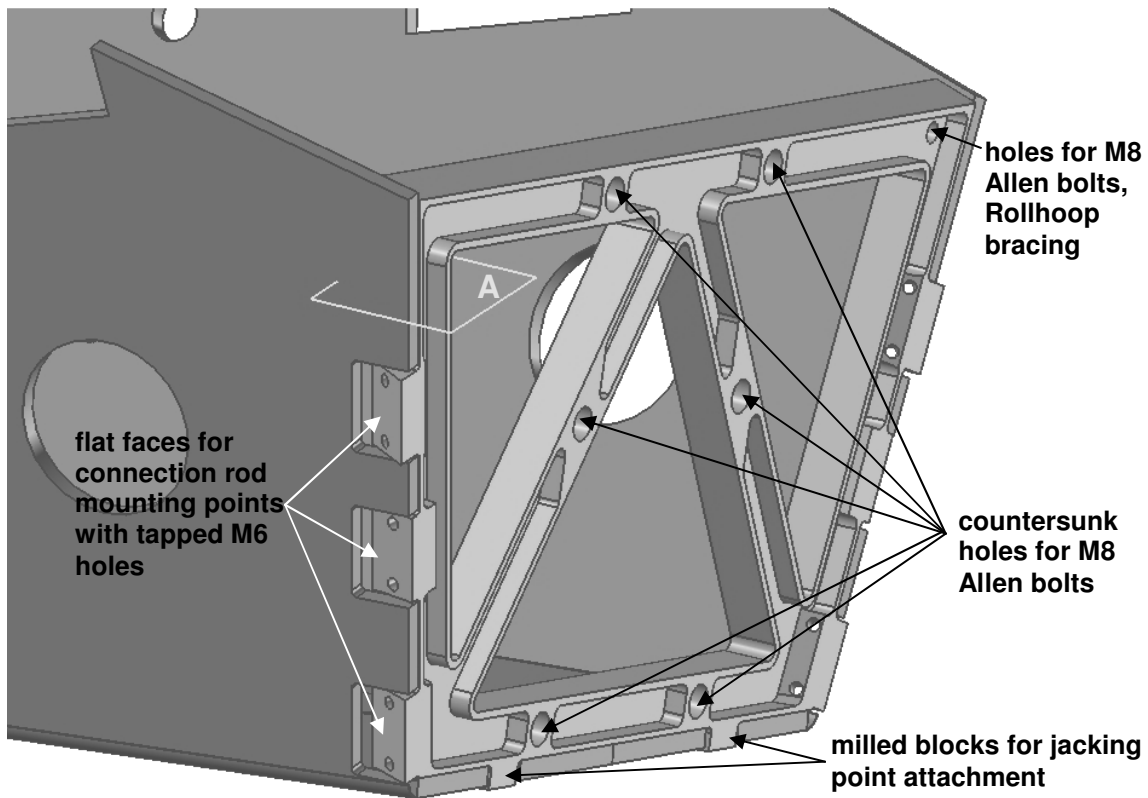
Figure 5.3: The rearframe and its placement in the chassis

The holes for the rollhoop bracing and the engine mounting plates are drilled. Figure 5.4 shows the attachment of the rearframe to the sidepanel and bottompanel in detail.

A milled rectangular tube is glued into the ALUCORE panel edges first. Then the rearframe is glued and blind riveted into the chassis.
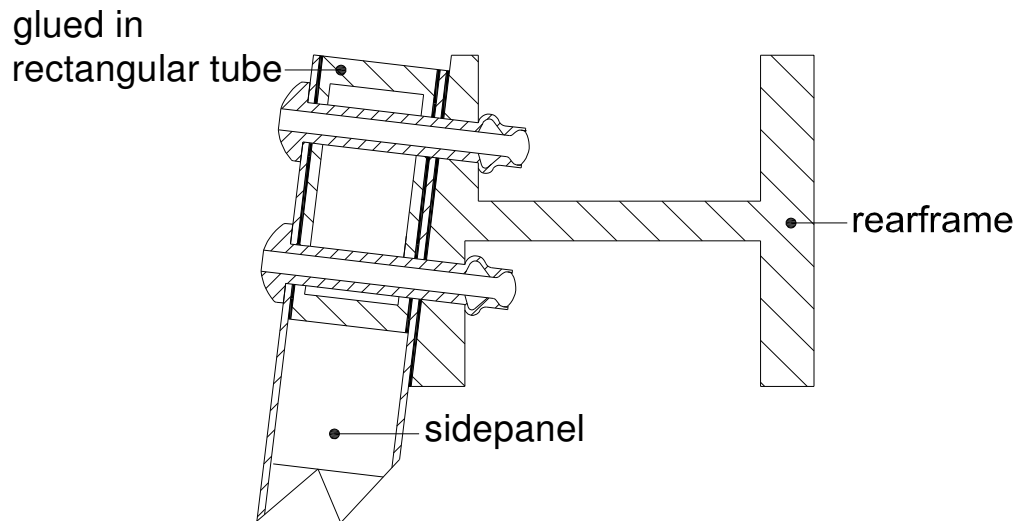
Figure 5.4: Rearframe attachment

5.1.4 Suspension support beams

On eight places the suspension connection rods are mounted on an insert in the sidepanel. To withstand the connection rod forces, support beams are placed on the inside of the sidepanels. These are drawn in figure 5.5.
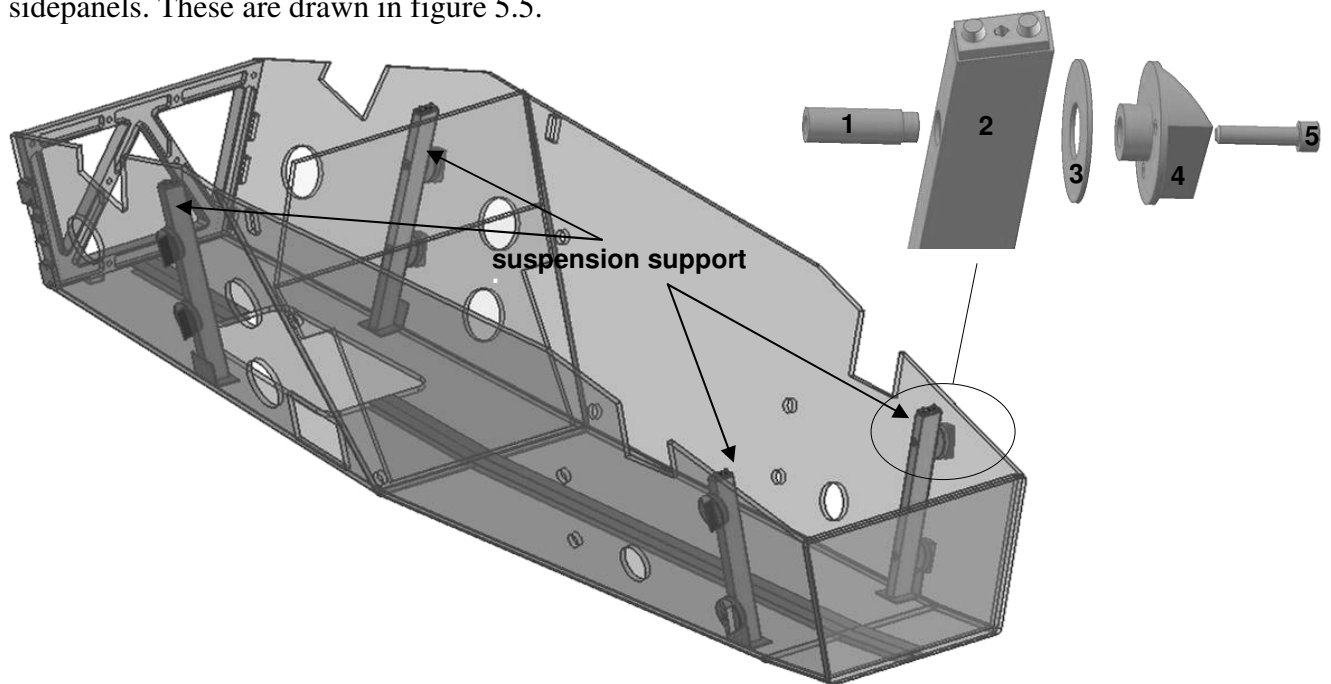
Figure 5.5: Suspension support beam placement with detailed attachment view

In the upper right of figure 5.5 an exploded view is drawn from the supportbeam connection rod attachment. Part 1 is an aluminium bush with inner M8 thread, which is welded into the standard 40x20x2 aluminium tube (part 2). Then an aluminium ring (part 3) is glued on tube (part 2). The tube with parts 1 and 3 is placed on the inside of the chassis and the insert (part 4) is put through a corresponding hole in the sidepanel and centered on part 1. Finally all is glued and secured by an Allen bolt. The insert is first machined by lathe. Due to the axi-symmetrical shape after turning, it is easy to clamp it

onto the milling machine and mill on a flat face with the right angle. This face is used later on for the attachment of the connection rod mounting points.

5.1.5 Torsion tubes

The torsion tubes are designed to have a maximum cross section area. Therefore a traverse cross section is made at the driver's elbows. This is depicted in appendix F. The torsion tubes are made out of 5052 aluminium alloy plate of 1 mm thickness. Figure 5.6 shows the layout and placement of the torsion tubes.

seam

seam
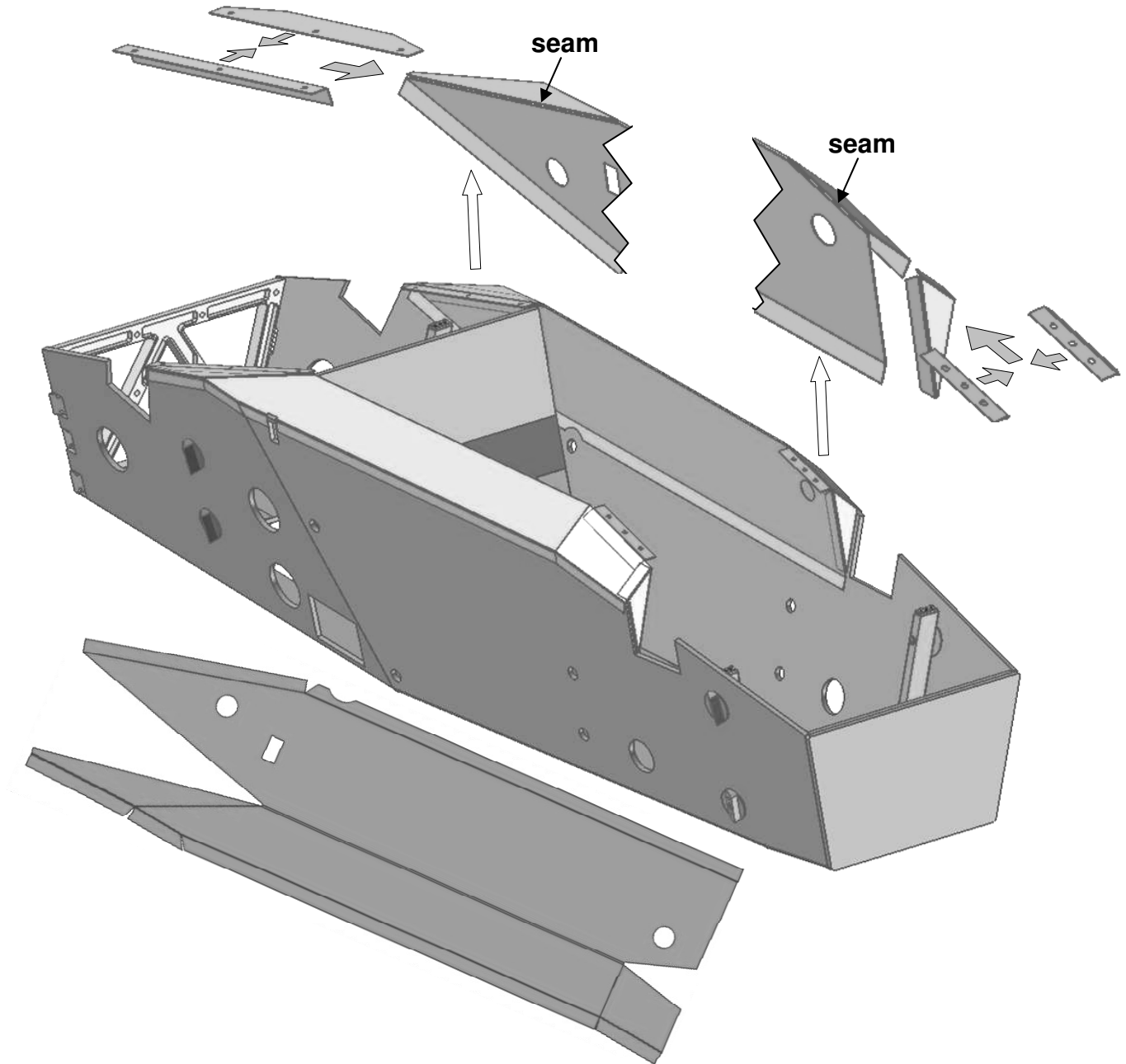
Figure 5.6: Torsion tube layout, placement and sub-parts

The torsion tube also has two flaps attached; these will be used for the mounting of the front and rear cover plates. The flaps are made out of two layers of 1mm thick aluminum plate. This is glued into the torsion tube seams this is depicted in figure 5.7a. Then the torsion tube is glued onto the sidepanel. Figure 5.7b shows the cross-section of the torsion tube attached to the sidepanel.
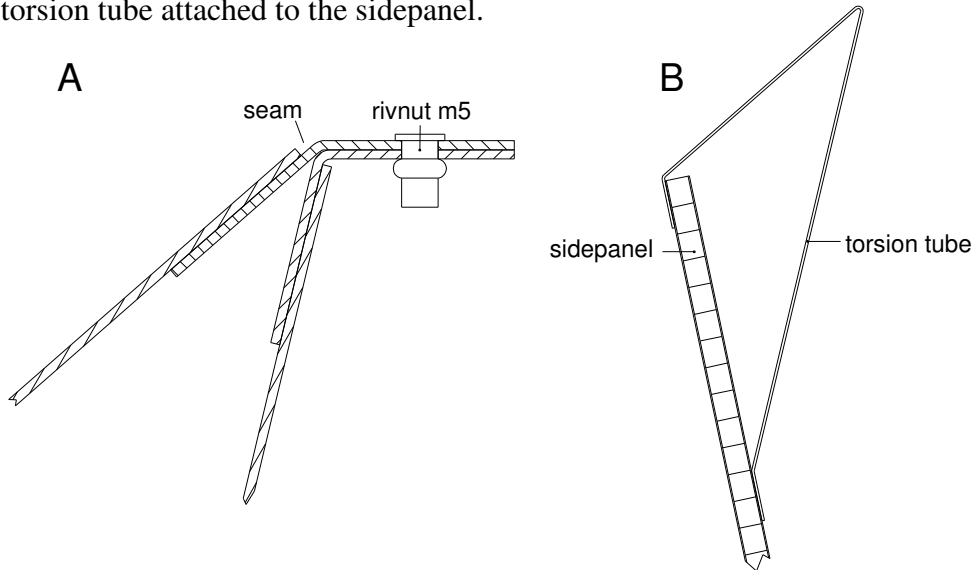
Figure 5.7   a: Glued in flaps   b: Sidepanel - torsion tube attachment

5.1.7 Front and rear roll hoop

The front and rear roll hoops have to extend from the lowest frame member on one side of the chassis, up over and down to the lowest frame member on the other side of the chassis. The top-most surface of the front hoop must extend above the top of the steering wheel. Furthermore the roll hoops must be made out of 25x2.5mm round steel tube. The roll hoops are placed outside the chassis. This makes it easy to attach and detach them and it will also be used to mount the front wheel connection rods to the chassis. Figure 5.8 shows the chassis with the roll hoops.
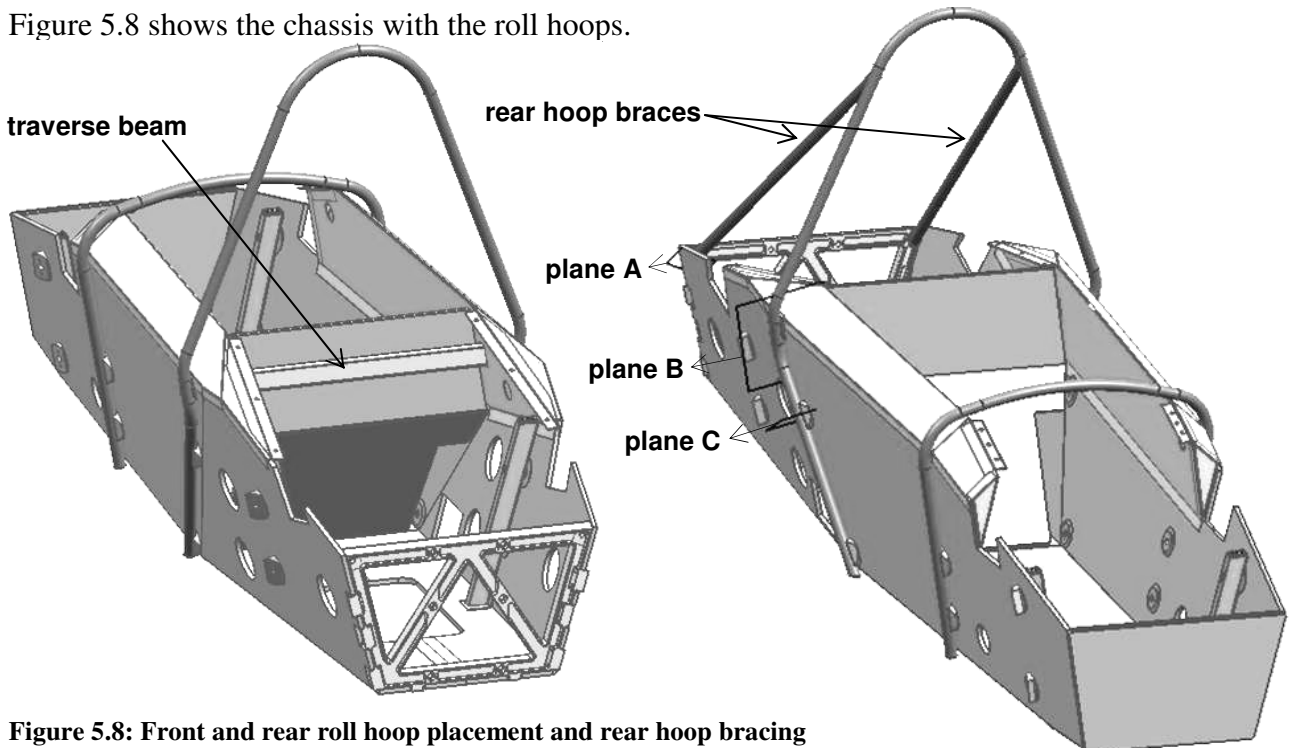
Figure 5.8: Front and rear roll hoop placement and rear hoop bracing

The roll hoop connection details are shown in the cross sections through plane a, b and c in figure 5.9.a, b and c.

a)
- M10 Allen bolt
- rearframe
- welded on endplate
- M10 Nut
- roll hoop brace

b)
- rear roll hoop
- aluminium traverse beam
- cylinder with thread
- M8 Allen bolt
- welded in aluminium block
- welded in steel bush

c)
- insert part 1
- roll hoop
- section nut
- M8
- insert part 2
- M8 Allen bolt
- sidepanel
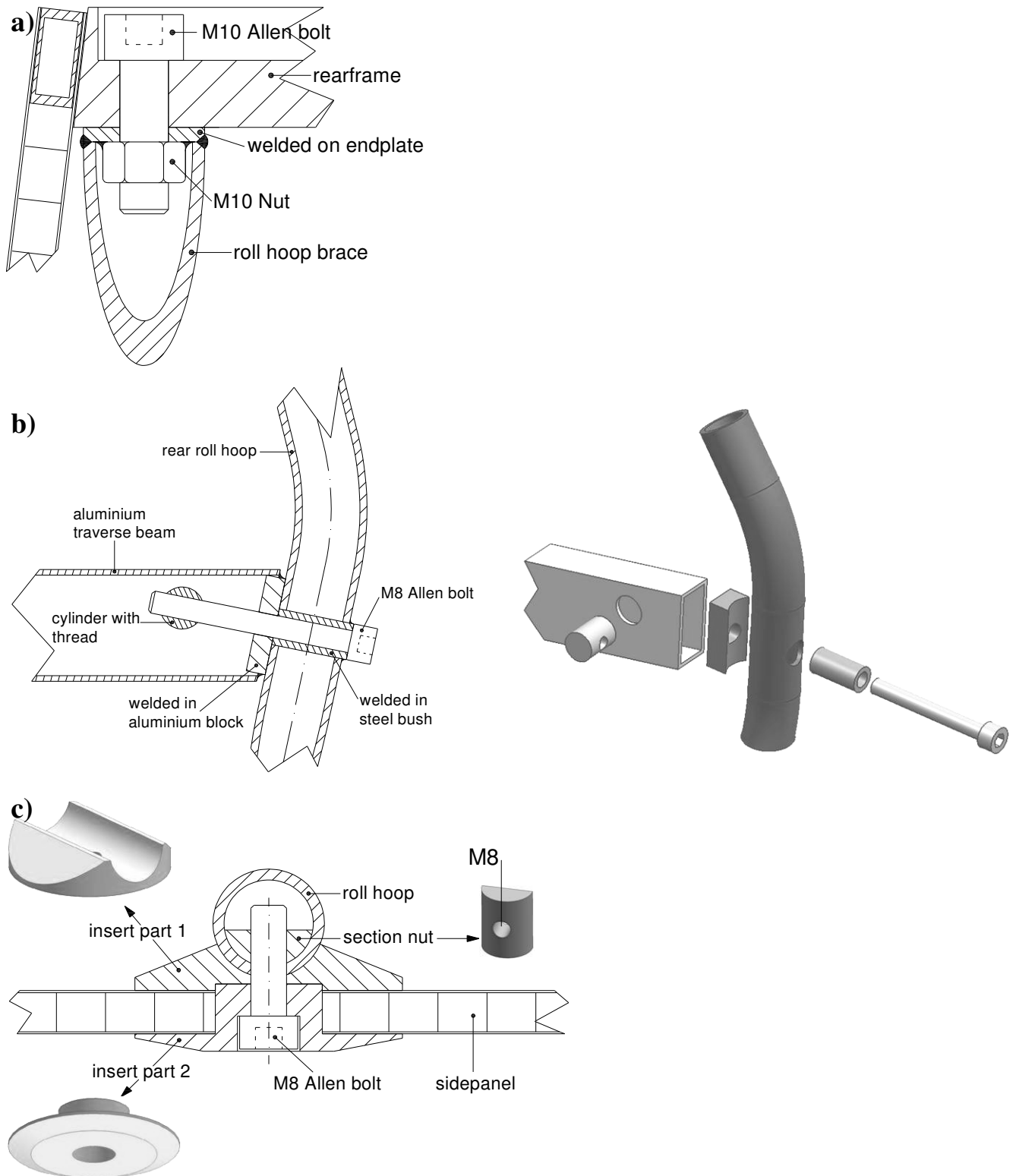
Figure 5.9 a: Cross section plane a   b: Cross section plane b   c: Cross section plane c

5.1.8 Dashboard

The dashboard will be part of the chassis structure. It will be a sandwich structure consisting of two 1 mm thick aluminium plates with a 25 mm thick polyurethane core. Figure 5.10 shows an exploded view of the dashboard.

dashboard frontplate

dashboard PU-foam

large hole for steering transmission

dashboard rearplate
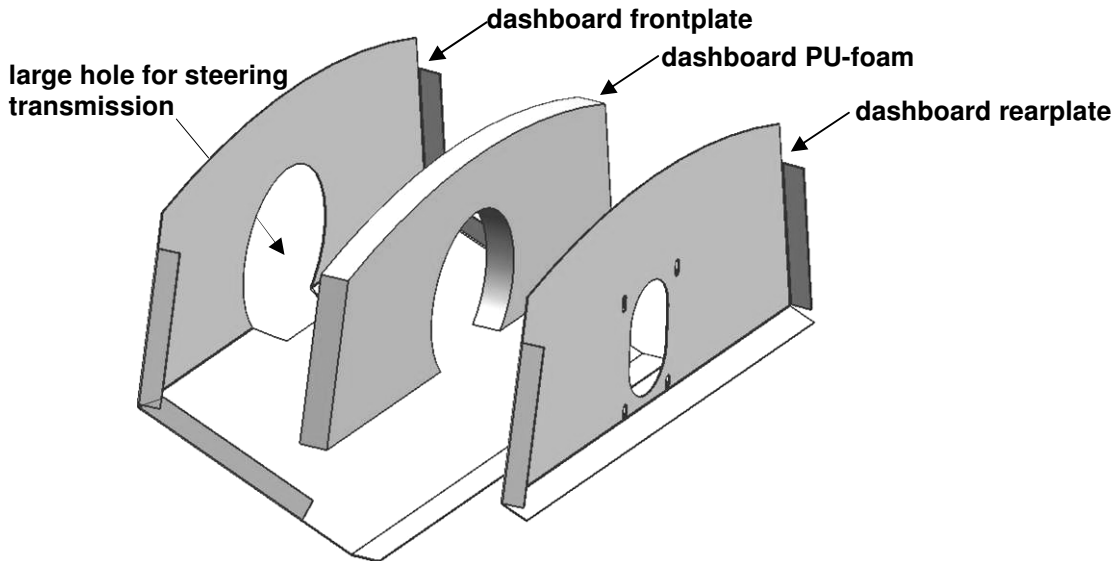
Figure 5.10: Exploded view of the dashboard

The top edge of the dashboard will be mounted onto the front roll hoop. The middle top part of the front roll hoop will be sandwiched by the front and rear dashboard plates using glue and blind rivets. The large round hole in the frontplate of the dashboard will later be used to countersink the steering transmission onto the dashboard. The weakened frontplate will be closed by adding a covering plate over the steering transmission, this will be shown later. The large flange on the dashboard frontplate extending forward also reinforces the frontplate around the large hole. Furthermore this flange is attached to the suspension box and adds stiffness to the chassis structure. Figure 5.11 shows its placement in the chassis.

glued and blind riveted
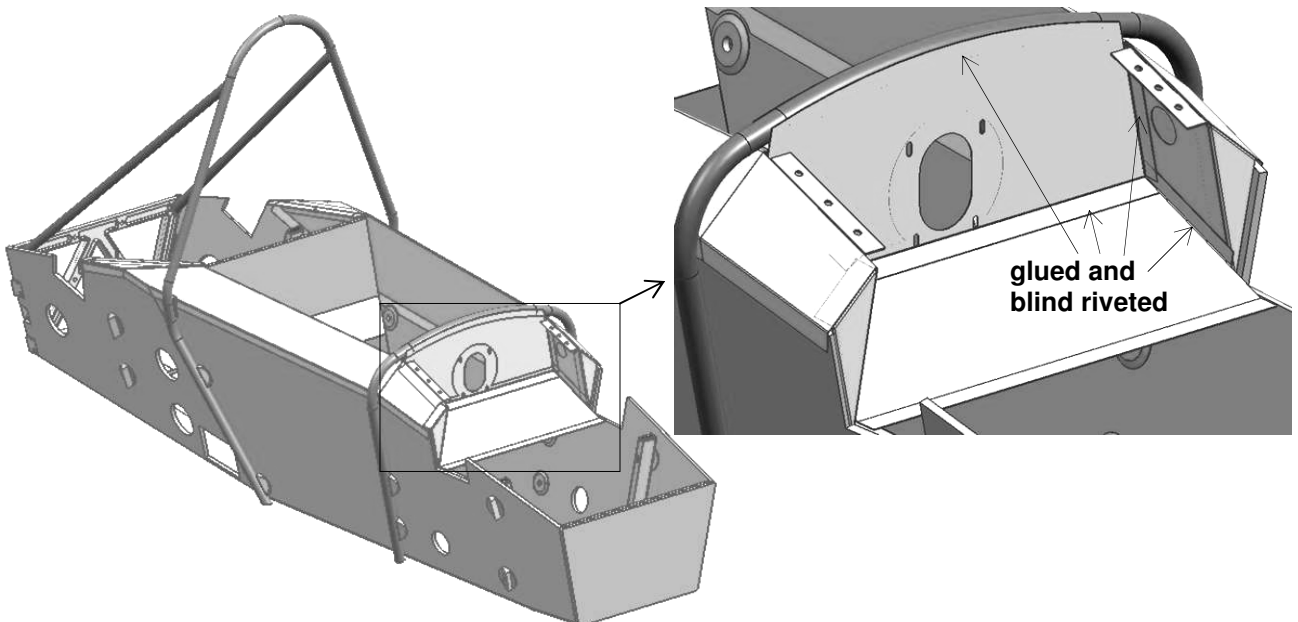
Figure 5.11: Dashboard placement and attachment

5.1.9 Rear and front covering plates

The chassis is still a box without a cover. To finalize the structure covering plates are added front and rear. Furthermore traverse beams are added front and rear to the structure to distribute the connection rod forces into the covering plates. The traverse beams are made out of standard 40x20x2 mm aluminium rectangular tube. They are attached on top of the support beams and can easily be detached to reach the engine and pedalbox if necessary. The front traversebeam are depicted in figure 5.12.
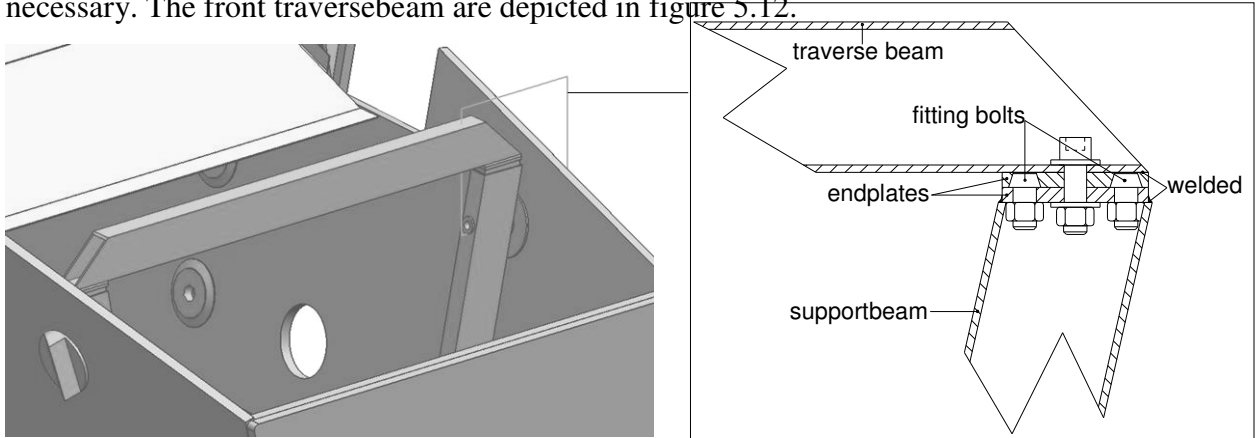
Figure 5.12: Attachment traverse beams onto support beam

Both the support beam and the traverse beam have a 4 mm thick welded endplate. The support beam endplate has three 6 mm holes. Two holes are used for M6 fitting bolts. The fitting bolts fit into tapered holes in the traverse beam endplate and are for positioning the traverse beam. A long M6 bolt is used to tighten it all together.
At the rear suspension support beams a similar traverse beam is added.
The traverse beams will be used to mount on the rear and front covering plates. The covering plates will be attached using rivnuts placed into the supporting edges.
A total of four plates will be used to close the structure; this is shown in figure 5.13.
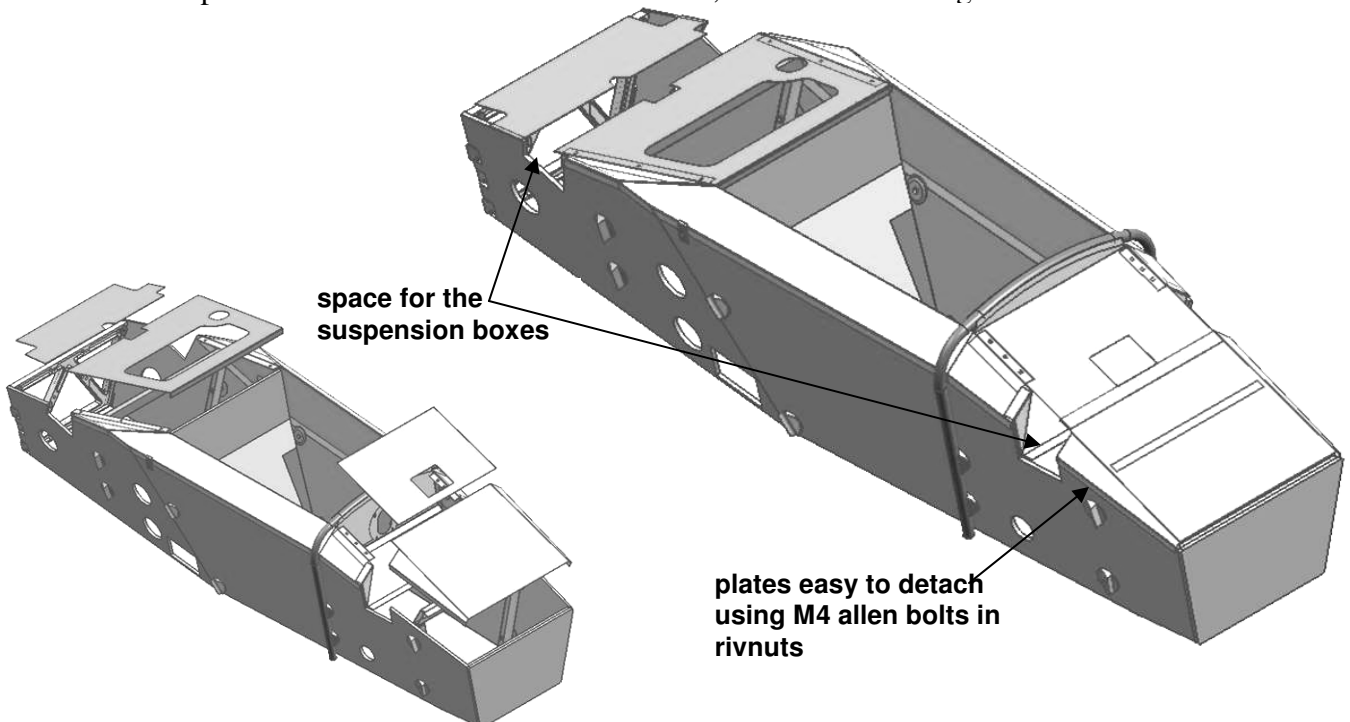
Figure 5.13: Front and rear covering plates

5.2 Side impact and sloped floorpanel assembly

The rules require a side impact system. It should extend from the front to the rear roll hoop. Furthermore it should reach at least up to 300 mm above ground. The FSRTE02 side impact will be made out of plate material glued into the chassis.
Figure 5.14 shows the cross section.
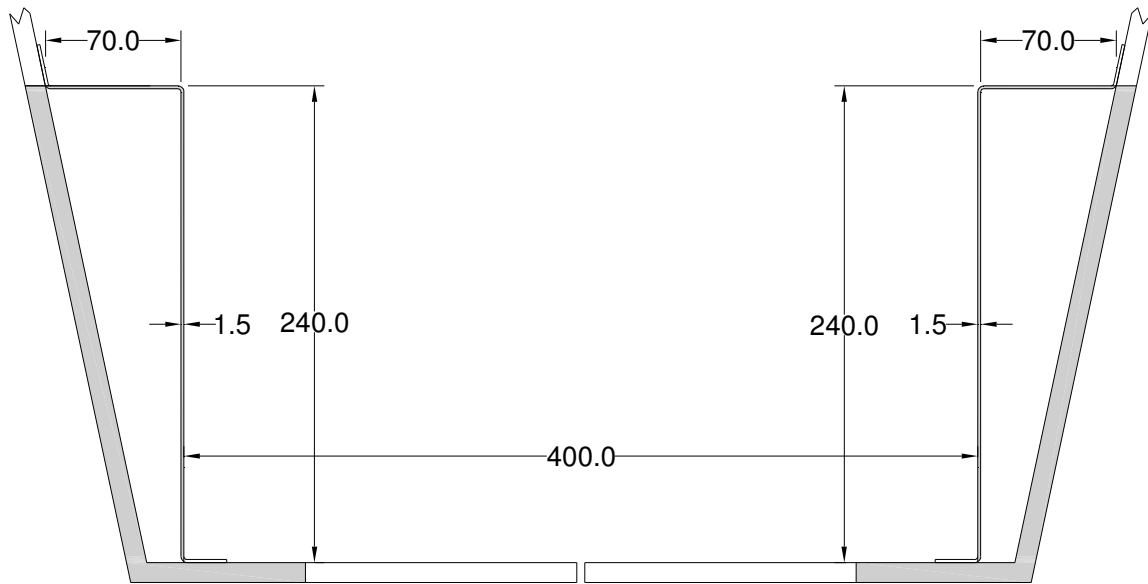
Figure 5.14: Side impact cross section

It should be equivalent to a side impact using tubular members stated in the rules therefore the second moment of area is compared. The grey sections in figure 5.14 are equivalent to the required tubular side impact structure.

To protect the steering rack and transmission a sloped floor panel is added. This floorpanel also prevents the side impact tubes from crushing the driver's legs in a side impact. Figure 5.15 shows the folding of the sloped floorpanel. The floor panel will be made out of 1 mm thick aluminium plate. The driver will enter the car by stepping onto the sloped floorpanel, to reinforce the floorpanel a plate of ALUCORE panel is glued underneath.
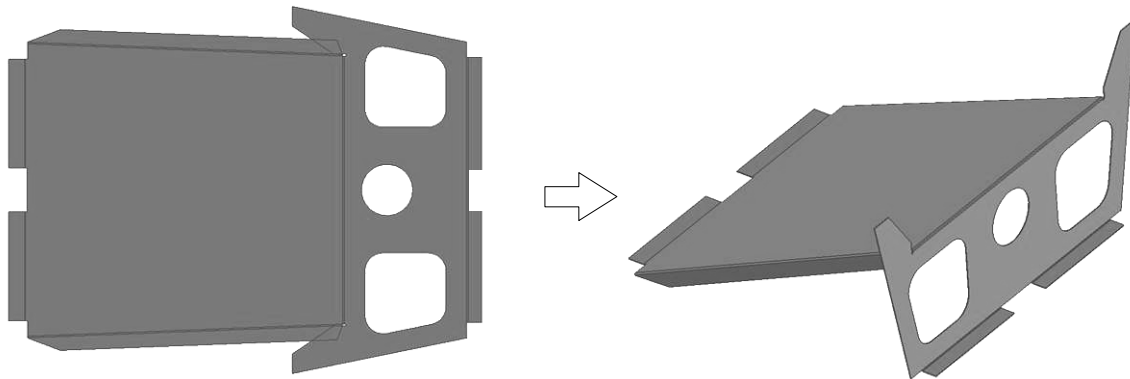
Figure 5.15: Sloped floorpanel layout and folded sloped floorpanel

The lay out of the side impact tubes is shown in figure 5.16. It also shows the chamfer needed for the driver's knees. Furthermore a hole is added to attach the seatbelt on the

side impact and the lower insert for the rear roll hoop attachment. There will be made two side impact tubes, one for the left and one for the right.

hole for seat belt mounting

chamfered corner for knee support
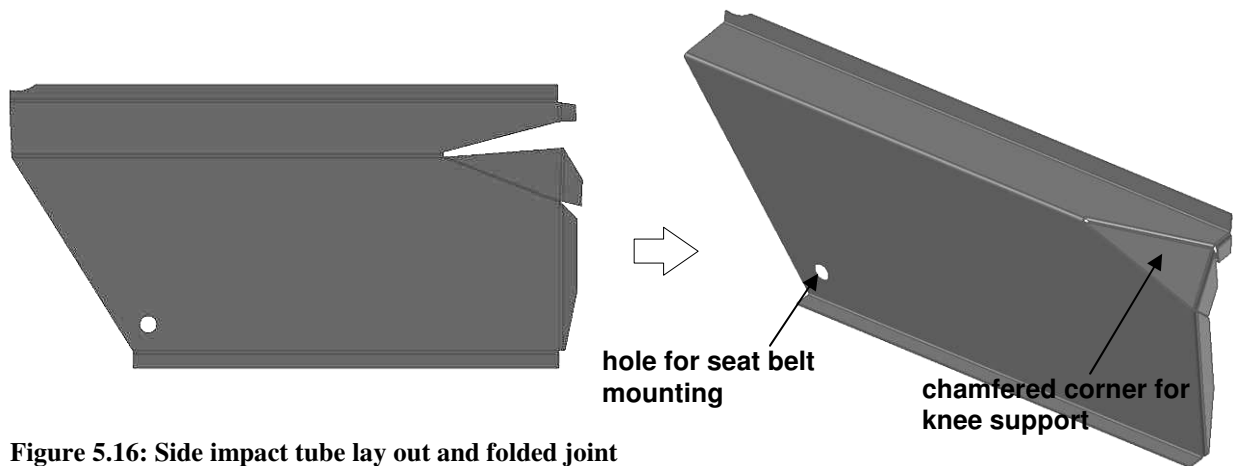
Figure 5.16: Side impact tube lay out and folded joint

Figure 5.17 shows the assembly of the sloped floorpanel, the side impact, the side impact traverse plates and the 25x25x1.5 mm tube. The traverse plates are glued into the side impact tubes. These plates will prevent the tube from being crushed in a side impact. The aluminium 25x25x1.5 mm tube is used to connect the side impact to the front rollhoop through the inserts.

side impact traverse plates

25x25x1.5 aluminium tube
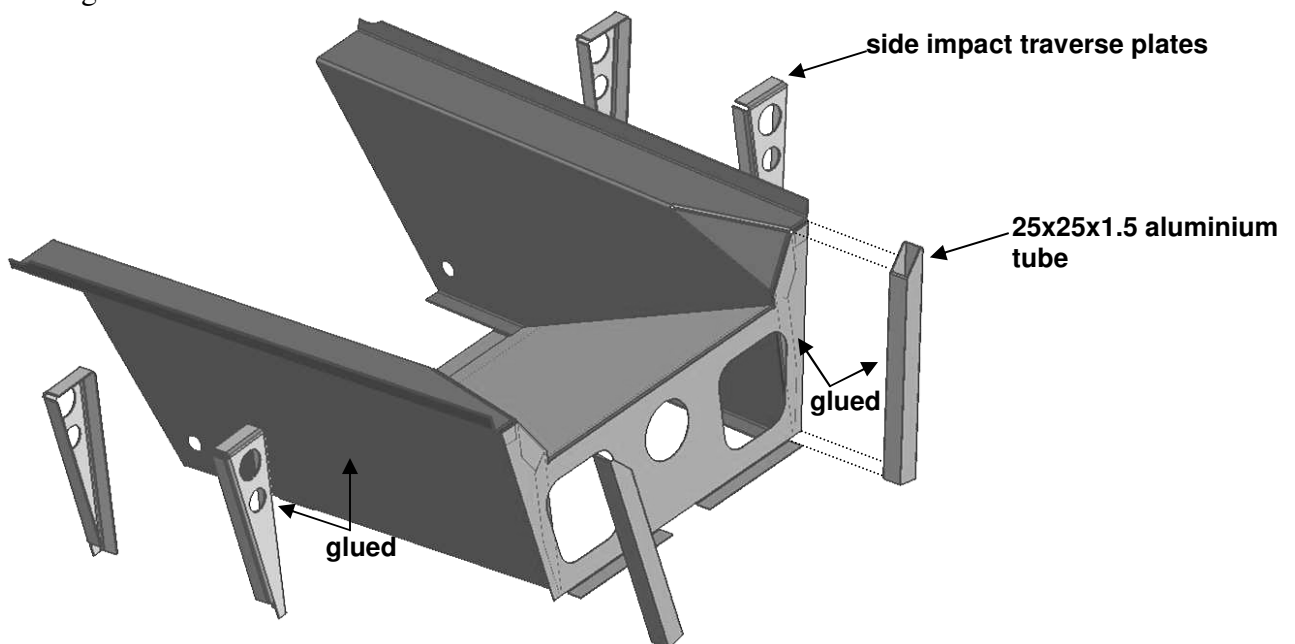
glued

glued

Figure 5.17: Sloped floorpanel and side impact assembly

Figure 5.18 shows the sloped floorpanel and side impact assembly placed in the chassis.
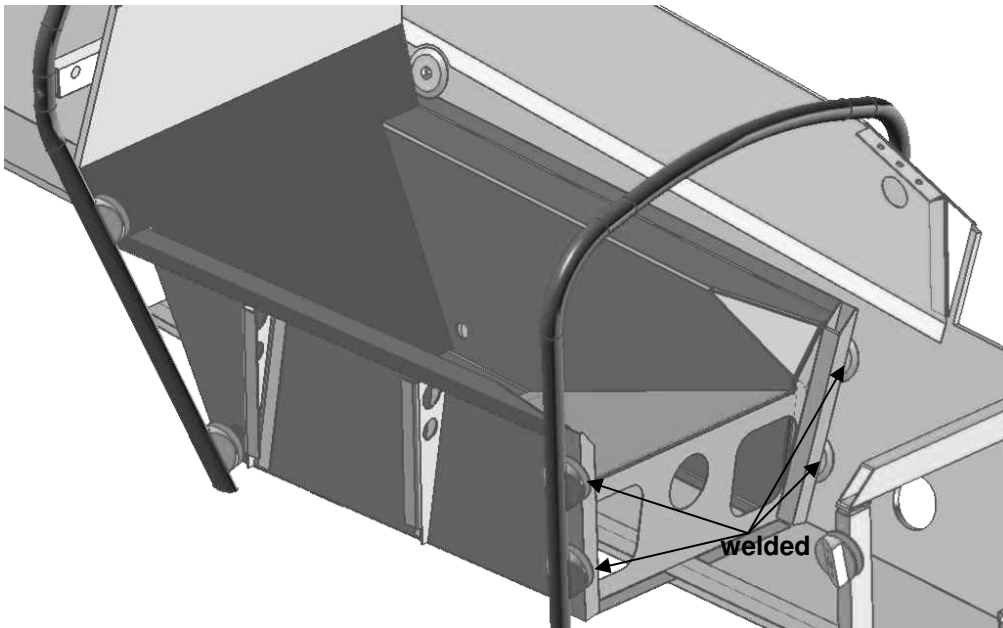
welded

Figure 5.18: Sloped floorpanel and side impact placement

All is glued and blind riveted where necessary except for the square 25x25x1.5 mm tubes, these are welded onto the inserts.

5.3 Steering system

The applied steering system is a pinion with a steering rack. This system is easy to use; it can be built in everywhere. The transmission from the steering wheel to the steering rack will must be free of play and must have a high stiffness for direct steering. This way the driver can exactly feel the tire behavior though the vibrations on the steering wheel. Therefore a system with four eccentric disks is used. Figure 5.19 shows the system.
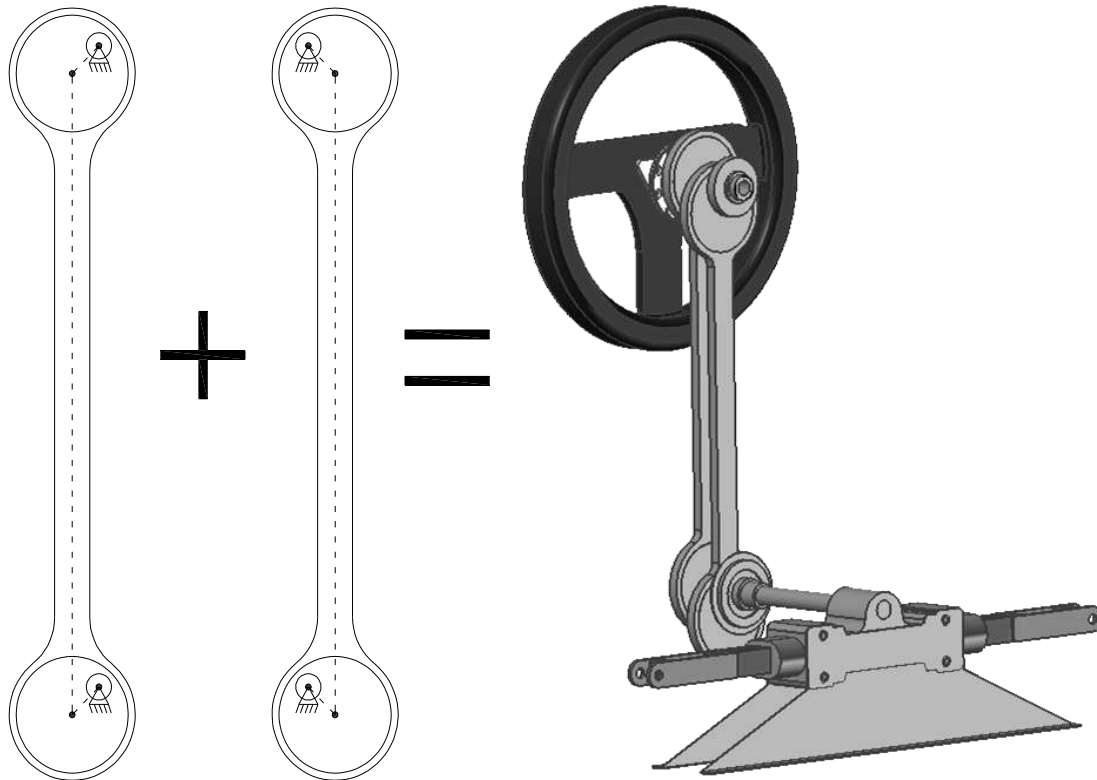
Figure 5.19: Steering transmission with four eccentric disks

The steering wheel shaft and the steering rack shaft are parallel; on both shafts two eccentric disks are mounted. Two opposite disks and one ring ended bar can be considered as a "four bar system". The disadvantage of a four bar system is that it can only transmit a rotation angle<180°, larger angles will make the system to lock (all bars are aligned). This can be solved by using two "four bar systems" with a phase difference of 90°. If one system is in locking position, the other system is in its best position and vice versa. The steering system uses eccentric disks instead of bars, the disks are made out of aluminum and use special coating to minimize friction. The mechanism is mounted into an aluminum housing made out of two symmetrical halfs. The mechanism is over-determined with four parts determining the distance between the steering wheel shaft and the steering rack shaft. Therefore the mechanism has to be manufactured very accurate. By stacking up the parts that fix the shaft to shaft distance and bore through all parts together, problems are prevented.

The steering transmission is very flat and will be placed in a flat 25 mm thick housing. Then the steering transmission is placed into the chassis. This is shown in figure 5.20
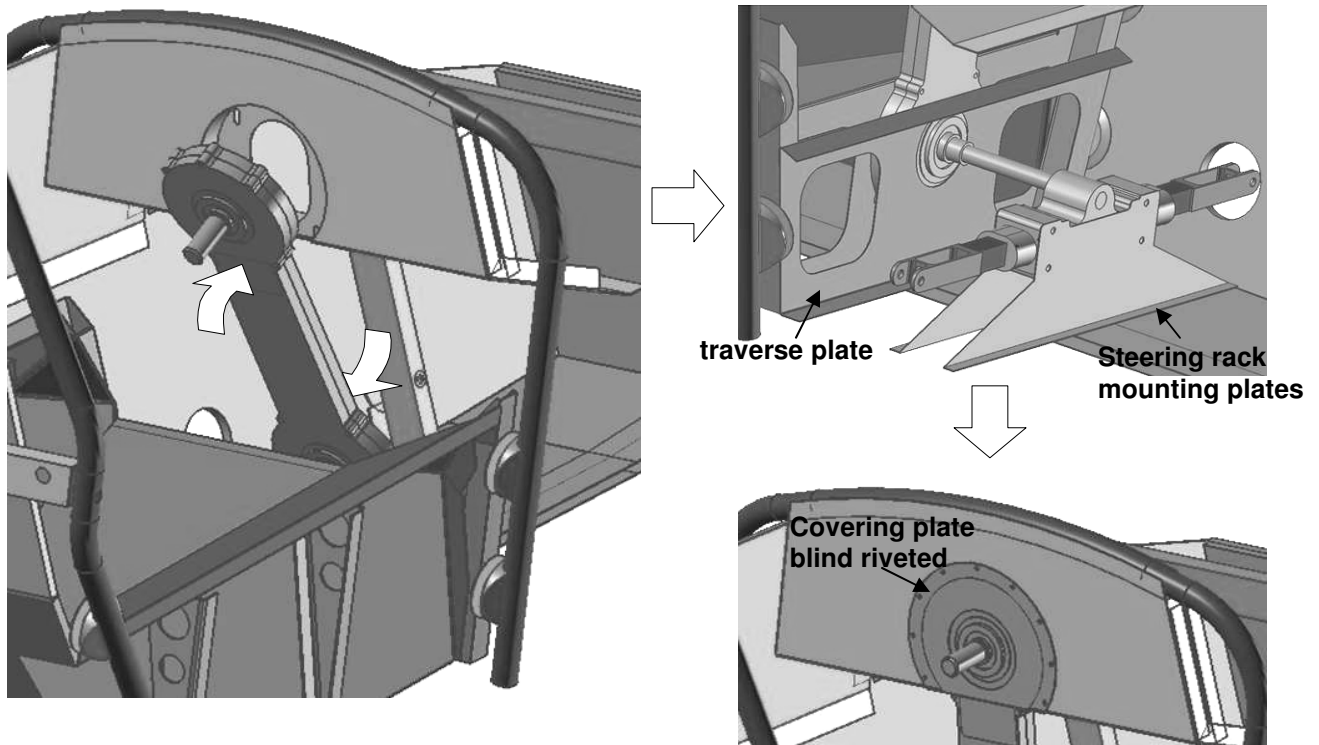
Figure 5.20: Placement and attachment steering system

The order of placement is indicated by the arrows. First the transmission is tilted in. Subsequently the transmission is sandwiched by a traverse plate mounted onto the 25x25x1.5 mm tubes with rivnuts for easy disassembling. The steering rack is placed using two mounting plates glued onto the bottom panel. Then the steering rack shaft is connected to the transmission. After they have been aligned the steering rack and the transmission are fixed using bolts. Finally a covering plate is placed closing the hole in the dashboard and the transmission is fixed completely using four bolts that go through the covering plate, the transmission and the dashboard rear plate.

To protect the steering rack a second sloped floor panel is placed, shown in figure 5.21.
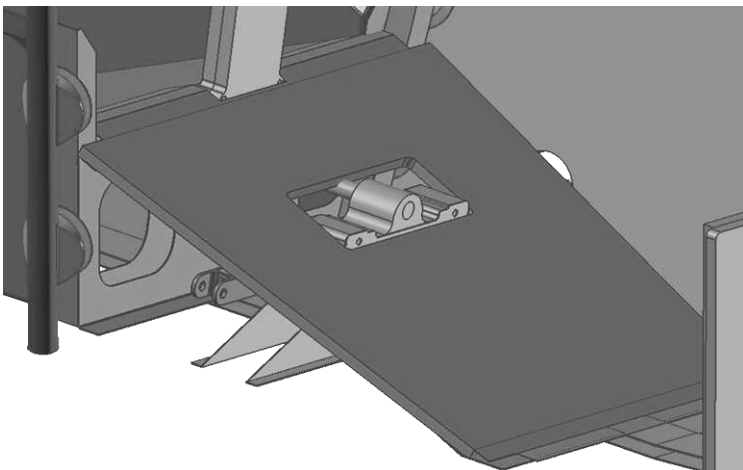
Figure 5.21: Second sloped floorpanel for steering rack protection

This panel will be attached using rivnuts, this way it is easy to remove the panel to reach the steering rack and the transmission.

5.4 Power train and drive train

The engine is the heart of the powertrian. The Suzuki engine is accurately modeled using Unigraphics. Therefore the mounting points have been measured exactly. Figure 5.22 shows the modeled engine.
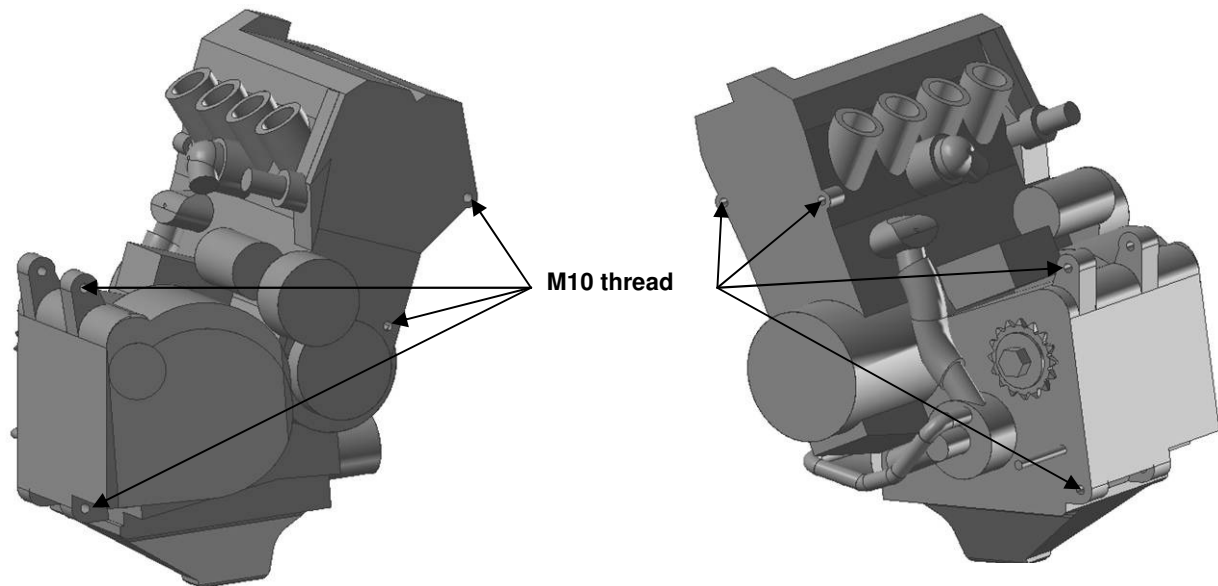
Figure 5.22: Suzuki engine mounting points

The car will be driven using a chain, other final drives like a timing belt will be heavier. The differential will be a Torsen type differential. Using a single brake disc mounted onto the differential. When accelerating tensile force will be generated in the chain this force should be lead through the rear sprocket, the differential and the differential bearings back to the engine. Therefore two aluminium plates are used mounted onto the rearward four engine mounting points. Figure 5.23 shows a topview of these plates together with the differential, both sprockets and the brake disk. The actual design of the differential housing and bearing, drive shafts, sprocket flange and braking system is done by formula student team members and is therefore not discussed extensively.

1	Torsen differential	7	bearing mounting ring 2
2	differential housing	8	bearing mounting ring 3
3	differential covering plate	9	connection tube
4	sprocket flange	10	radial needle bearing
5	brake disk flange	11	combined radial and axial bearing
6	bearing mounting ring 1	12	oil seal
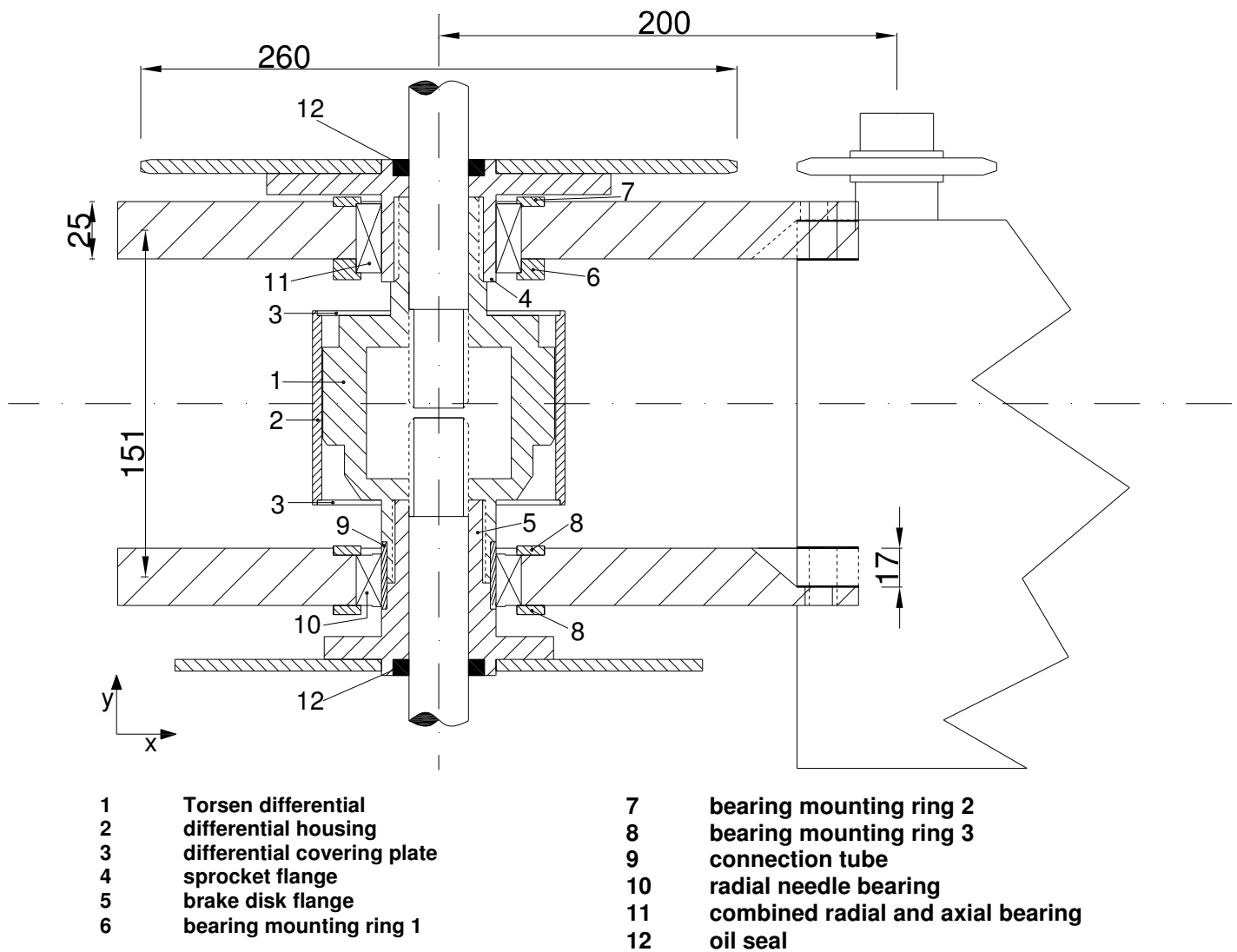
Figure 5.23: Topview of differential mounting plates with differential, sprocket and brake disk

The differential mounting plates are 25 mm thick. This way a deep pocket can be milled into the plate to meet both engine mounting faces having an offset of 17 mm in y-direction. If the 25 mm thick plates would be massive each plate would have a mass of 5.7 kg. By milling away 75 % of the material the plate will have a mass of 1.45 kg. The right plate will also be used to mount the brake caliper. The drive shafts are chosen hollow with an outer diameter of 26 mm. Furthermore flex-plates are used to transmit the torque to the wheels over the whole suspension travel.

As the wheel travels there will be approximately 1 mm of axial shaft displacement, which can also be absorbed by the flex-plates.

Figure 5.24 shows the exploded view and an assembled view of the complete drivetrain.
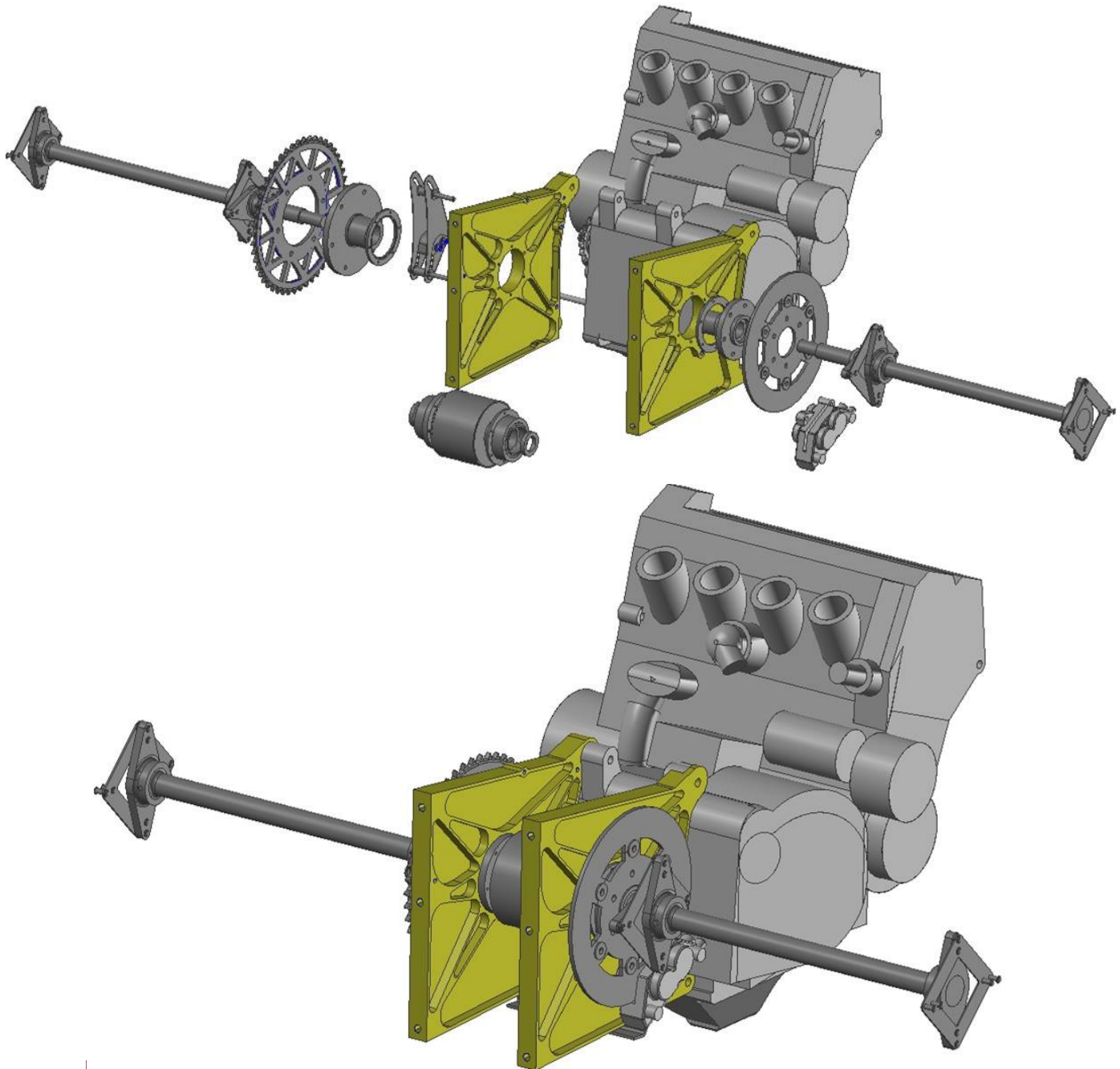
Figure 5.24: Drivetrain exploded view and assembly

To mount the drive train in the chassis, some brackets have been added bolted onto the four frontward engine mounting points. Furthermore a brace is added to mount the differential plates to the bottom panel in lateral direction, to prevent the plates from working like a parallelogram due to lateral inertia forces. Figure 5.25 shows these brackets and the placement of the engine in the chassis.
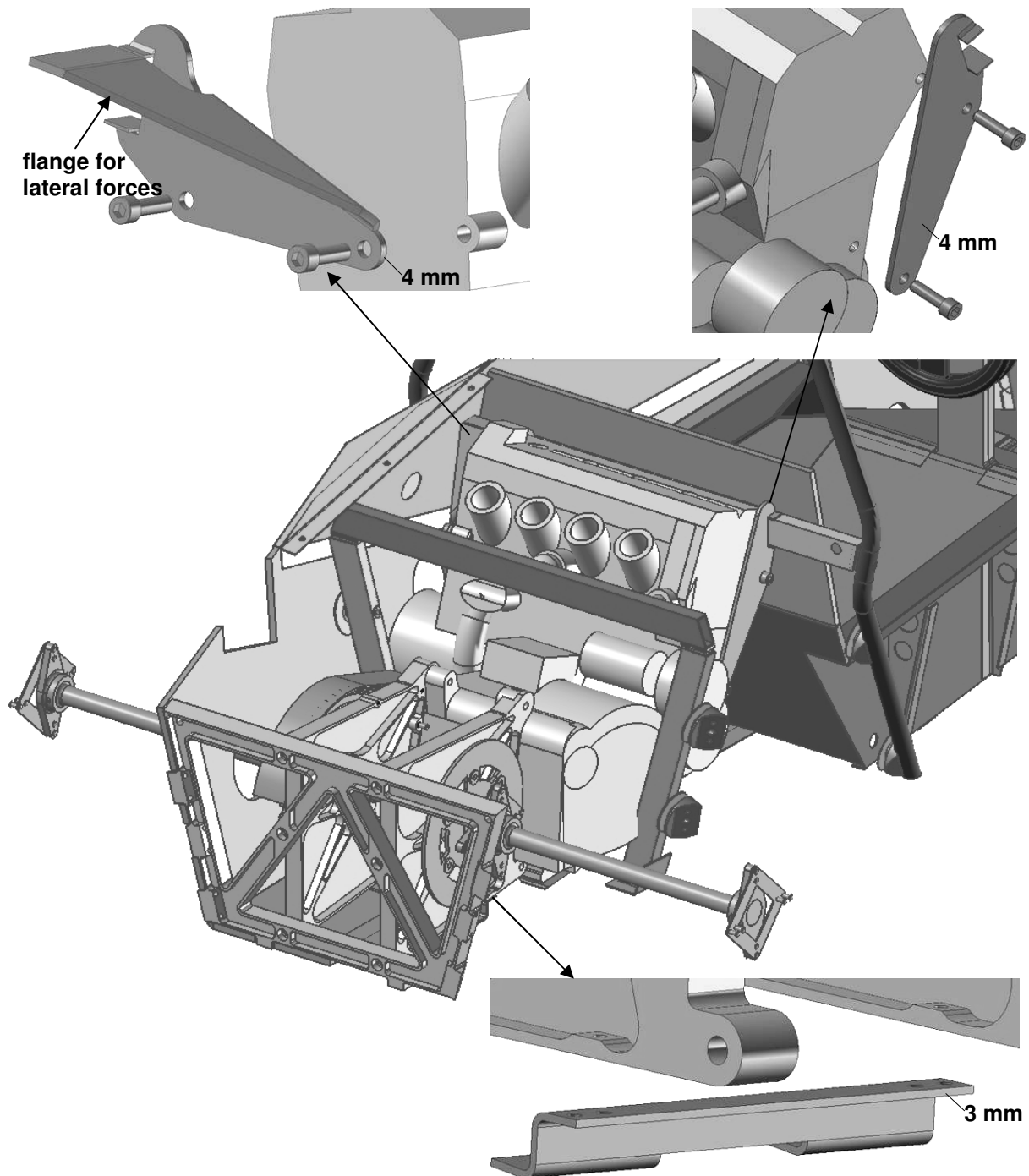
Figure 5.25: Placement and attachment drivetrain and engine

The front engine brackets will be mounted onto the traverse beams behind the seatpanel. The forces are transmitted to the rear roll hoop and to the seatpanel. The powertrain is completed by adding the fuel tank, the battery and the radiator.

The battery is placed on the right as close a possible to the starter motor. This way cables are kept short so little voltage is lost and weight is saved. The battery can be reached through a hole in the sidepanel. The hole will be closed again by a cover, bringing back the sidepanel stiffness. The fuel tank is chosen 6 liters and placed left.

Figure 5.26 shows the placement of the fuel tank and the battery.

heat shield

fuel
tank
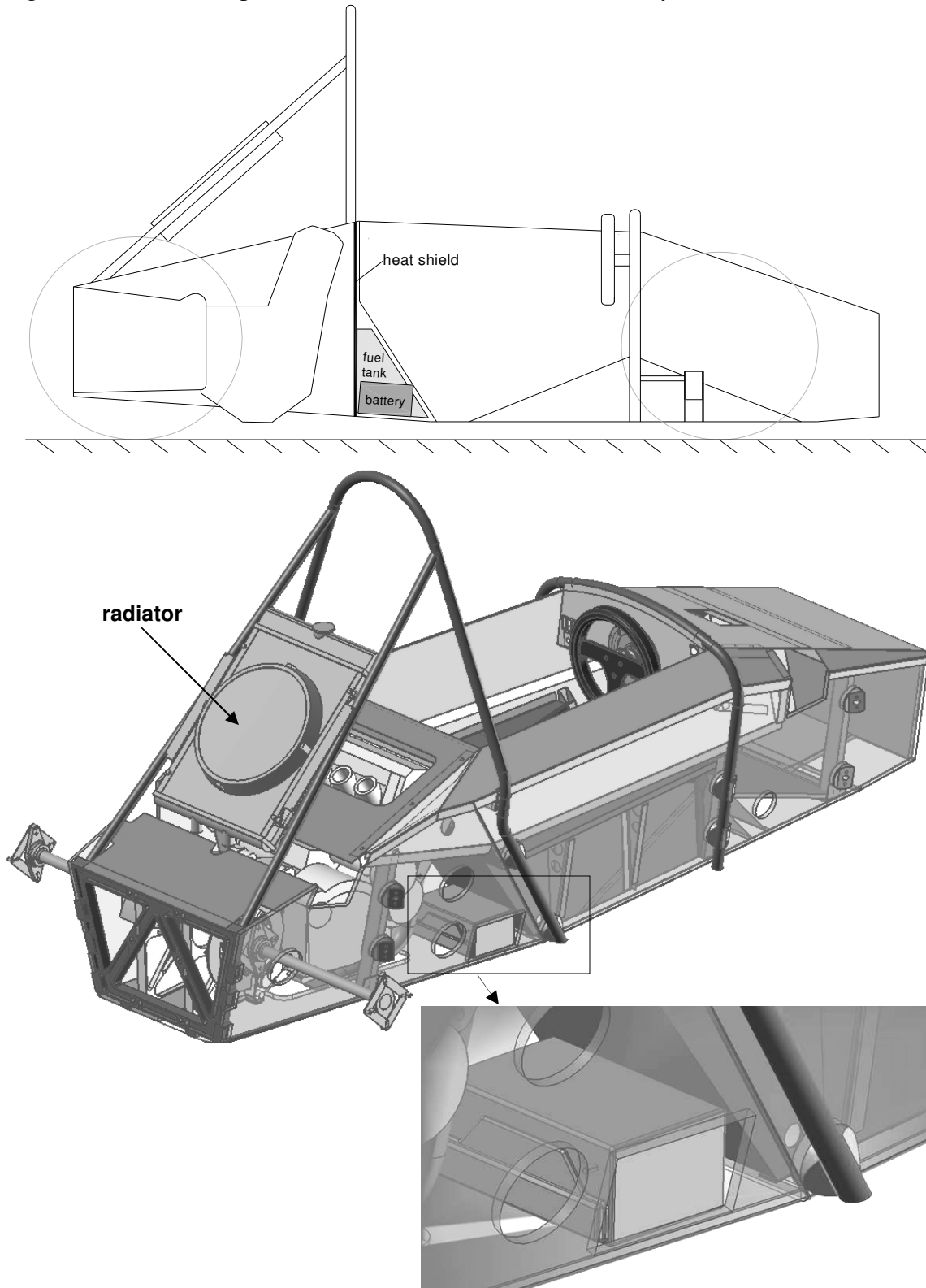
battery

radiator

Figure 5.26: Placement of battery, fuel tank and radiator

6 Suspension design

The suspension properties were determined in chapter 4. In this chapter the suspension with these properties will be designed fitted onto the chassis. First the suspension center lines are determined.

6.1 Suspension center lines

The suspension center lines are drawn onto the chassis using AutoCAD coordinates in the Unigraphics model. All properties are determined at ride height (ground clearance 50 mm) therefore the suspension centerlines are given at ride height. Figure 6.1 shows the chassis with the centerlines. The corresponding coordinates are given in appendix G.
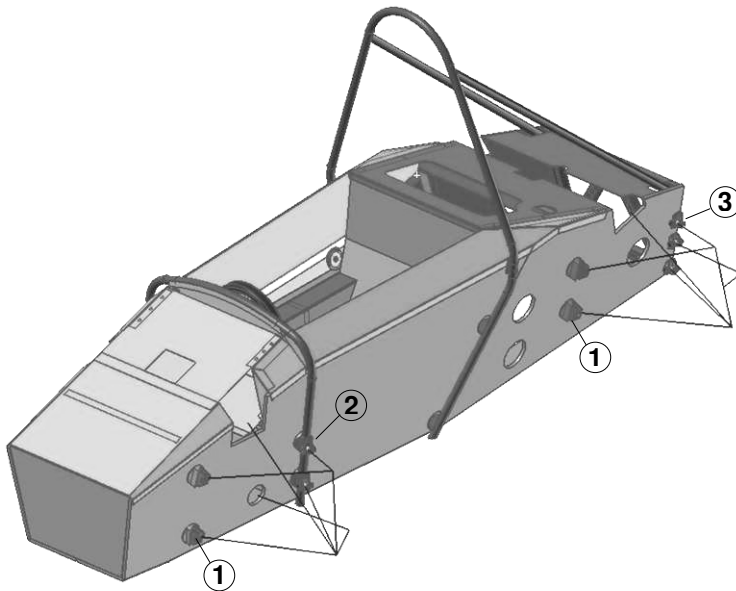
Figure 6.1: Suspension center lines

The pushrod lines are pointing toward the empty spaces in the chassis. In these spaces the suspension boxes will be placed.

6.2 Chassis connection points

Every wheel has six connection rods. Four rods have to be mounted to the chassis using spherical joints fixing four degrees of freedom (d.o.f). One rod is connected to the chassis by the bump stiffness fixing the 5th d.o.f. The last rod is the steering rod and can be controlled by the driver, fixing the 6th d.o.f. At the rear the steering rod is called tie rod and can be adjusted to align the wheels for toe in or toe out. The used spherical joints will be standard INA rod ends. These rod end will be placed in vertical direction, as the wheel travels the rod end will rotate in the right direction. The rod end specifications can be found in appendix H. The numbers in figure 6.1 refer to the different mounting point types. The different types will be show and explained in paragraph 6.2.1, 6.2.2 and 6.2.3.

6.2.1 Mounting point "type 1"

Mounting point "type 1" is used at the suspension support beams. Figure 6.2 shows a cross section of this mounting point.

1	welded in bush	6	bolted on U-profile
2	M8x50 Allen bolt	7	rod end
3	suspension support beam	8	tapered offset washer
4	ring (glued to side panel and beam)	9	M8x35 Allen bolt
5	insert with angled face		
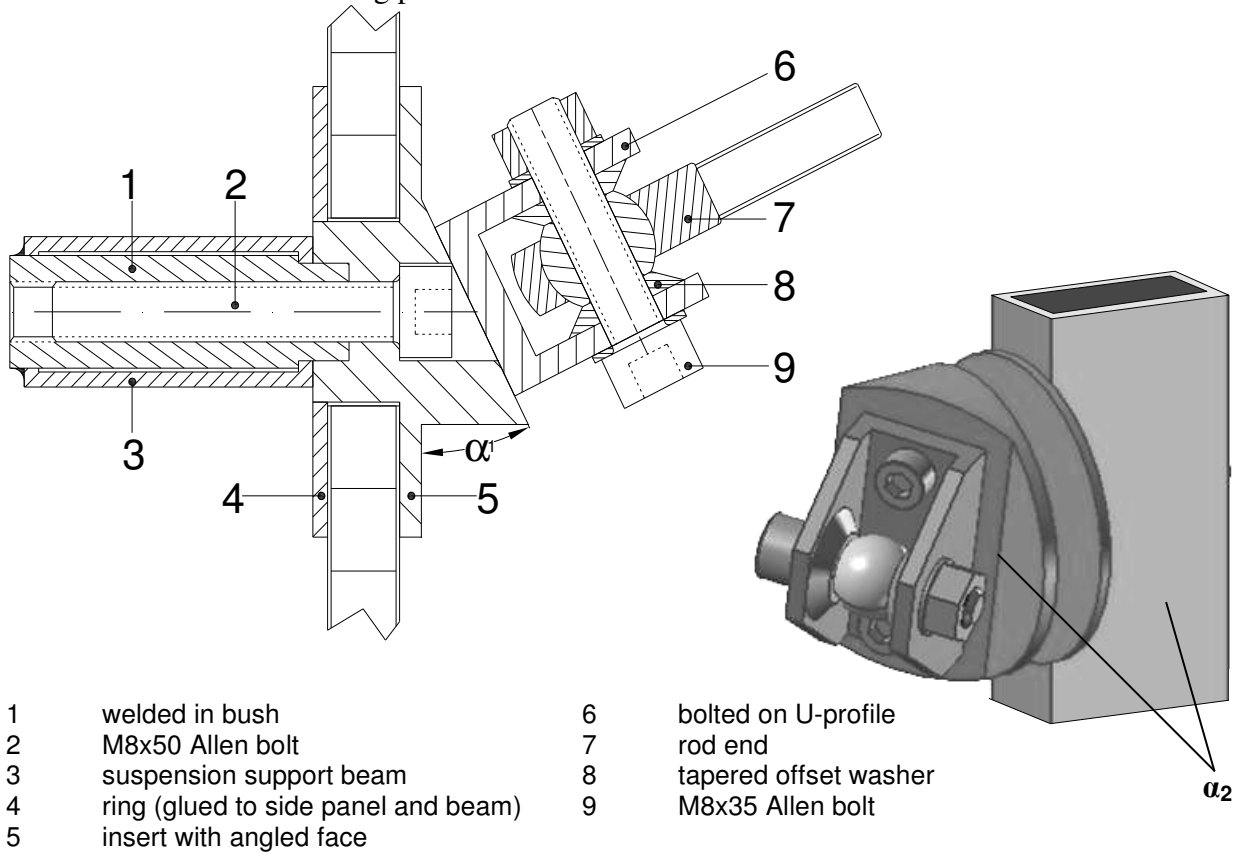
Figure 6.2: "Type 1" mountingpoint

The flat face on the insert is determined by two angles, α_1 and α_2. α_2 Is defined as the angle between the indicated face and edge in figure 6.2. The angle is calculated by Unigraphics, using the suspension centerlines, this can be seen in figure 6.3.
When suspension centerlines are changed Unigraphics automatically updates all angles. The semi finished insert is made eight times on the turning lathe. Then four versions with a different α_1 are milled. Every version is used left and right. Angle α_2 is determined when gluing in the insert.
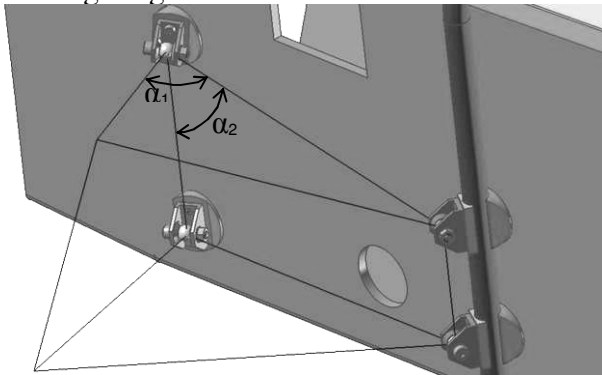
Figure 6.3: Suspension angles

6.2.2 Mounting point "type 2"

Mounting point type 2 is used at the front roll hoop. The inserts mounting the front hoop are placed at the connection rod heights so the suspension forces will be directly distributed into the chassis. To create a flat surface on the round roll hoop tube an aluminium adapter plate is added with a rounded face, fitting on the roll hoop tube radius. Figure 6.4 shows the mounting point on the front roll hoop.
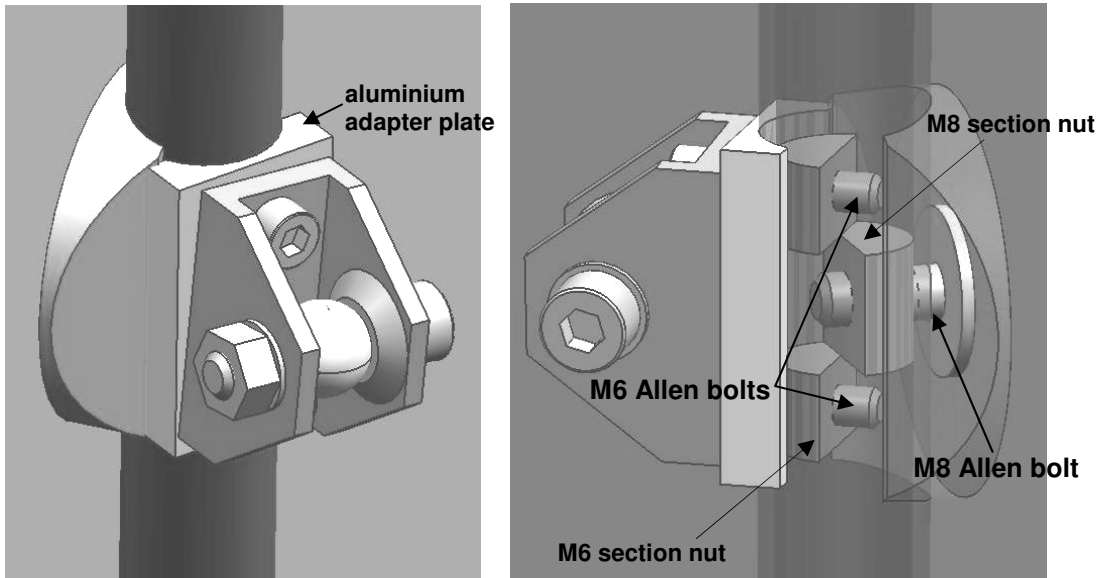
Figure 6.4: Mounting point "type 2"

The roll hoop is tightened from the inside with and M8 Allen bolt using a section nut. The u-profile and the adapter plate are fixed by two M6 Allen bolts that go through the roll hoop into the M6 section nuts. The angle α_2 is obtained by drilling the holes in the U-profile off-centre.

6.3.3 Mounting point "type 3"

Mounting point "type 3"is applied at the rearframe (see figure 6.5). The flat faces are already milled on the rearframe. The U-profiles have their attachment holes drilled off-centre to introduce the α_2 angle.
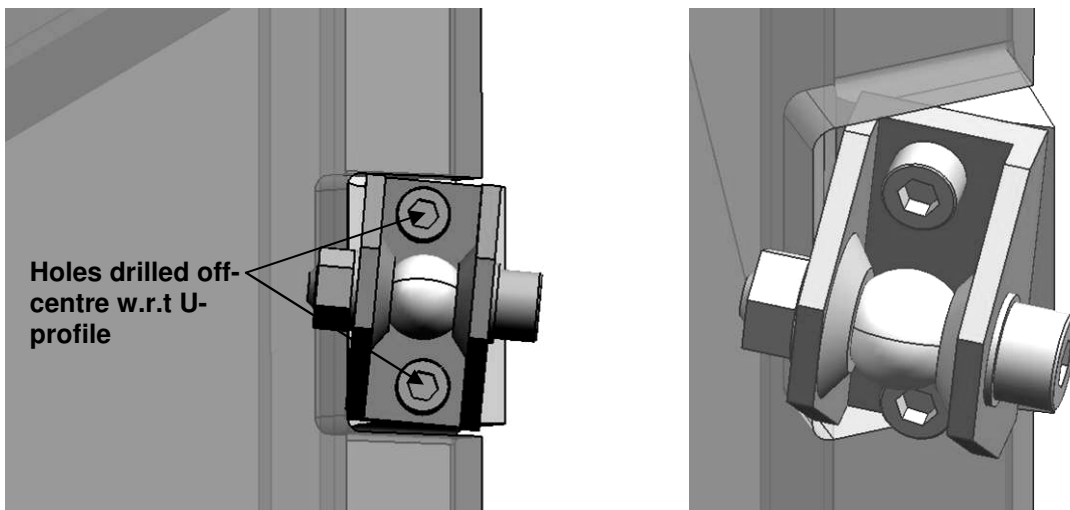
Figure 6.5 Mounting point "type 3"

6.3 Connection rods and uprights

The uprights were mainly designed by formula student team members as were the brake disks and calipers. Therefore these parts are shown but not discussed. First a complete overview of the connection rods and uprights is given in figure 6.6.
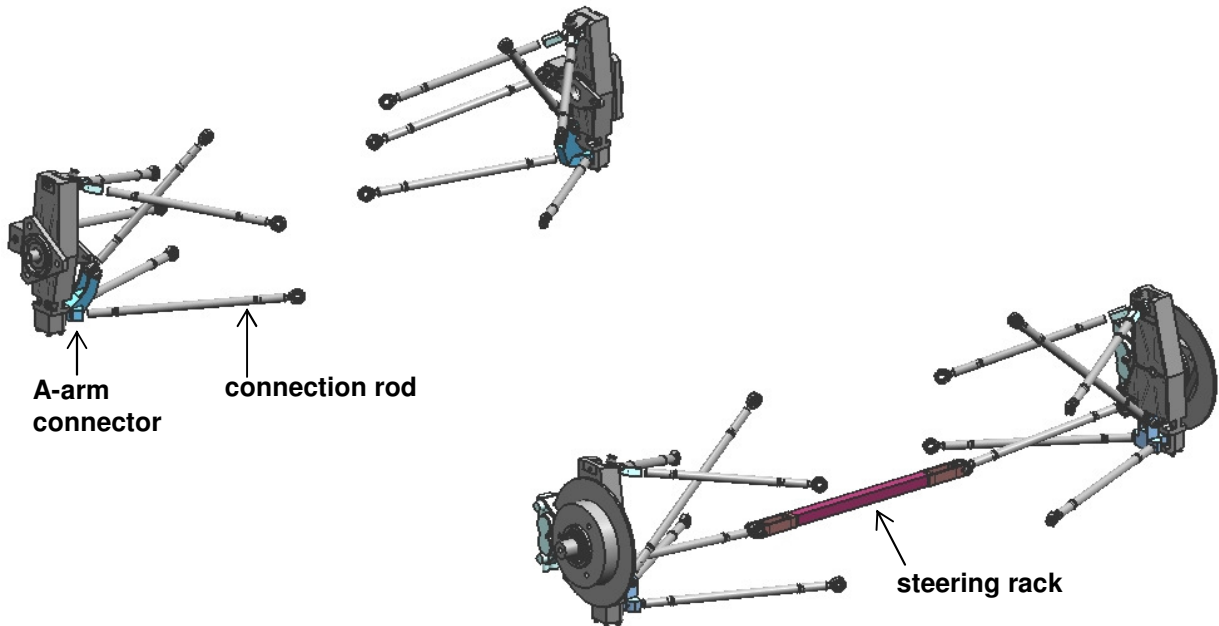
Figure 6.6: Overview of connection rods and uprights

Several parts will be discussed in detail starting with the connection rod. The rod will be made out of an aluminium tube. On both ends a bush is welded, one with left and one with right inner M8 thread. The bush has an 11 mm hole to improve the welding proces, heat is conducted through the thin part of the bush to the thicker part. Also the stress distribution will improve, there will be no stress concentration around the weld.
On the chassis side the rod end is screwed in, secured by a nut. The upright rod side is connected to the A-arm connector by a stud. A cross section of the connection rod is depicted in figure 6.7.

1	alumiunium tube Ø16 x 2	4	rod end GAKR8-PW (INA)
2	bush with M8 thread	5	A-arm connector
3	left thread stud	6	securing nut
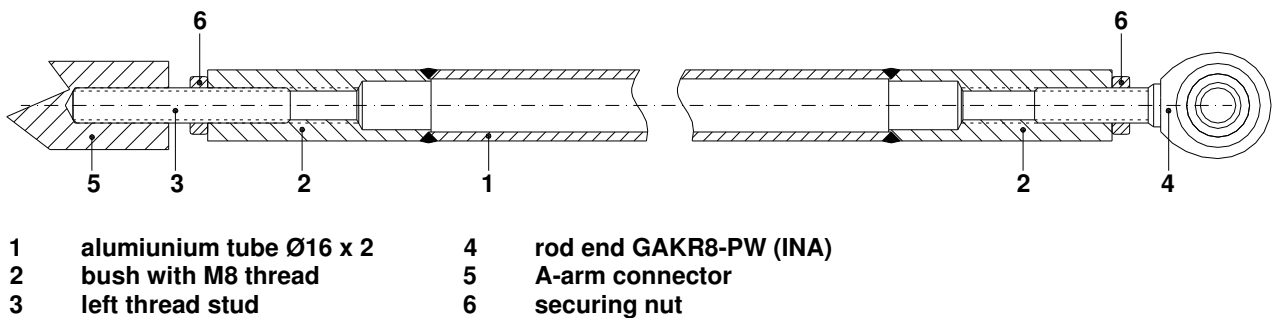
Figure 6.7: Connection rod cross section

The connection rods can be marked with an arrow pointing out and a letter code for the position. Markings must be made in the thicker end part.
Detailed information on the rod ends is given in appendix H.

The rear A-arm connector is a rather complex part. It has to join the lower A-arm connection rods but also the pushrod is mounted on this part. Figure 6.8 shows a zoomed view of the rear right upright. All the rod centerlines have to converge to the lower upright pivoting point.

But the flexplate has a large diameter and conflicts with the pushrod centerline. Therefore the A-arm connector needs a cut away and the pushrod force makes a small detour.
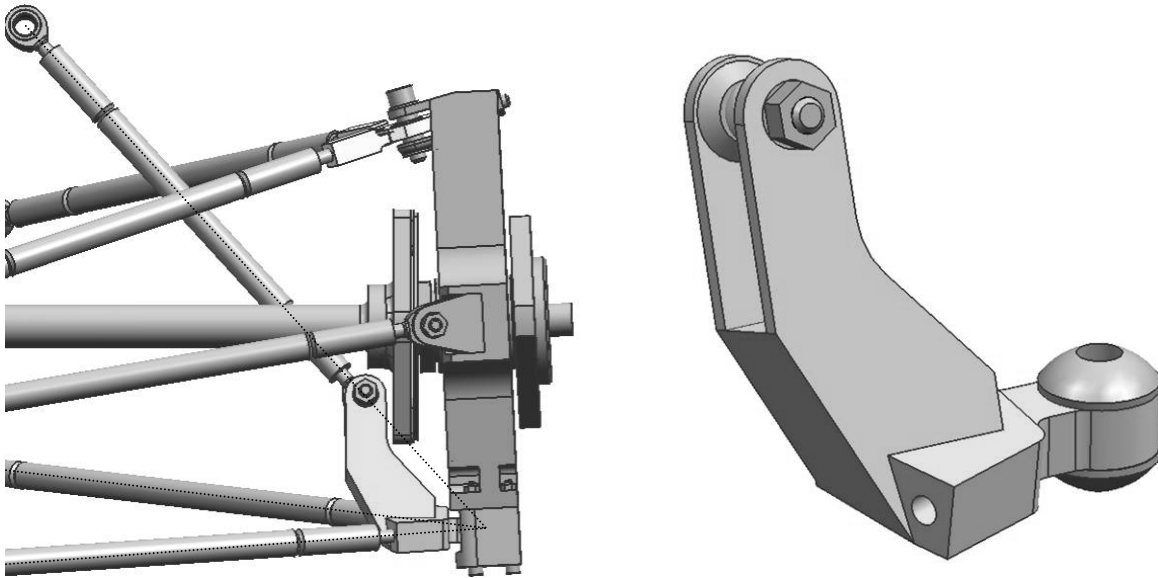
Figure 6.8: Flexplate intersects with the pushrod centerline, special A-arm connecter design

Furthermore the steering rack width is enlarged to prevent bump steer. This is done by bolting on a steering rack extension. Figure 6.9 shows the aluminium extension.
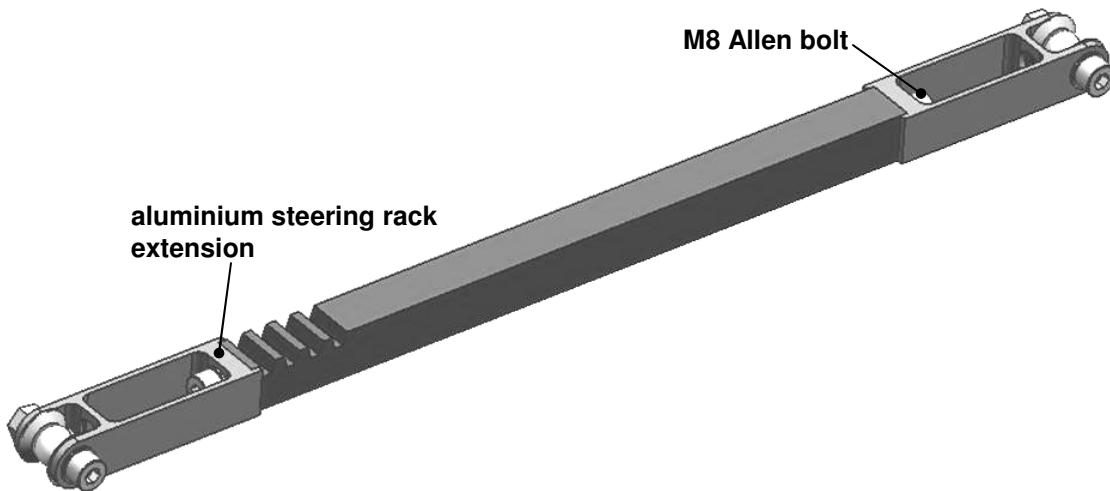
Figure 6.9: Steering rack with extension

6.4 Suspension unit concepts

The FSRTE02 is equipped with pushrods. These pushrods will be attached to a rocker. The rocker will pivot as the wheel travels. This is shown schematically in figure 6.10.
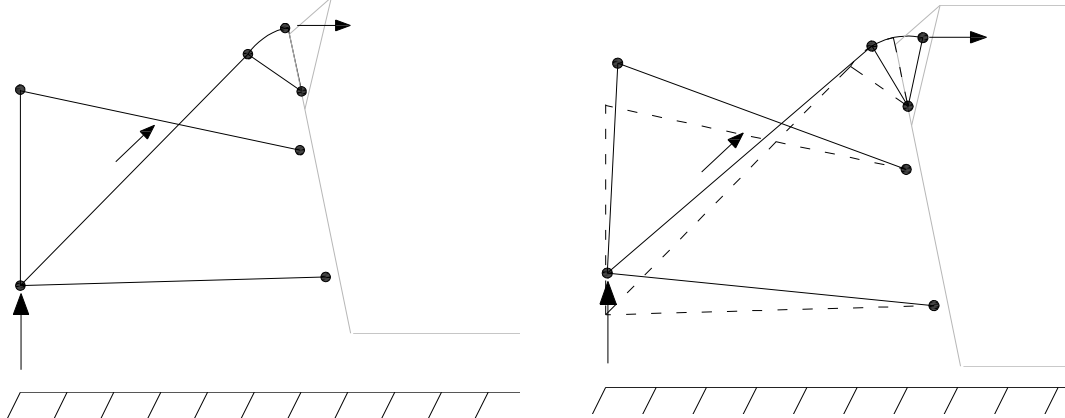
Figure 6.10: Schematic presentation of rocker in both utmost positions

Two situations are distinguished, pure bump and pure roll. Both corresponding stiffness' were calculated in paragraph 4.1 and 4.2.2. A suspension system in which both can be adjusted independently is therefore preferred.
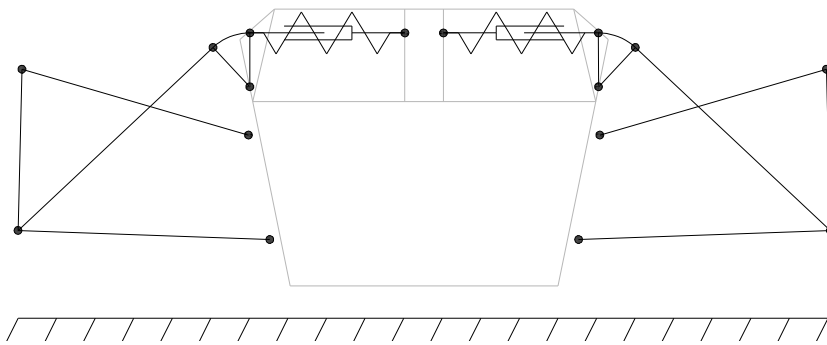
Figure 6.11: Most common used system with two shocks

The most commonly used system is depicted in figure 6.11. This system has both bump and roll stiffness and adjustments can not be made independently. If one installs shocks with a higher stiffness, the roll stiffness also increases.

By using a single shock or monoshock instead of two, the system can be made independent. This is depicted in figure 6.12.
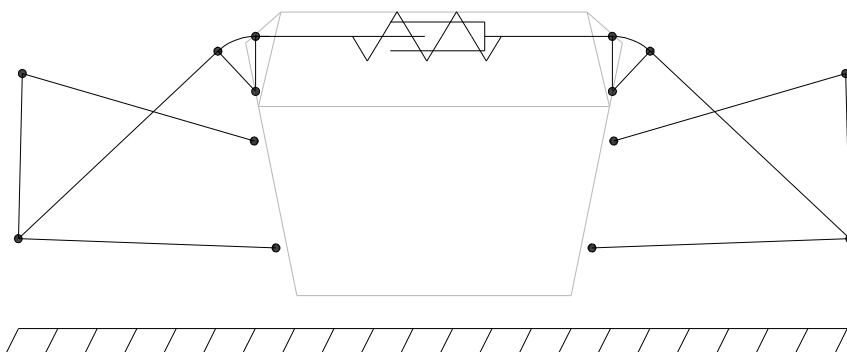
Figure 6.12: Monoshock system

Another advantage is that the monoshock will be lighter than two single shocks. Roll stiffness can be added in different ways. A simple solution is a classic anti-roll bar. But there is little space at the upright to connect an anti-roll bar. The uprights are coupled to the rockers through the pushrods, therefore the rocker rotation will be used for the anti-roll system. Bump and roll can be identified using both rocker rotation directions. Figure 6.13a shows the rocker rotation for pure bump and figure 6.13b shows the rotation direction for pure roll.
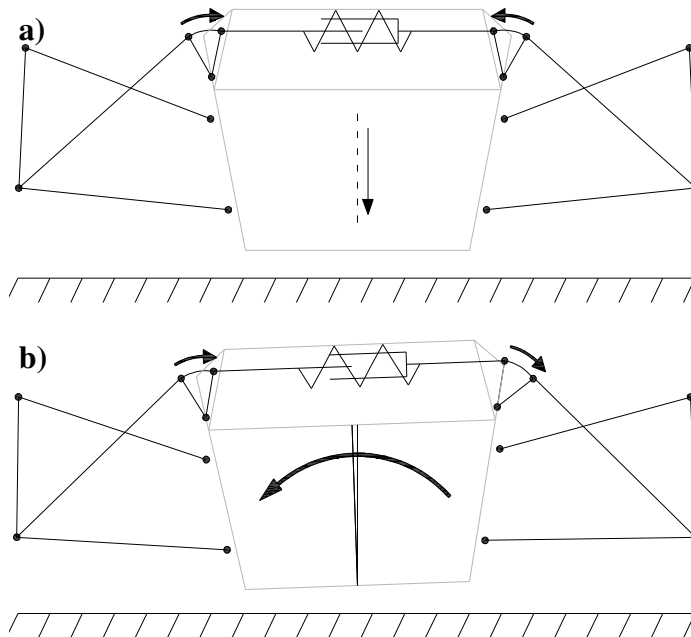
Figure 6.13   a: Rocker rotation in pure bump   b: Rocker rotation in pure roll

In the following paragraphs different concepts for the rocker activated anti-roll system are discussed, starting with the original FSRTE01 design.

6.4.1 Original FSRTE01 design

The original design of the FSRTE01 is made by Wouter Berkhout. Figure 6.14 shows this design
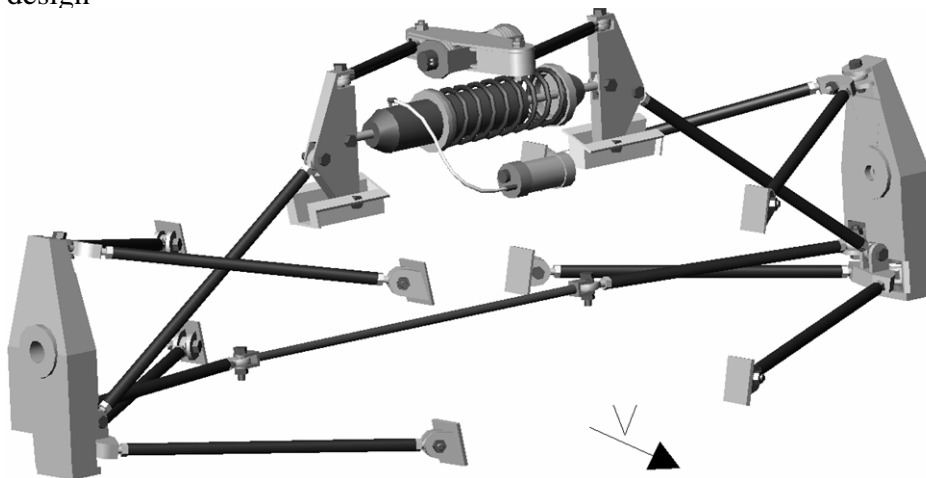
Figure 6.14: Original FSRTE01 anti-roll system design

Figure 6.15a shows a top view of the FSRTE01 anti-roll system in a pure bump situation. Both rods move in opposite direction and the third rocker will rotate about point C. Figure 6.15b shows a top view of the FSRTE01anti-roll system in a pure roll situation. Both rods move in the same direction and the third rocker will translate in y-direction and compress the Belleville spring washers. By changing the spring washer configuration the roll stiffness can changed.
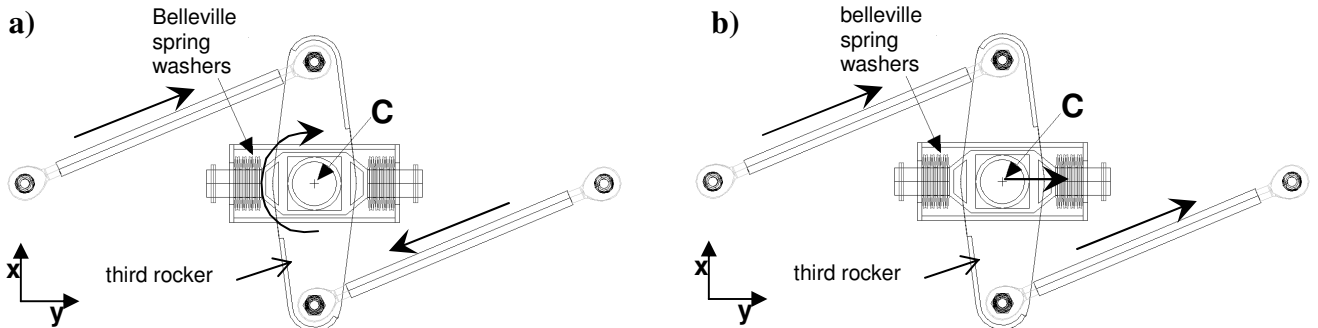
Figure 6.15   a: FSRTE01 anti-roll system in pure bump   b: FSRTE01 anti-roll system in pure roll

In case of roll both rods are applying a force onto the third rocker. The y-components of these forces are supported by the Belleville spring washers. The x-component is supported by the guidance rail, causing friction.
The roll damping is provided by the friction between the Belleville spring washers, but can not be adjusted independently.
The forces acting on the rockers in case of roll have an x-component which causes the rockers to tumble in x direction.
Therefore other concepts have been looked at, in order to find an optimized system. Some of them are based on the FSRTE01 principle, others are completely different.

6.4.2. Anti-roll concept 1

This paragraph actually shows two variations on one anti-roll concept based on pneumatic and hydraulic. First the pneumatic version is discussed. Figure 6.16 shows this concept. The system uses three concentric tubes. The inner tube (1) is connected to the right rocker and has a piston on the other end. The second and middle tube (2) is connected to the left rocker and acts like a cylinder. In a pure bump situation both tube move in opposite direction over a distance x, compressing the large helical spring. Meanwhile gas (air or nitrogen) is pumped out through radial holes in the cylinder wall with a volume of A_1*2*x. The outer tube (3) is a cylinder too in which the middle tube (2) acts like a piston. The middle tube (2) is moving to the right over a distance x, area A_2 is chosen $2*A_1$ so the pumped in volume will cause the outer tube (3) to move over a distance $A_1*2*x / 2*A_1= x$ in respect to the middle tube (2). So in the end, the outer tube (3) will not move in a bump situation. In a pure roll situation no gas is pumped and the outer tube (3) is connected to the tube 1 and 2 with the gas stiffness.
The outer tube (3) is fixed on the chassis so the roll-stiffness is based on compressing the gas. It can be adjusted by changing the gas volume.
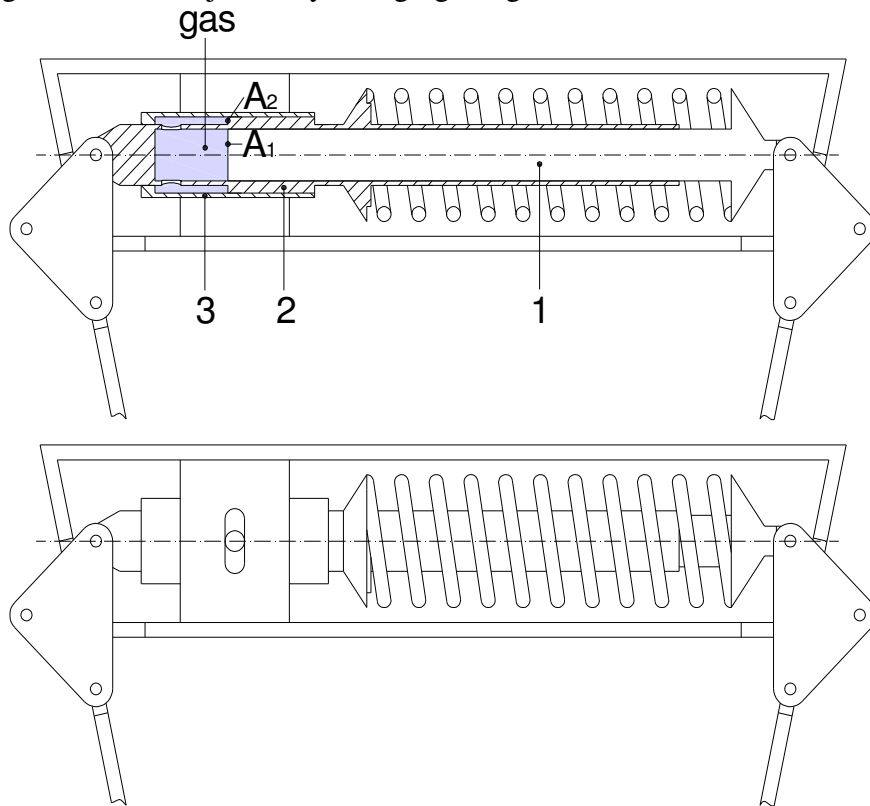
Figure 6.16: Pneumatic anti-roll concept

The pneumatic anti-roll concept is based on the same principle only the gas is replaced by oil. This makes it possible to use the anti-roll system also for bump damping.
The oil stiffness is much too high to be used as the anti-roll stiffness. Therefore a relative low stiffness is added between the outer tube (3) and the chassis. Roll damping should also be added to this concept.
This concept needs a lot of development especially on the sealing of the parts.

6.4.3. Anti-roll concept 2

Figure 6.17 shows a schematic topview of the second anti-roll concept.
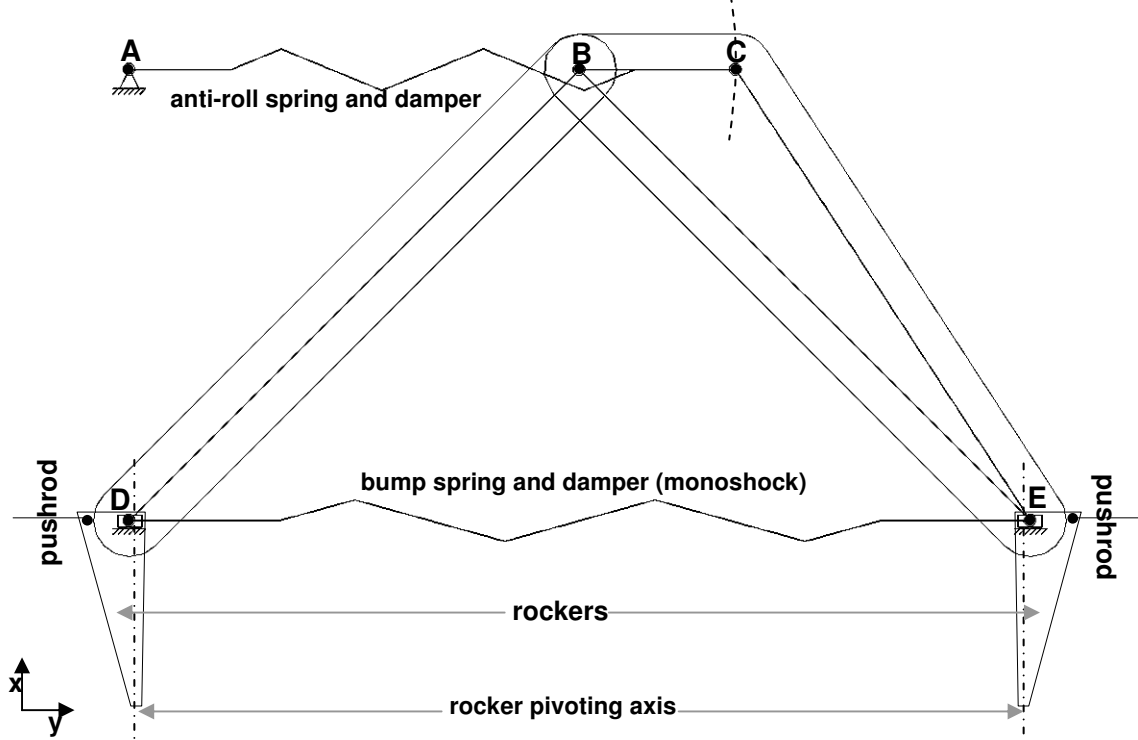
Figure 6.17: Schematic topview of anti-roll concept 2

Two beams are pointing forward and have a pivoting point B. In a pure bump situation point D and E move towards each other causing point B to move in a straight line in forward direction. Point C will now describe an approximate radius about point A. This is examined using SAM. The result is plotted in figure 6.18
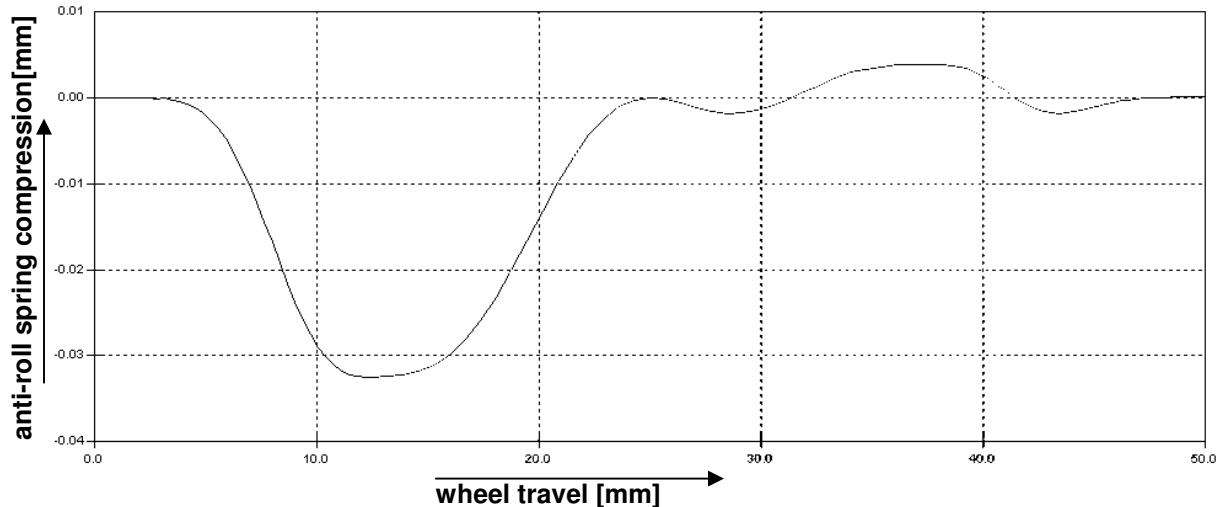
Figure 6.18: Anti-roll spring compression in pure bump for concept 2

The anti-roll spring compression in pure bump is 0.033 mm max and is therefore assumed to have no influence on the bump stiffness.

In a pure roll situation points D and E translate in the y-direction over an equal distance. This means point B and C will also travel this distance in y-direction and the anti-roll spring is actuated.
In reality points D and E will travel in z-direction too and spherical joints are needed in all points. Furthermore this concept takes up a lot of chassis space.

6.4.4. Anti-roll concept 3

This concept is based on the original FSRTE01 design except that the third rocker is now rotating about a horizontal axis. To keep it compact the third rocker is designed around the monoshock. A schematic frontview of this concept is given in figure 6.19.
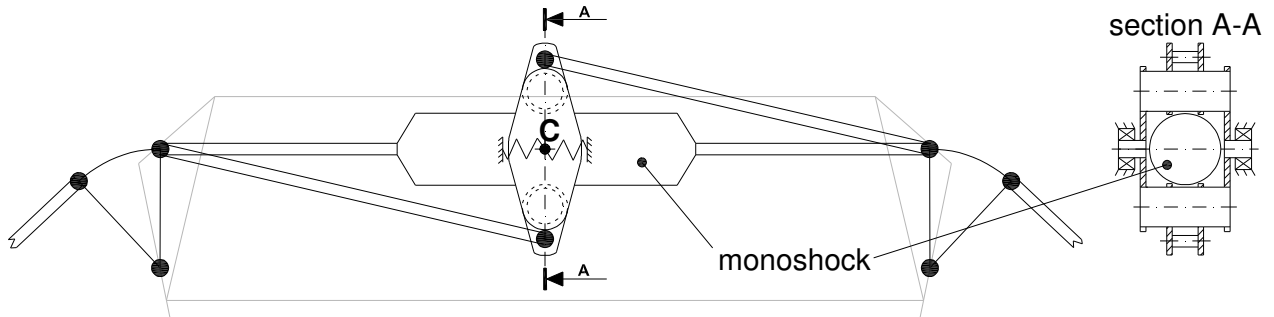
Figure 6.19: Anti-roll concept 3 in frontview

This is 2D system and all pivoting axes are parallel this means all forces are in one plane.

With the third rocker placed vertical, the system is not working symmetrically. To examine this effect a SAM model is made. Three situation are depicted in figure 6.20, together with the displacement of point C in y-direction

hard bump on both wheels,
maximum spring compression
y-displacement point C = +0.41 mm

ride height static
spring compression
y-displacement point C = 0 mm

wheels off the ground,
spring unloaded
y-displacement point C = +0.42 mm
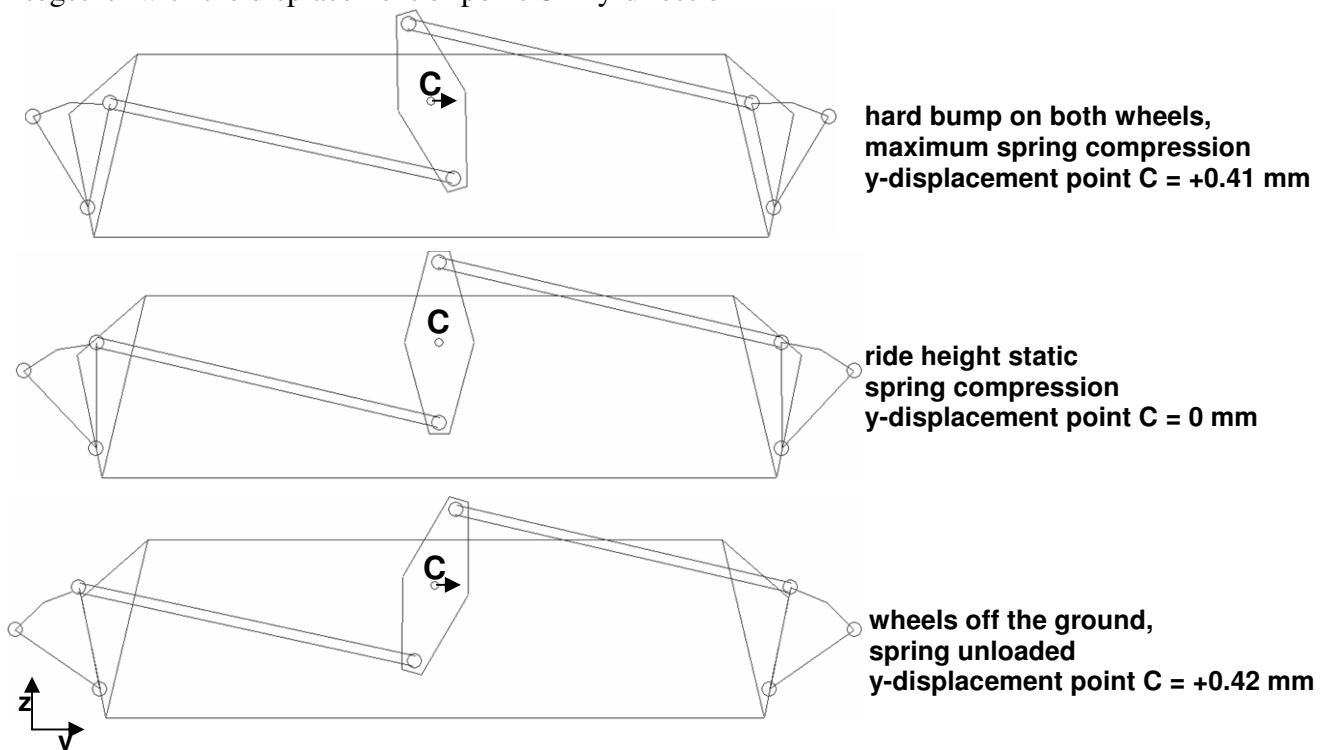
Figure 6.20: SAM model results anti-roll concept 3

So the maximum y-displacement is approximately 0.4 mm in extreme bump situation. This is acceptable so the asymmetric effect is neglected. The stiffness in y-direction of point has not been worked out so that is a point of attention. Furthermore the rocker connection points have to be detailed.

6.4.5. Anti-roll concept 4

This concept looks like the original FSRTE01 design. The main difference is that the translating carriage is replaced by a rotating arm. The third rocker rotation point will now describe a circular path instead of a linear path in a roll situation. This will solve the friction problem of the FSRTE01 design. The rockers are not loaded in x direction. Furthermore the monoshock is placed in front of the anti-roll system. A topview of this concept is given in figure 6.21.
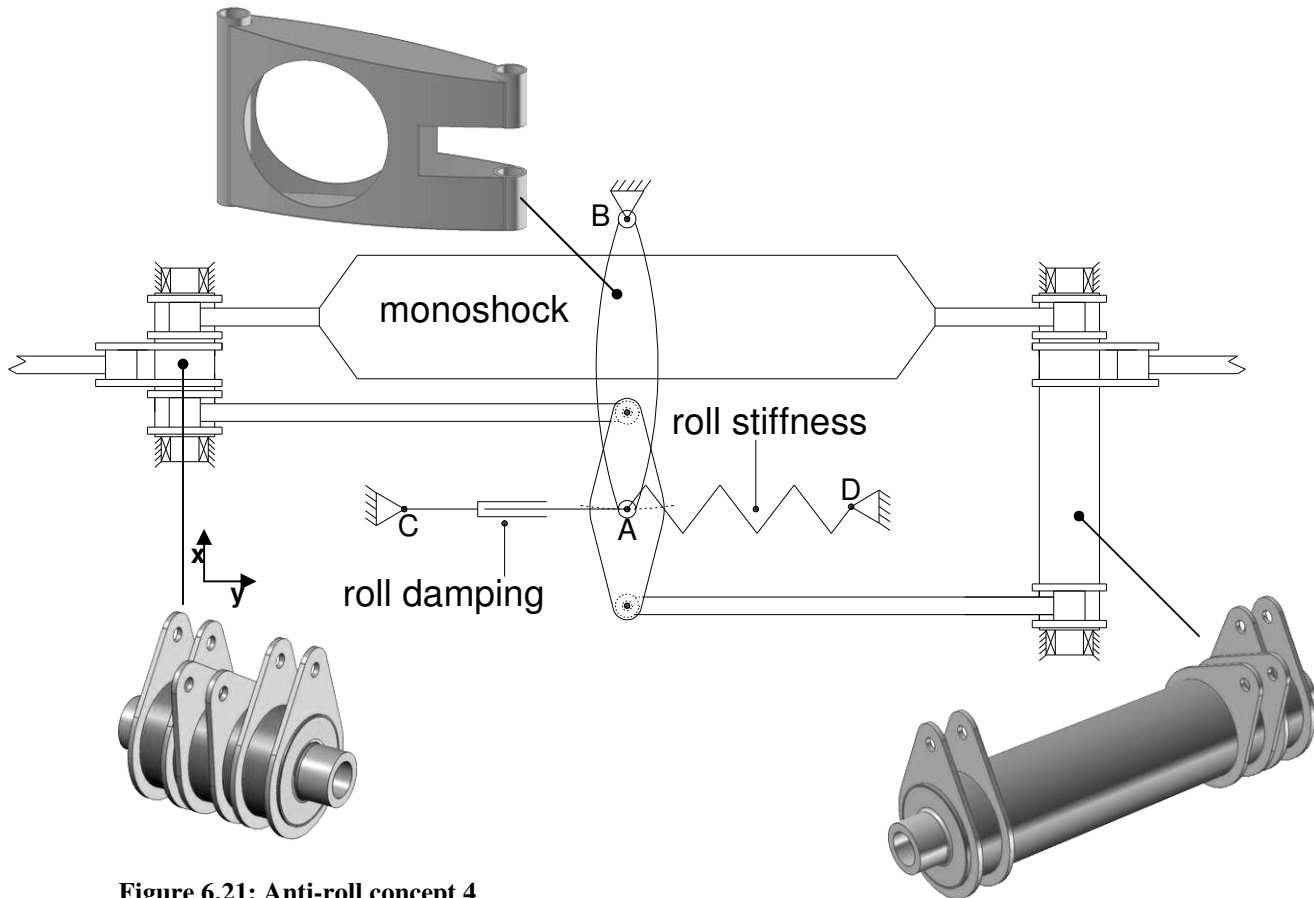
Figure 6.21: Anti-roll concept 4

The rockers are made from a tube to transmit the torque. Welded on plates apply the torque onto the tube. The stroke of point A is 25-30 mm in both directions depending on the rocker ratio. Using an arm A-B of 200 mm this means the x-displacement of point A will be 3.1-4.5 mm. This can be solved using revolute joints in points C and D.
The roll stiffness can be introduced using a helical spring. The roll-damping can be applied using a motorcycle steering damper. Arm A-B intersects with the monoshock, this is solved using a box shaped arm with a large hole for the monoshock
This system will take a lot of space in the chassis, therefore another concept is made.

6.4.6. Anti-roll concept 5

This concept uses a standard aluminum rectangular tube to mount in all suspension parts. The idea is to build up and test a suspension box on the bench and place the whole assembly in the car.

This way all accurate bearing alignments can be CNC machined on the aluminum tube. The largest available aluminum tube of 120x80x2.5 is chosen. A monoshock with a maximum outside diameter of 71 mm fits into this tube leaving 1.5 mm clearance with the wall. In concept 4 the monoshock was placed in front of the anti-roll system.

In this system the monoshock is placed beneath the anti-roll system. For the linear guidance of the third rocker pivoting point, a standard INA ball monorail guidance system is used. Figure 6.22 shows a cross section of concept 5 in front view and a topview.
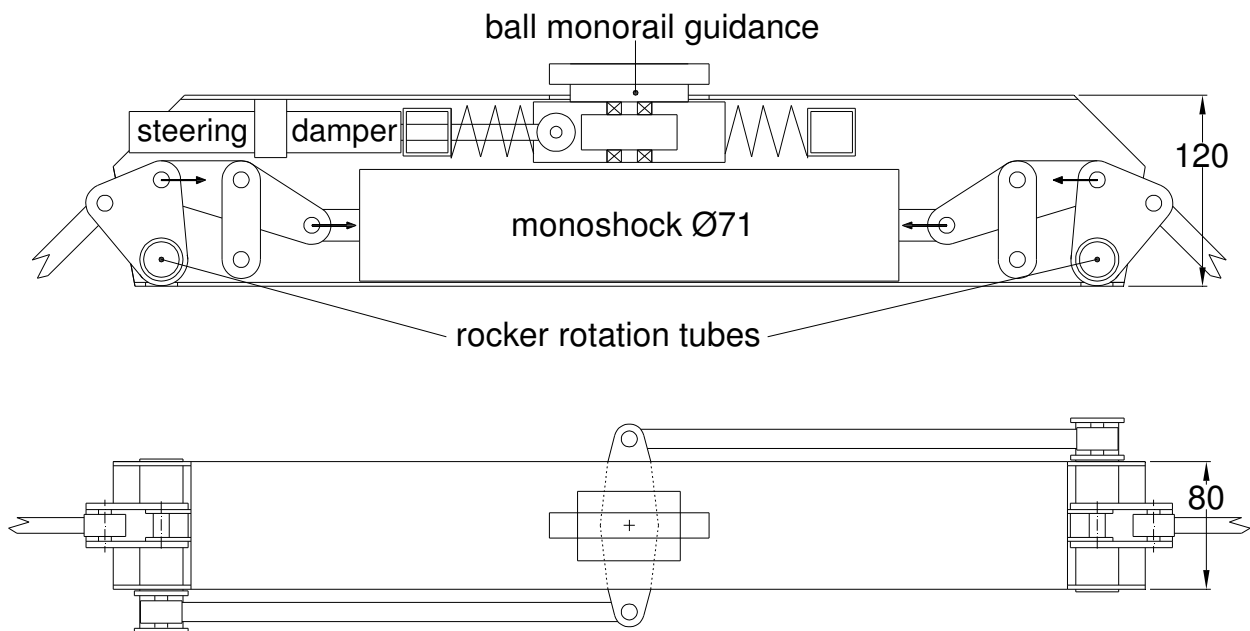
Figure 6.22: Topview of anti-roll concept 5

This concept uses two parallelograms to be able to place the monoshock as low as possible in the rectangular tube. The ball monorail guidance system reaches through a hole in the top most face of the tube. On the ball monorail guidance system a block is bolted which is used to mount the bearings for the third rocker rotation and to attach the steering damper. The block is preloaded by two helical springs. The third rocker reaches through two holes in the tube side faces. Outside the tube the third rocker is connected to two rods using rod ends. The rods are also connected to a lever arm mounted onto the rocker rotation tubes reaching through rectangular holes in the aluminum tube sidewalls. This anti-roll system can be used front and rear. Furthermore the roll stiffness can be adjusted by changing the lever arm length. The stiffness changes with the squared ratio. An adjustable steering damper is used to adjust the roll damping.

6.5 Suspension unit design

Concept 5 will be used for the FSRTE02 suspension and will henceforth be called suspension box. It has a lot of similarities with the FSTRE01 mechanism but it solves the problems of friction, tumbling of the rockers and roll damping. Furthermore concept 5 is the most compact one, it is the easiest to mount on the chassis and it can be applied front and rear. It can also be bench tested prior to installation.

In this paragraph calculations will be made for the suspension ratios, the corresponding monoshock specifications and the anti-roll springs and damper.

Finally the assembly is build up step by step.

6.5.1 Suspension ratios

The front and rear suspension box placement is shown in sideview in figure 6.23.
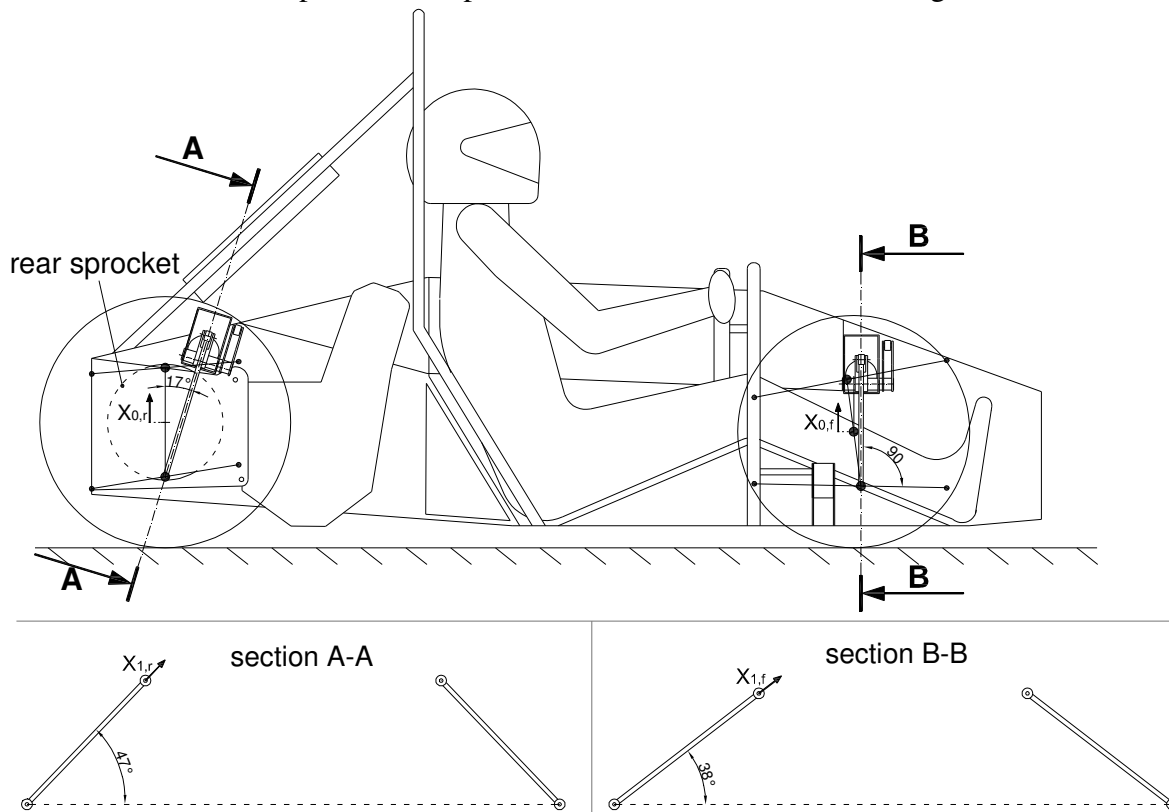
Figure 6.23: Sideview of suspension box placement and pushrod plane sections

The rear pushrod is leaning 17° forward in sideview. The rear suspension box is aligned with the pushrod. The largest rear sprocket of 260 mm and the engine determined the position of the suspension box.

The torsion tubes have to extend forward as far as possible for high chassis torsion stiffness. Therefore the front suspension box is placed horizontal in sideview. This means the front pushrod is placed vertical in sideview.

Figure 6.23 also shows sections A-A and B-B through the rear and front pushrod planes and the inclined angles of 47° and 38° rear and front.

Different ratios are calculated starting with the pushrod ratio "i_p". This is defined and calculated using the displacements X_0 and X_1 and angles from figure 6.23:

$$i_{p,r} = \frac{X_{1,r}}{X_{0,r}} = \cos(17^o) \cdot \sin(47^o) = 0.7$$

$$i_{p,f} = \frac{X_{1,f}}{X_{0,f}} = \cos(0^o) \cdot \sin(38^o) = 0.62$$

The next ratio is the monoshock ratio "i_m". This ratio is defined as the monoshock travel divided by the pushrod travel in pure bump.
Therefore the rocker and the parallelogram are depicted in figure 6.24:
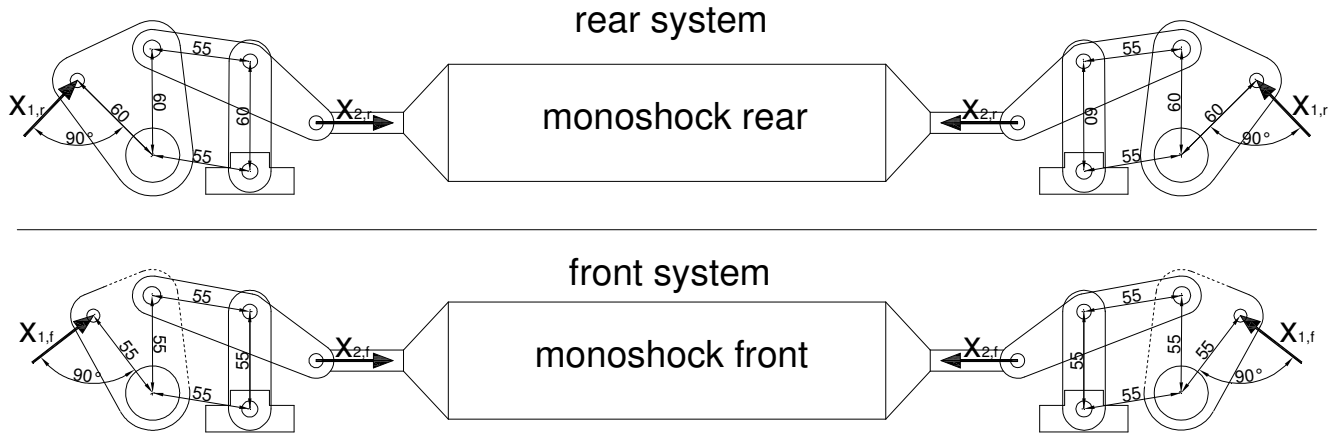
Figure 6.24: Rocker and parallelogram dimensions of front and rear suspension box

On the front system all bar lengths are 55 mm this means $X_{1-f} = X_{2-f}$.
On the rear system all bar lengths are 60 mm this means $X_{1-r} = X_{2-r}$
In pure bump both pushrods travel an equal distance X_1, this means that the monoshock is compressed from both sides by a total distance of $2*X_2$.
Therefore the monoshock ratios $i_{m,r}$ and $i_{m,f}$ are **2** for the rear and front suspension respectively.

Finally the anti-roll ratios $i_{a,r}$ and $i_{a,f}$ are determined; this ratio is defined as the ball monorail guidance system displacement divided by the pushrod travel.
Therefore the length of the lever arm mounted onto the rocker rotation tubes outside the rectangular tube is needed. This is depicted in figure 6.25.
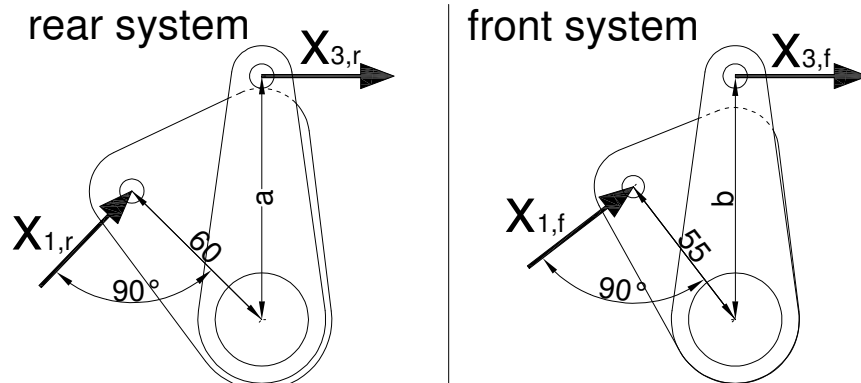
Figure 6.25: Rocker and lever arm dimensions of front and rear suspension box

Different ratios can chosen by changing the lever arm length. Then the anti-roll ratios front and rear are:

$$i_{a,r} = \frac{X_{3,r}}{X_{1,r}} = \frac{a}{60}$$

$$i_{a,f} = \frac{X_{3,f}}{X_{1,f}} = \frac{b}{55}$$

6.5.2 Anti-roll helical spring stiffness

The preferred roll stiffness C_{roll}=22000 Nm/rad front and rear and the permitted roll angle is 1.7 deg. The roll stiffness can also be expressed in a linear stiffness on the wheels by equation 6.1:

$$C_{roll,wheel} = \frac{C_{roll}}{\left(\frac{1}{2}t\right)^2} \qquad\qquad \text{(equation 6.1)}$$

With t, the track width. This results in a $C_{roll,wheel,r}$ of 61100 N/m and a $C_{roll,wheel,f}$ of 56300 N/m. By multiplying this value with the pushrod ratio and the anti-roll ratio, the preferred anti-roll spring stiffness can be determined. But a reverse approach is used here. First the anti-roll spring stiffness is determined, then the preferred anti-roll ratio is calculated, and the anti-roll lever arm length is calculated. Figure 6.26 shows the helical spring used front and rear, table 6.1 shows the corresponding spring properties.
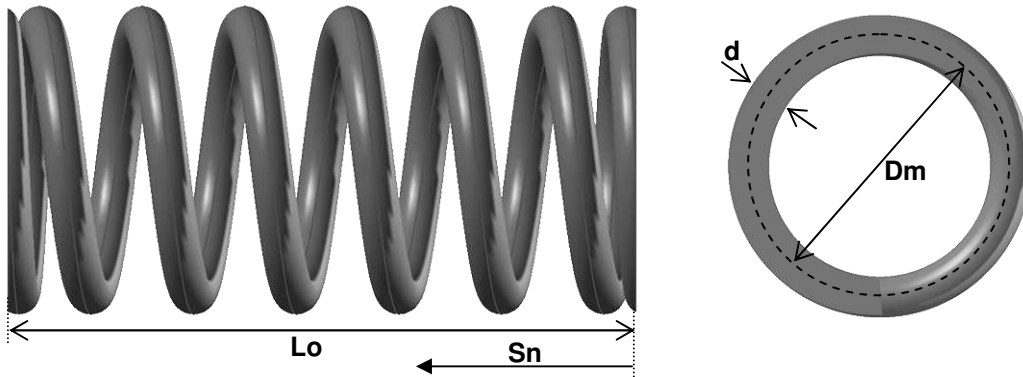
Figure 6.26: Tevema helical spring for the anti-roll mechanism

Wire diameter	d [mm]	5
Mean diameter	Dm [mm]	32
Number of active coils	Nw [-]	5.5
Unloaded spring length	Lo [mm]	75
Spring stiffness	C_{tevema} [N/mm]	35.3
Maximum spring compression	Sn [mm]	34.8
Force at maximum compression	Fn [N]	1226
Order number at Tevema		D 13840

Table 6.1: Tevema helical spring for the anti-roll mechanism dimensions and specifications

The spring is used twice to preload the third rocker block, this is shown in figure 6.27
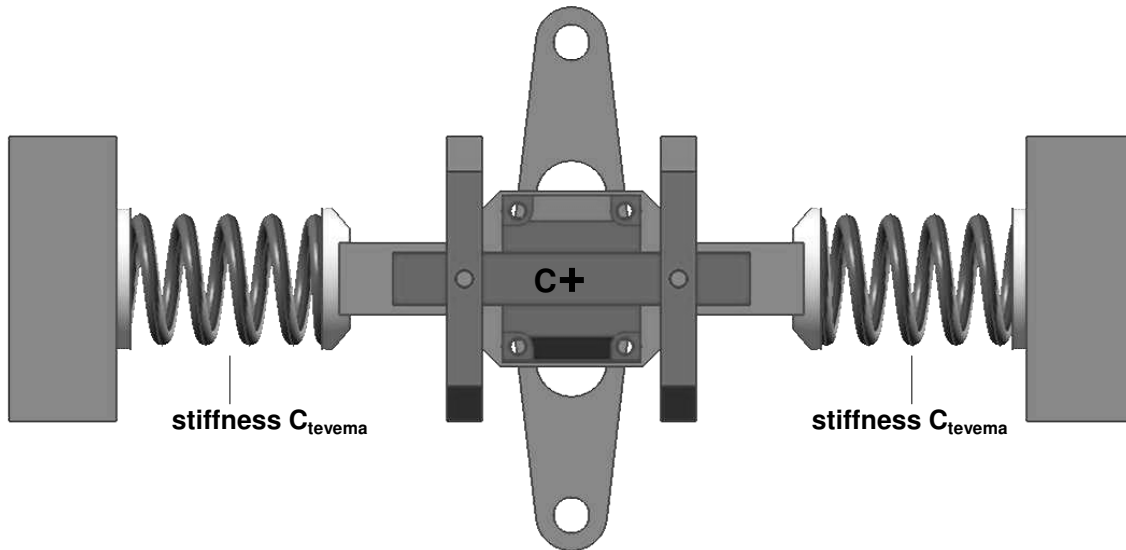
Figure 6.27: Third rocker block preloaded by two helical compression springs

So the stiffness in point C in horizontal direction equals 2*C_{tevema}=70.6 N/mm. Both springs are preloaded over a distance of 17.4 mm, this is half of the maximum allowable spring compression. The linear stiffness on the wheels caused by the anti-roll system is given by equation 6.2.

$$C_{roll,wheel} = i_p^2 \cdot i_a^2 \cdot 2 \cdot C_{tevema} \qquad \text{(equation 6.2)}$$

C_{tevema}, $C_{roll,wheel}$ and the ratio i_p are already known. $i_{a,r}$ and $i_{a,f}$ are 1.33 and 1.44 respectively. The corresponding anti-roll lever lengths a and b in millimeters, are calculated below:

$$a = i_{a,r} \cdot 60 = 1.33 \cdot 60 = 79.7$$
$$b = i_{a,f} \cdot 55 = 1.44 \cdot 55 = 79.2$$

The roll stiffness front to rear ratio is very important for the road holding this can be used to adjust over- or under steering properties. Therefore the roll stiffness should be adjustable this is done by picking another connection hole on the lever arm changing lengths a and b. The adjustment area is schematically shown in figure 6.28, furthermore table 6.2 shows all corresponding roll stiffness and lever arm lengths a and b.
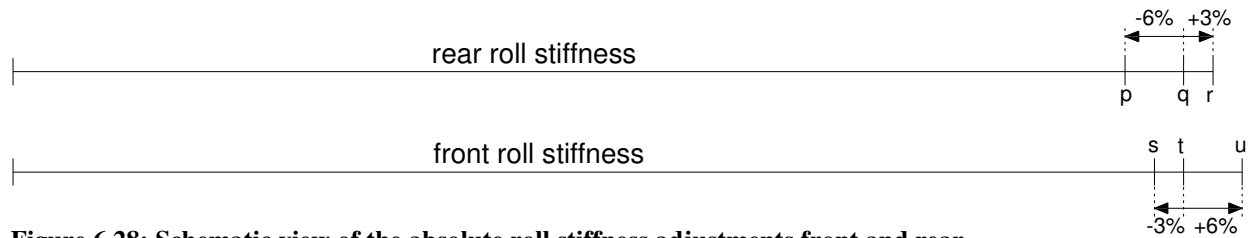
Figure 6.28: Schematic view of the absolute roll stiffness adjustments front and rear

Adjustment	Roll stiffness [Nm/rad]	Lever arm length [mm]
p	20680	77.3
q	22000	79.7
r	22660	80.9
s	21340	78
t	22000	79.2
u	23320	81.6

Table 6.2: Adjustments range for front and rear anti-roll stiffness and corresponding lever arm lengths

Table 6.3 shows all possible roll stiffness ratios.

$C_{roll,r}$ [Nm/rad]	$C_{roll,f}$ [Nm/rad]	Ratio $C_{roll,r}/C_{roll,f}$
20680	21340	0.97
20680	22000	0.94
20680	23320	0.87
22000	21340	1.03
22000	22000	1
22000	23320	0.94
22660	21340	1.06
22660	22000	1.03
22660	23320	0.97

Table 6.3: Possible rear to front roll stiffness ratios

The front and rear levers can even be swapped, to double the number of possible front to rear ratios.

6.5.3 Steering damper specifications

The used steering damper is shown in figure 6.29. The damper is designed and produced by WP.
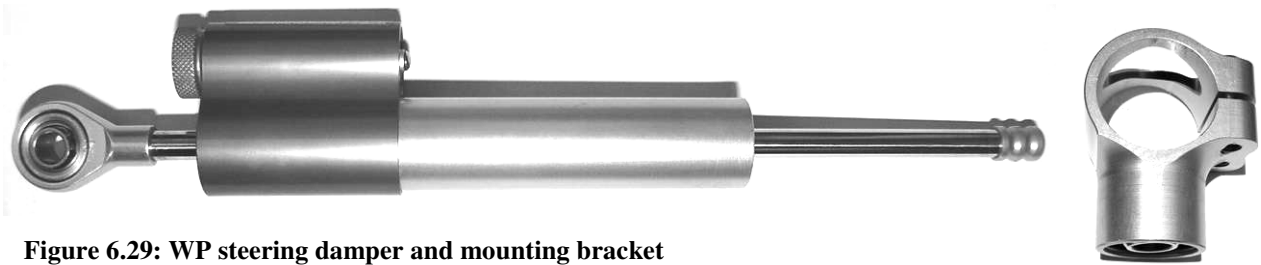
Figure 6.29: WP steering damper and mounting bracket

The steering damper has two concentric tubes. A piston is mounted onto the central rod. If the piston travels oil is pumped from the inner tube to the space between the inner and outer tube back to the inner tube on the other side of the piston. This way the damping value is independent of the piston movement direction.
The oil is led along a resistance. This can be adjusted by a screw which uses 31 indication clicks.
Damping properties are inquired at WP. Figure 6.30.a shows a measurement of damping force on different speeds using a sinusoid speed signal. The measurement is done without changing the oil resistance.
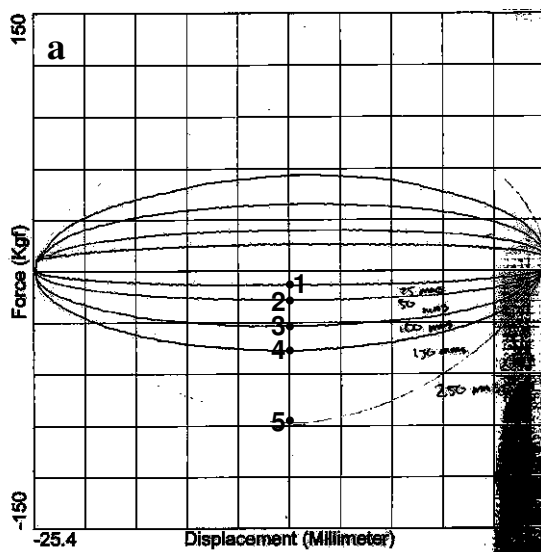
Figure 6.30.   a: WP measurement data   b: Speed-force graph extracted from WP data
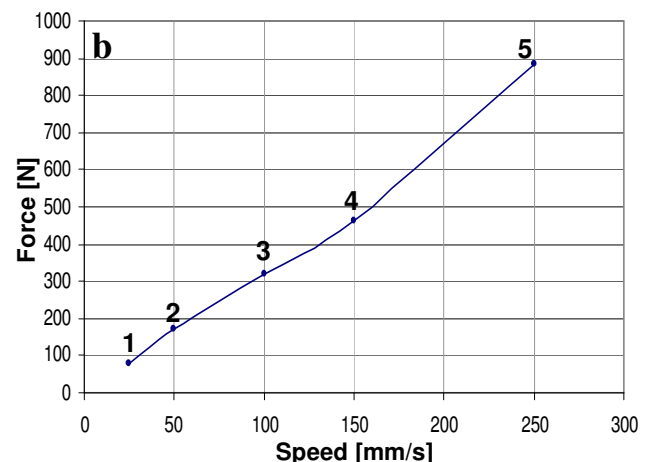
This graph is used to examine the damping properties. Therefore five data points are picked, at which the current speed is plotted against the corresponding force in N.
The resulting graph is depicted in figure 6.30b. It is assumed to be a straight line so the damping is proportional. This means the damping value and the speed are independent.
To find the relation between the resistance screw adjustment and the damping value a test setup is build. The steering damper is placed vertical and a constant force is applied by a mass of 12 kg. A digital camera is used to register the piston movement. Furthermore a measuring tape is added to the test setup. The speed is determined by comparing the distance traveled between two frames and the time between those frames. A schematic drawing is shown in figure 6.31.
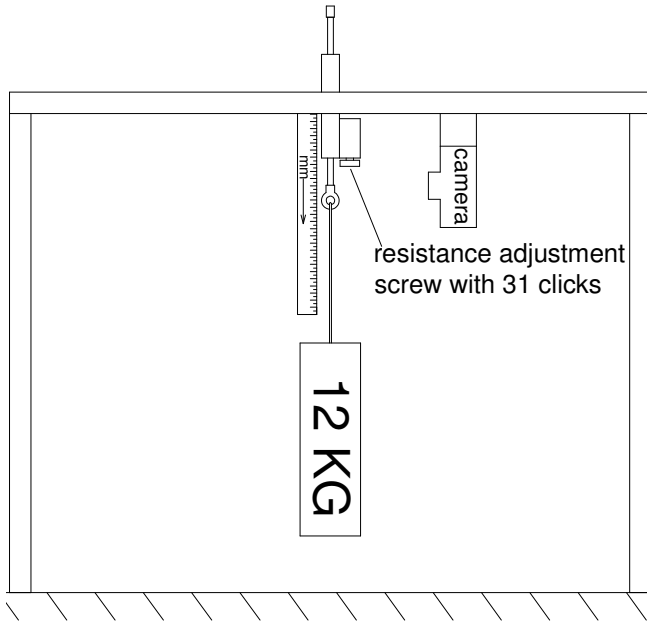
Figure 6.31: Setup to determine WP damping coefficient

The graphs are shown in appendix L, a line is fitted through the measurement data extracting equation 6.3. This equation can be used to calculate the damping coefficient d_{wp} for a certain number of resistance screw open clicks x.

$$d_{wp} = 61 \cdot e^{0.19 \cdot x} \qquad \text{(equation 6.3)}$$

The preferred roll damping was calculated in paragraph 4.2.2; $d_{roll,f} = d_{roll,r} = $ **315 Nms/rad.** This is translated to a linear damping at a single wheel by equation 6.4:

$$d_{roll,wheel,f,r} = \frac{d_{roll,f,r}}{\left(\frac{1}{2} t_{f,r}\right)^2} \qquad \text{(equation 6.4)}$$

The $d_{roll,wheel,f}$ = **805 Ns/m** and $d_{roll,wheel,r}$ = **875 Ns/m**. Now the preferred d_{wp} can be calculated depending using the pushrod and anti-roll ratio.

$$d_{wp,f} = i_{p,f}^{\;2} \cdot i_{a,f}^{\;2} \cdot d_{roll,wheel,f} = 0.62^2 \cdot 1.44^2 \cdot 805 = 640 \, \text{Ns/m}$$

$$d_{wp,r} = i_{p,r}^{\;2} \cdot i_{a,r}^{\;2} \cdot d_{roll,wheel,r} = 0.7^2 \cdot 1.33^2 \cdot 875 = 760 \, \text{Ns/m}$$

The corresponding steering damper adjustment is calculated using equation 6.3. The front damper has to be turned open **12.6** clicks and the rear damper resistance has to be opened **13.5** clicks.

6.5.4 Monoshock specifications

The required monoshock stiffness can be calculated using the pushrod and monoshock ratios and the required wheel stiffness. When using a monoshock system, a single shock has to supply stiffness to one axle instead of one wheel. The needed axle stiffness is therefore 2*C_wheel. The wheel rates front and rear are **16800 N/m** and **19600 N/m** respectively. Equation 6.5 shows the relation between the wheel stiffness and the monoshock stiffness.

$$2 \cdot C_{wheel} = I_p^2 \cdot I_m^2 \cdot C_{monoshock} \qquad \text{(equation 6.5)}$$

The monoshock stiffness' front and rear are respectively **21900 N/m** and **20000 N/m**. The corresponding maximum monoshock stroke s_m can be calculated with equation 6.6, using the maximum wheel travel s_w of 51 mm.

$$s_m = I_p \cdot I_m \cdot s_w \qquad \text{(equation 6.6)}$$

The monoshock strokes front and rear are respectively **63mm** and **71 mm**.

Furthermore the minimal required spring volume is calculated using equation 6.7:

$$V_{spring} = \frac{C_{monoshock} \cdot s_m^2 \cdot G_{steel}}{\mu_{spring} \cdot \tau_{steel}^2} \qquad \text{(equation 6.7)}$$

Using G_{steel}=8.0e10 N/m^2 and τ_{steel}=6.0e8 N/m^2 and μ_{spring}=0.5 [-] the required front and rear spring volumes become 3.86e-5 m^3 and 4.48e-5 m^3 respectively.

The helical spring stiffness can be expressed using the material properties and spring dimensions. This is shown in equation 6.8.

$$C_{monoshock} = \frac{\Delta F}{\Delta s} = \frac{G \cdot d^4}{8 \cdot D_m^3 \cdot N_w} \qquad \text{(equation 6.8)}$$

With d the spring wire thickness, D_m the mean spring diameter and N_w the number of active coils. The spring volume can also be expressing using the spring dimensions.

$$V_{spring} = \pi \cdot D_m \cdot N_w \cdot \tfrac{1}{4} \cdot \pi \cdot d^2 \qquad \text{(equation 6.9)}$$

Equations 6.8 and 6.9 can be combined. Filling in the minimal required volumes, enables us to calculate the corresponding spring dimensions. Therefore one dimension variable has to be chosen and the other two can be calculated. Table 6.4 shows three options that comply for the front and rear monoshock spring.

	Spring dimension variable	Front monoshock	Rear monoshock
option 1	d [mm]	7.13	7.20
	N_w [-]	4.96	5.34
	D_m [mm]	62	62
option 2	d [mm]	7	7
	N_w [-]	5.30	6.51
	D_m [mm]	58	57
option 3	d [mm]	8	8
	N_w [-]	2.80	3.34
	D_m [mm]	87.5	85

Table 6.4: Three different options for the monoshock spring front and rear

For "option 1", D_m is chosen 62 mm, the spring just fits into the rectangular tube of 120x80x2.5 mm but the wire thickness is not standard. Options 2 and 3 show the complying spring dimension with standard wire thickness' of 7 and 8 mm. Using a d of 8 mm, D_m becomes too large and the spring does not fit into the tube.
Therefore option 2 is recommended, using a monoshock spring with a wire thickness d of 7 mm front and rear with a different number of active coils.

Finally the monoshock damping properties are determined. This is calculated using the pushrod and monoshock ratios and the required wheel damping from paragraph 4.1.

$$2 \cdot d_{wheel} = I_p^2 \cdot I_m^2 \cdot d_{monoshock} \qquad \text{(equation 6.10)}$$

Using equation 6.10 the required front- and rear monoshock damping are respectively **1390 Ns/m** and **1280 Ns/m**.

6.5.5 Suspension box design

Finally the complete suspension box design can be made with the right ratios and dimensions. The front suspension box design is showed step by step. Starting with the front monoshock having an unloaded length of 330 mm in figure 6.32.
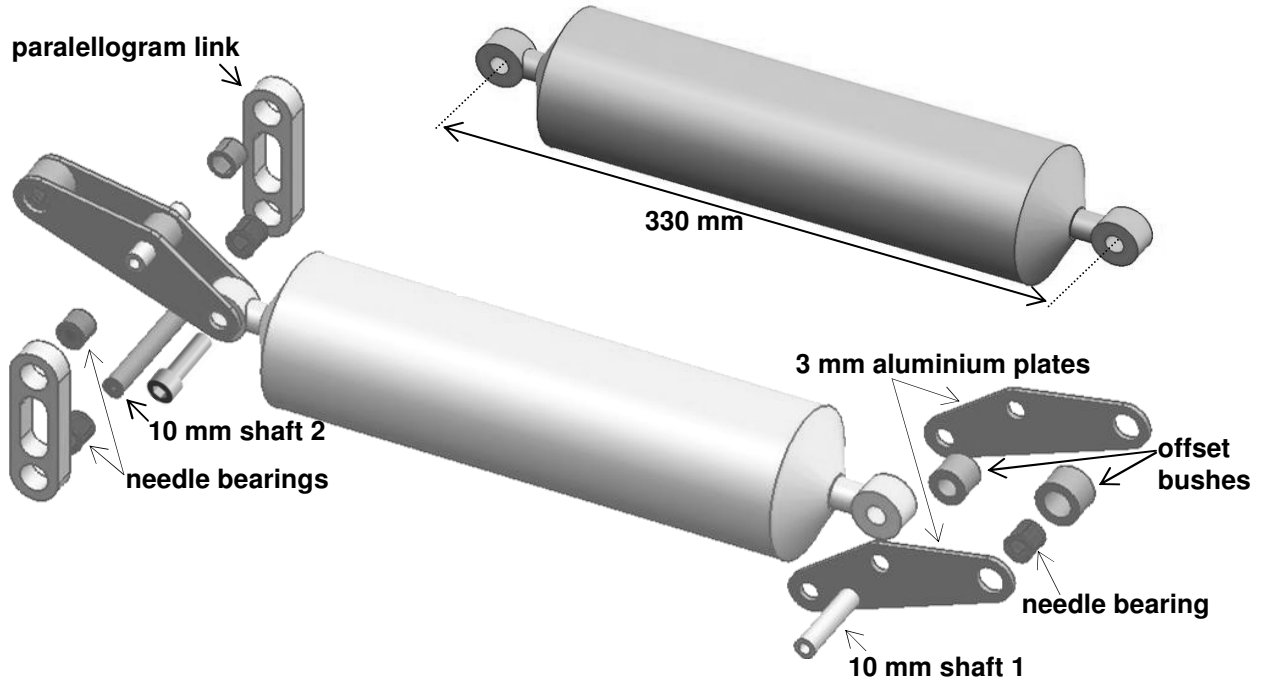
Figure 6.32: Exploded view of triangulalar plates, bearings and parallelogram links

First the aluminium triangular plates are welded onto the offset bushes, then the 10 mm shaft and a needle bearing are pressed in. The subassembly is bolted onto the monoshock using an M10 Allen bolt. Then needle bearings are pressed into the parallelogram links, and placed on both sides of the triangular plates.
Figure 6.33 shows the rocker, the main shaft and the anti-roll levers.
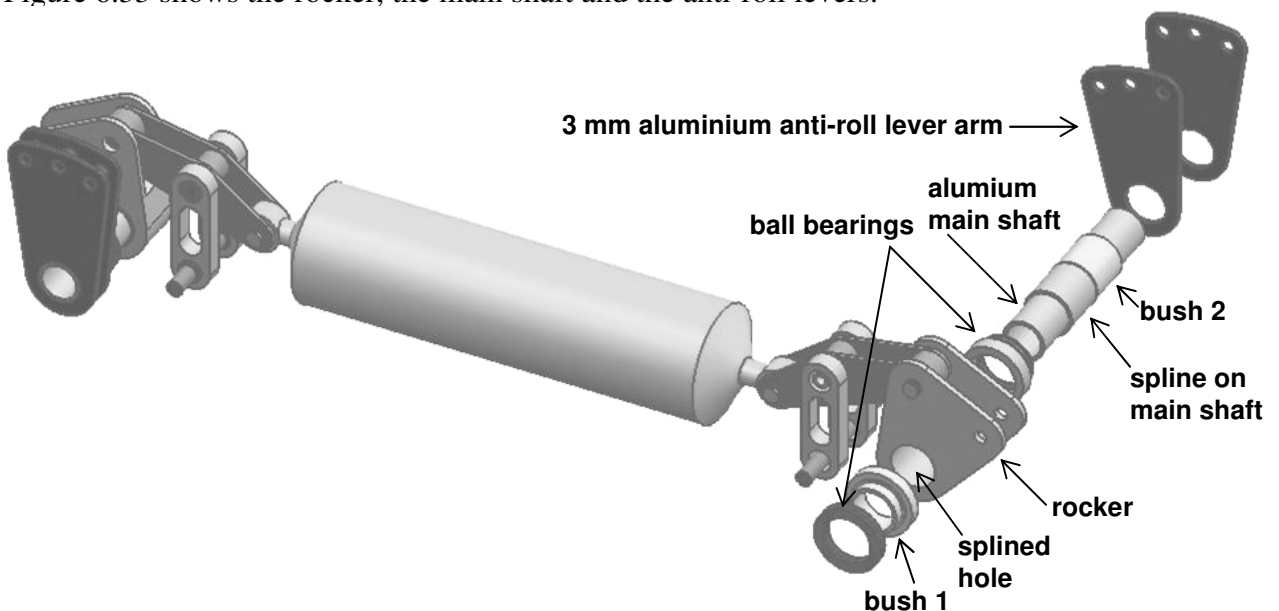
Figure 6.33: Placement of main shaft together with anti-roll lever arm and rocker

The anti-roll lever is made out of two 3 mm thick aluminum plates welded onto an aluminum shaft. This shaft has a spline. The rocker is also made out of aluminum and has a splined hole. Two ball bearings (appendix J) are pressed in the rectangular tube wall. The shaft with the lever is placed in the rectangular tube through the rocker inside the tube.

Figure 6.34 shows a detailed cross section of the main shaft placed in the rectangular tube.

1	rectangular tube	6	rocker
2	mounting ring ball bearing	7	filling bush 1
3	filling bush 1	8	locking ring
4	main shaft	9	anti-roll lever arms
5	ball bearing 61806-2z		
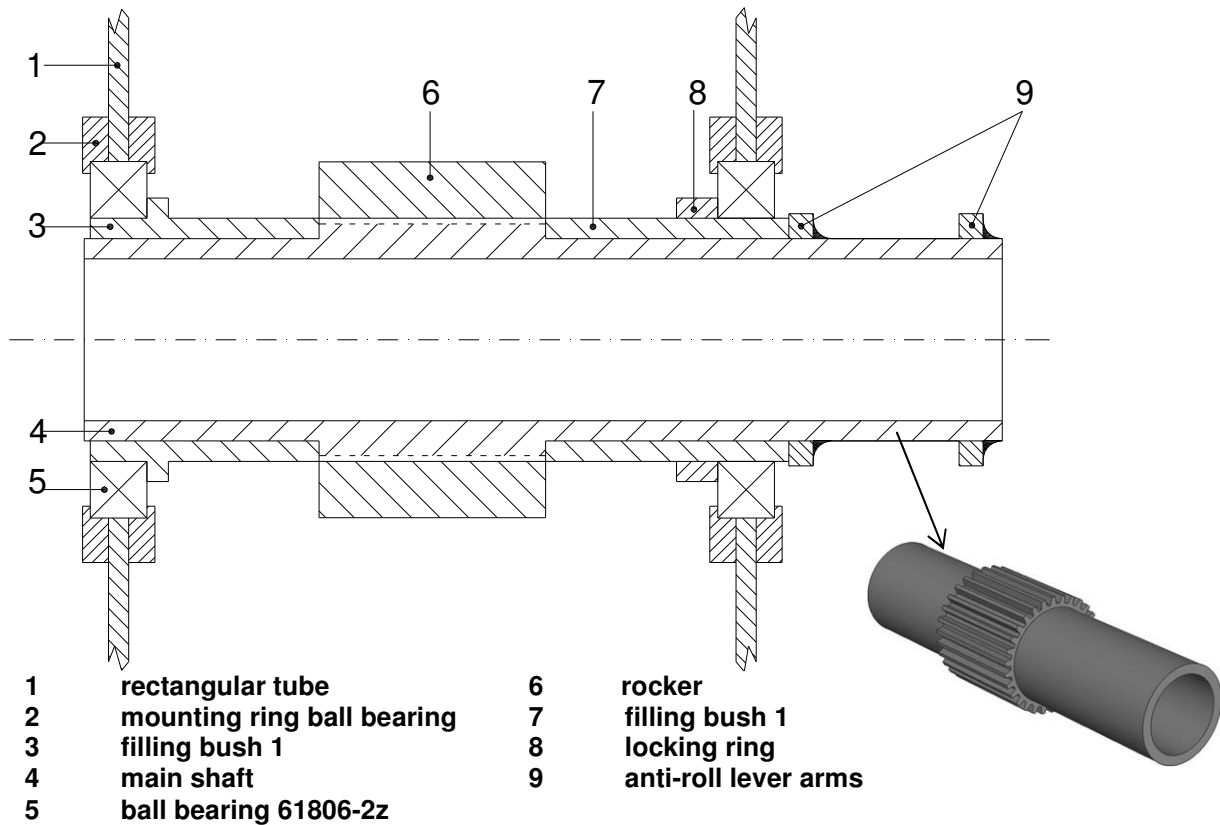
Figure 6.34: Mainshaft cross section

Due to the use of filling bushes the main shaft spline can be made using wire-EDM (wire electric discharge machining). When choosing another anti-roll lever arm length the locking ring is released and the mainshaft is slid out partly, rotated one spline groove and slid in again. The locking ring is placed and the rod is connected to the anti-roll lever arm using another hole.

Ball bearings are pressed into the third rocker block. Ball bearing specifications can be found in appendix I. Then the third rocker is put in the block using a 10 mm shaft and two M5 Allen bolts. The block is bolted onto the ball monorail guidance with four M4 Allen bolts. The ball monorail guidance system specifications can be found in appendix K. Figure 6.35 shows an exploded view of the sub assembly.
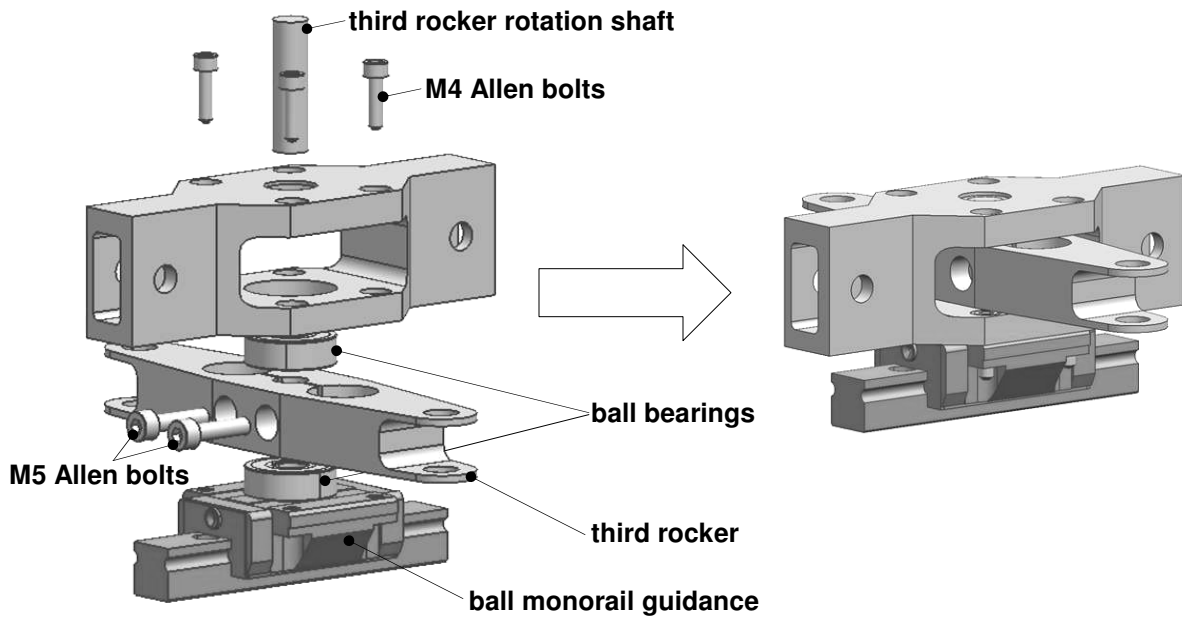
Figure 6.35: Exploded view of the third rocker rotation an translation system

Subsequently the assembly from figure 6.35 is mounted upside down into the rectangular tube of 120x80x2.5 using two brackets. This is depicted in figure 6.36
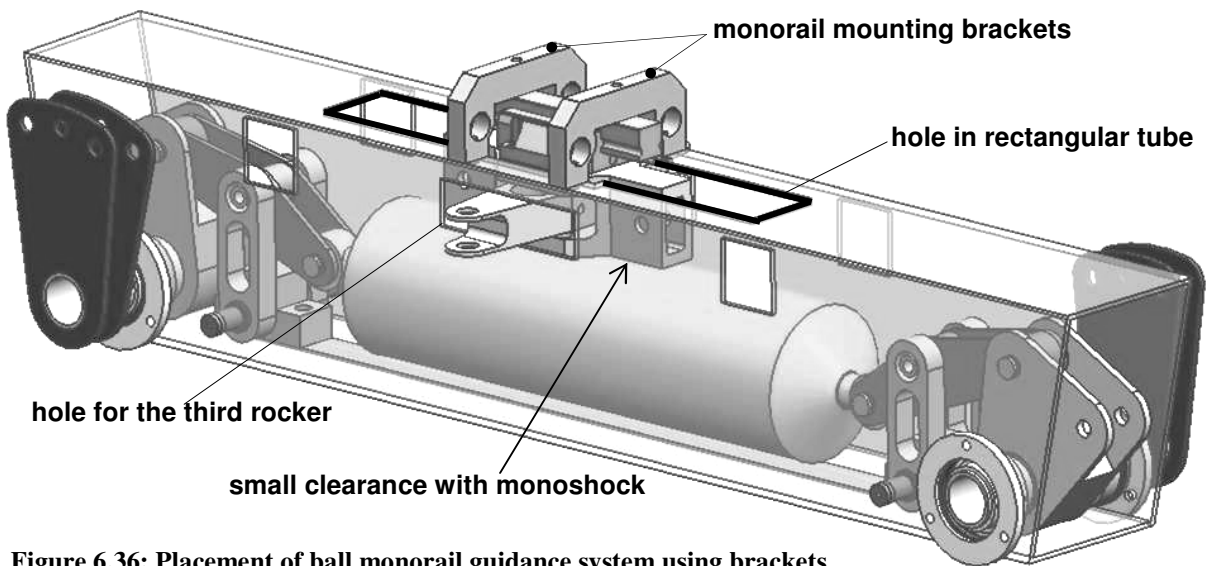
Figure 6.36: Placement of ball monorail guidance system using brackets

Figure 6.37 shows the next assembling steps. First the helical anti-roll springs are added. The springs are preloaded till half of their maximum compression and kept in place by two square traverse tubes of 30x30x3 mm welded to the rectangular tube. The helical spring ends are places on end caps preventing the spring from falling out by a small edge. Then the WP steering damper is added. The steering damper rod en can be put through a hole in the square 30x30x3 tube and through the helical anti-roll spring. It will be attached to the third rocker block using an M8 Allen bolt. The steering damper itself is fixed onto the rectangular tube using the original WP mounting bracket.
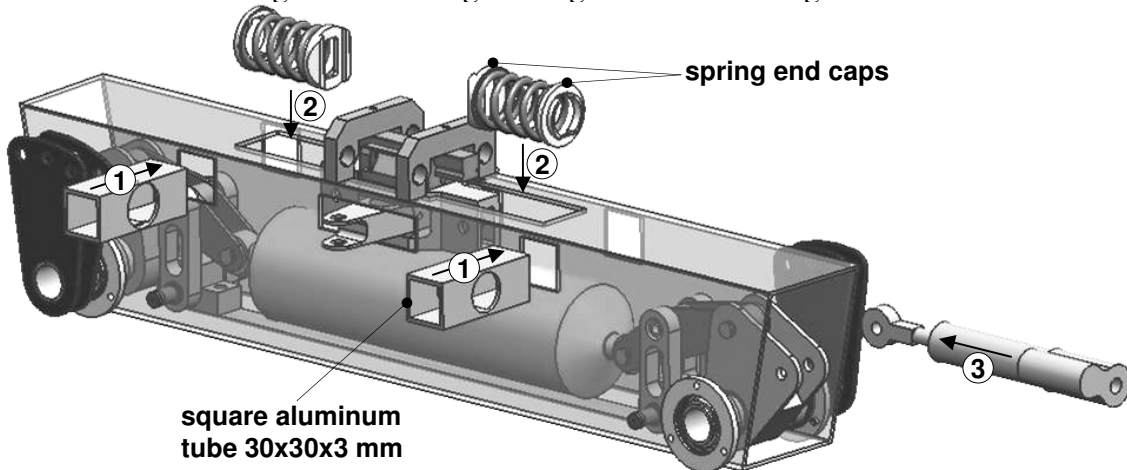
Figure 6.37: Spring and damper placement

Finally rods are added connecting the third rocker with the anti-roll lever arms using rod ends and M8 bolts. This is shown in figure 6.38.

Holes in the rectangular tubes can be made to ease the assembling and save weight these are not depicted.
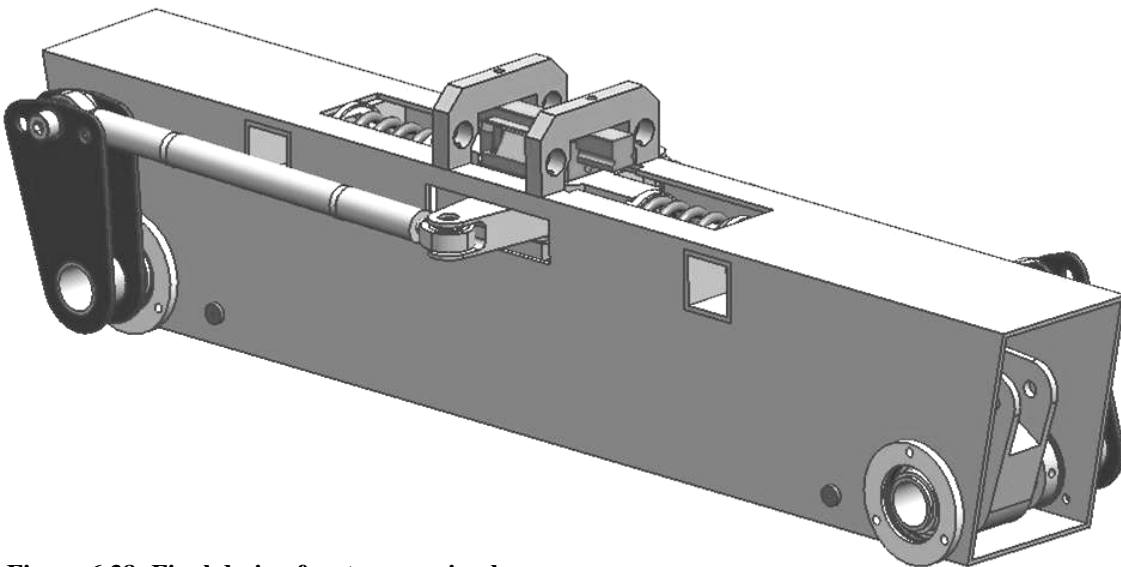
Figure 6.38: Final design front suspension box

The rear suspension box has minor differences with the front suspension box and is therefore not described separately.

7 FSRTE02 assembly

In this chapter the assembly is made by joining the suspension boxes and the chassis. In paragraph 7.2 the construction process is described and illustrated using photographs.

7.1 Unigraphics assembly

To mount the suspension boxes into the chassis, bent mounting plates are welded onto the rectangular tubes. Furthermore corner profiles of 2 mm thickness are glued and blind riveted onto the suspension boxes. This is shown in figure 7.1 for the front suspension box.

corner profiles

welded

bend mounting plates
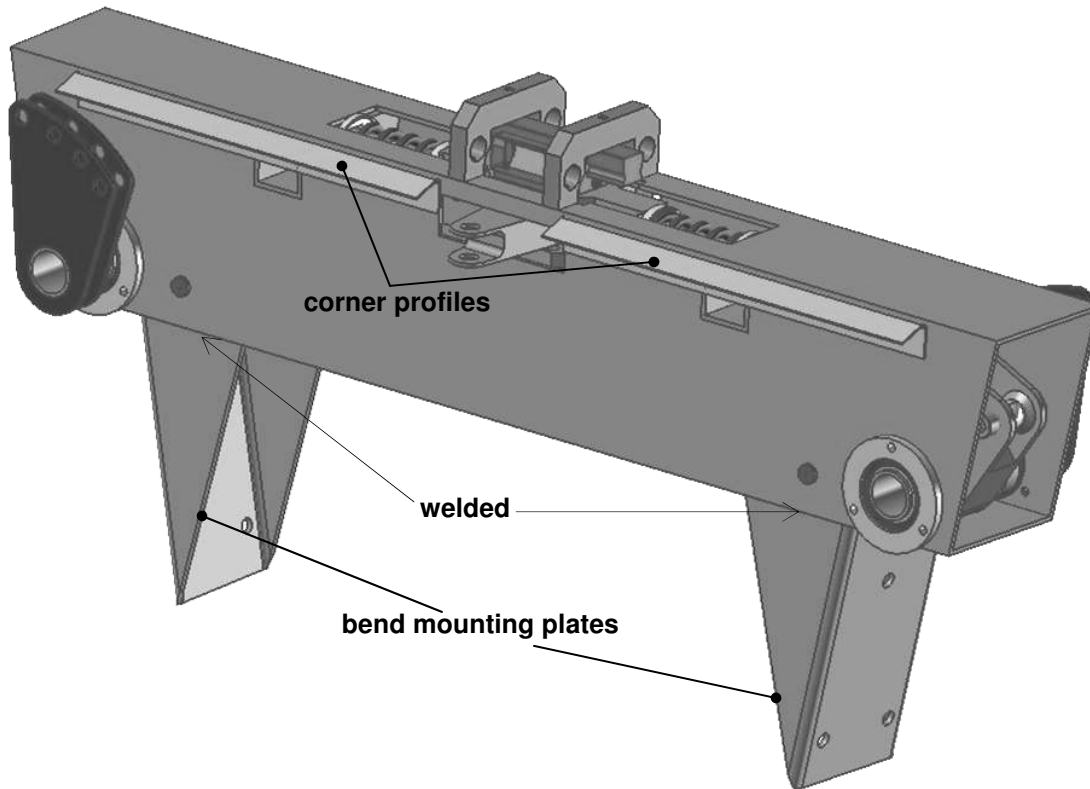
Figure 7.1: Front suspension box with bend mounting plates and corner profiles

The suspension box is mounted on the chassis using six M8 Allen bolts. The bolts are put in from the outside and reach through small inserts in the ALUCORE sidepanels. The bump forces are guided into the sidepanels through these inserts. The roll forces are guided into the front and rear covering plates through the corner profiles.
Figure 7.2 shows the placement of the suspension box rear and front.
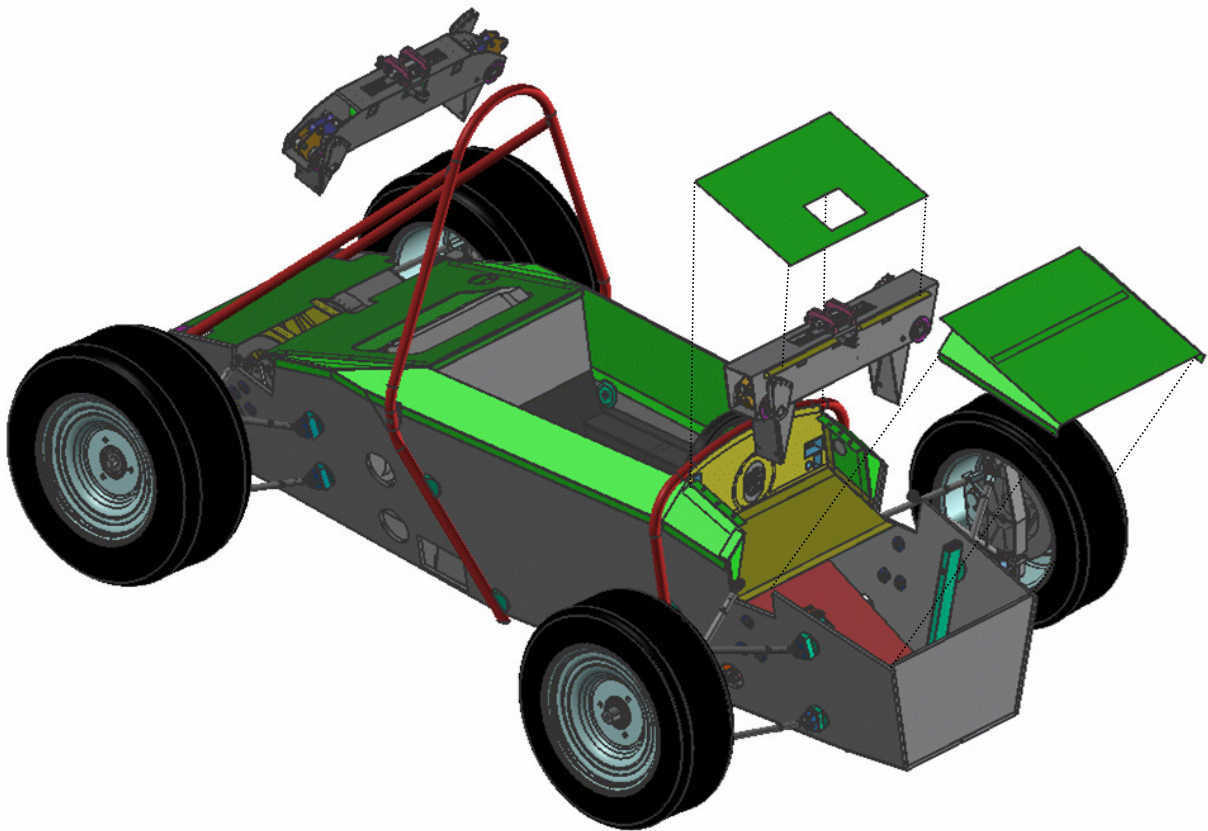
Figure 7.2: Placement of the suspension boxes front and rear onto the FSRTE02 chassis

Figure 7.3 shows the final assembly with a driver seated.

Figure 7.3: Final FSRTE02 assembly with driver seated

7.2 FSRTE02 construction.

The FSRTE02 construction is performed by students. Machined parts are mainly made by the GTD of the University. Appendix M shows the preferred sequence of the chassis construction. It is important to work accurately to prevent later fitting problems. Therefore the chassis has to be preassembled temporally as far as possible to see if all parts fit before gluing it the together. This paragraph illustrates the building process till thus far.

First the chassis halfs are watercutted and bent, this is shown in figure 7.4
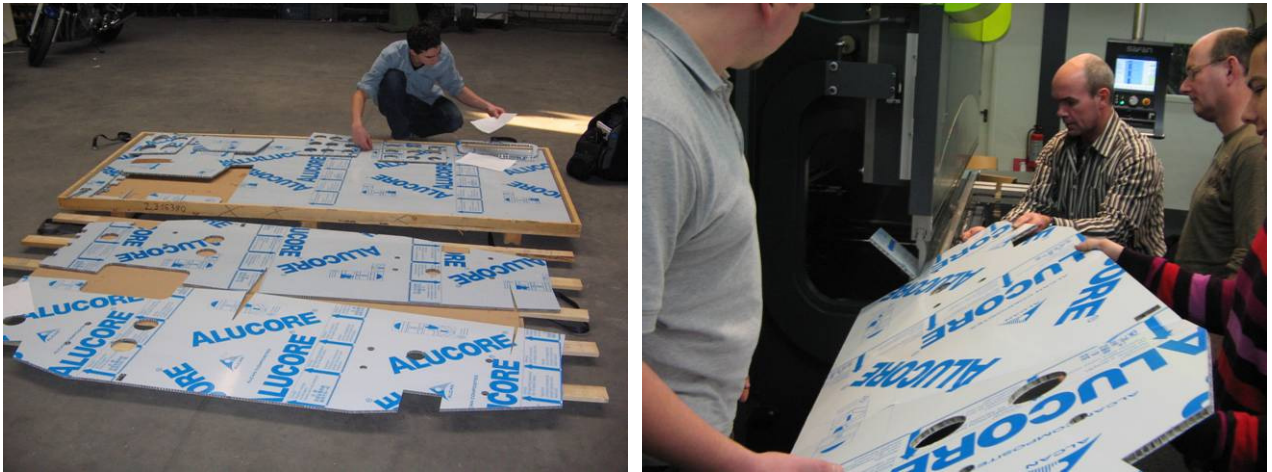
Figure 7.4: Watercutted layouts and bending both halfs on the press brake

A table of 350 mm height has been built using a heavy steel frame with an MDF tabletop. On this table a drawing is spread with the outlines of the bottom panels. Furthermore sidepanel supports rigs are mounted onto the table.

Then both chassis halfs are placed onto the table and aligned onto the bottom outlines. They are fixed using weights, pressing the bottom panel onto the table. The bottom seam is joined by gluing on a strip pressed by weights. The rearframe is placed temporally to ensure the rear chassis width will be correct. This is shown in figure 7.5a.

Figure 7.5 a: Gluing the bottom seam   b: Gluing in the rearframe
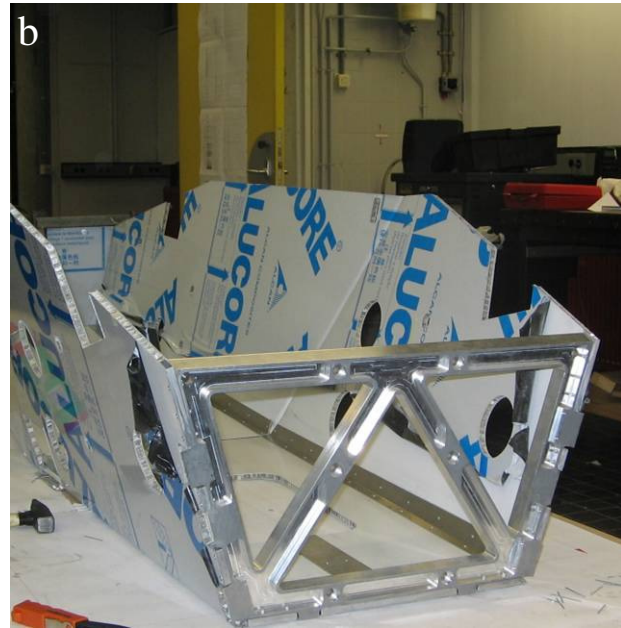
Then the rearframe is glued in using the milled rectangular tubes, this is depicted in figure 7.5b. Then the bent ALUCORE edges are reinforced by gluing in a corner profile. This can also be seen in figure 7.5.b.

The next step is to attach the frontpanel. Then the torsion tubes the side impact and the sloped floorpanel are bent and glued in.

Figure 7.6 shows the bending of the torsion tube.

Figure 7.6: Bending of torsion tube

This is the chassis construction till thus far.

8 Conclusions and recommendations

In this chapter the final result will described in conclusions. Then recommendations are made to help improve this design and give some ideas for the FSRTE03.

8.1 Conclusions

The conclusions are arranged per chapter.

General FSRTE02 properties
The wheelbase will be **1550 mm**, the front and the rear track will be **1250 mm** and **1200 mm** respectively. The total car mass will be **295 kg** including an 80 kg driver, the center of gravity height is **317** mm. The front to rear weight distribution is 46/54, using 6 inch wide front tires and and 8 inch wide rear tires, the contact pressures will be equal. Maximum acceleration is **1.24 G**, cornering can be done with a maximum lateral acceleration of **1.6 G** and maximum braking is done with **1.55 G**.

Chassis properties
A box structure has a much higher specific stiffness than a tubular spaceframe structure within the same volume. Therefore the chassis is mainly made out ALUCORE panels. These prefabricated panels consist out of two 0.5 mm aluminium skins and a 9 mm aluminium honeycomb core. The panels can be shaped using watercutting machine and a press brake and the complete joint can be glued together. The FSRTE02 chassis shape is based on the FSRTE01 shape but torsion stiffness is increased by **300%**.

Suspension properties
The wheel rates front and rear are **16800 N/m** and **19600** N/m respectively. The maximum chassis roll will be 2° including the tire compression. The front roll center height will be **10 mm** and the rear roll center height will be **97 mm** resulting in an equal roll moment front and rear. Both the front and rear roll stiffness will be **22000 Nm/rad**. The static camber will be 3.15^o. At the rear suspension **50% anti-squat** is applied. At the front suspension **50% anti-dive** is applied. The steering geometry is adjustable from parallel steering to a full Ackermann steering geometry.

Chassis design
The chassis consists out of two nearly symmetrical halfs, joined by two aluminum glued on strips. The front- and seatpanel and the rearframe are glued in using corner profiles and blind rivets. The torsion tubes are made out of 1 mm thick aluminium plates as well as the sloped floorpanel and the rear and front covering panels. The side impact is made out of 1.5 mm thick aluminum plate. All part layouts are optimized on minimum seam length and are made using lasercutting. The front and rear roll hoops are placed around the chassis and fixed from the inside. The dashboard is a sandwich structure of two 1 mm thick aluminium outer layers and a 25 mm thick polyurethane core. The steering system transmission is mounted in a 25 mm thick housing which is countersunk into the dashboard. The suspension connection rods will be mounted onto the rearframe and onto the front roll hoop. The remaining connection rod points are made using an insert that

reaches through the ALUCORE panel. The in-plane suspension force component is guided into the ALUCORE panel. The perpendicular force component is distributed into the chassis by a support beam on the inside. Space is reserved for the suspension boxes.

Suspension design
The different suspension mounting points are fully detailed. The A-arms are joined on the upright side by a connector. The lower rear connector is enlarged to prevent it from interfering with the flexplates. Different suspension unit concepts have been considered. The best concept is the suspension box concept. The functioning is based on the FSRTE01 design but all components are mounted into a standard aluminium rectangular tube of 120x80x2.5. Needle- and ball bearings are used in the pivoting points and a ball monorail guidance system is used for the third rocker translation. Roll stiffness can be adjusted by changing the lever arm length and a motorcycle steering damper is added for adjustable roll damping. The suspension box assembly can be bench built and tested prior to installation.

FSRTE02 construction
The suspension box is placed into the chassis and mounted using M8 Allen bolts.
For the building of the chassis a building rig is made. A flat solid table of 350 mm height is used. On this table both ALUCORE chassis halfs are aligned and joined together. Then the frontpanel and the rearframe are glued in. Subsequently the side impact, the sloped floorpanel and the torsion tubes are glued in. The roll hoops are placed using special inserts and the dashboard is glued in. Finally the rear and front coverplates are bolted on to reach full torsion stiffness.

8.2 Recommendations

First an enumeration has been made with specific FSRTE02 issues.

- Too little attention is paid to the tire choice and the tire characteristics. Different tires have to be compared. Therefore more tire data needs to be obtained from tire manufacturers or by doing tire tests.
- The scrub radius should be reduced.
- The caster and trail have to be looked at in more detail.
- FEM analysis has to be done on the rearframe to be able to see whether mass can be saved or stiffness can be gained.
- Mass could be saved on side impact using ALUCORE panels
- The front left engine bracket has to be reinforced to be able to withstand lateral engine inertia forces.
- The radiator should be made smaller.
- Flexplates need more optimization to reduce weight.
- Adjusting the monoshock preload is difficult because it is placed inside the rectangular tube so this should be solved.
- The monoshock has to be choosen fast so the suspension box design can be fine tuned.
- Weight can be saved on bolts, which are over dimensioned on some parts, either by going to aluminium bolting or by redesigning for smaller size.
- Air ducting in the engine compartment has to be examined.

Below a list of recommendations concerning the FSRTE03 design and some general issues is made.

- All team members should be able to work with Unigraphics. Parts should be designed in such a way that they are easy to adapt by changing a single parameter which any team members should be able to find in the part file.
- Bottom up assembly in Unigraphics should be applied. This way holes or other features can easily be made through different parts after assembling them.
- The FSRTE03 design should be completely parametric. For example when the roll center height changes, the complete assembly suspension geometry should change along.
- The Aprilia SXV 5.5 engine should be looked at seriously. The engine has a high power to weight ratio and would therefore be very suitable for the FSRTE03.
- Little mass can be saved on the FSRTE02 aluminium chassis structure (12% off car weight). Mass saving must be done simultaneously on all parts.
  The feasibility of a laminated carbon structure can therefore be examined.
- The FSRTE02 suspension performance should be used to design the FSRTE03 suspension.

Bibliography

- John C. Dixon, *Tires suspension and handling*, SAE, 1996

- P.C.J.N. Rosielle E.A.G. Reker, *Constructieprincipes 1*, March 2000

- W. Berkhout, *Design for a formula student racecar*, October 2004

- D.O. de Kok, *Optimal performance of a racing car on a circuit*, March 9, 2001

- Andries van Berkum Stijn Aben, *Eindoverbrenging voor de FS racewagen*, March 12, 2004

- Jasper Simons, *Stuurinrichting voor formula student, December* 2004

- P. Brinkgreve R. Brinkgreve M.J.M. van der Velden, *Wegligging van automobielen*, 1969-1972

- F. Sass Ch. Bouché A. Leitner, *DUBBEL Taschenbuch für den Maschinenbau,* Springer-Verlag, 1994

- *Racecar engineering,* November 2003

- Dr. Ir. I.J.M. Besselink, *Vehicle Dynamics lecture notes*, 2003

- Dr. Ir. I.J.M. Besselink, *Advanced Vehicle Dynamics lecture notes*, 2004

Internet sites

http://www.avonracing.com/tyres

http://www.aluminium-info.nl

http://www.alucore.com

http://www.alcanairex.com

http://www.hexcel.com

http://www.favonius.com/soaring/foams/foams.htm

http://www.netcomposites.com/education.asp?sequence=53

http://www.suzuki.nl

http://www.aprilia.com

http://www.formulastudent.com

http://www.keizerwheels.com

http://www.safan.nl

http://www.wp.nl

http://www.tevema.com

http://www.ina.nl

http://fsae.utoronto.ca

Appendices

Appendix A: Static mass distribution

The static mass distribution on the wheels is calculated by taking into account all of the cars parts heavier than 5kg. All mass centers are drawn below with their coordinates in table A.1
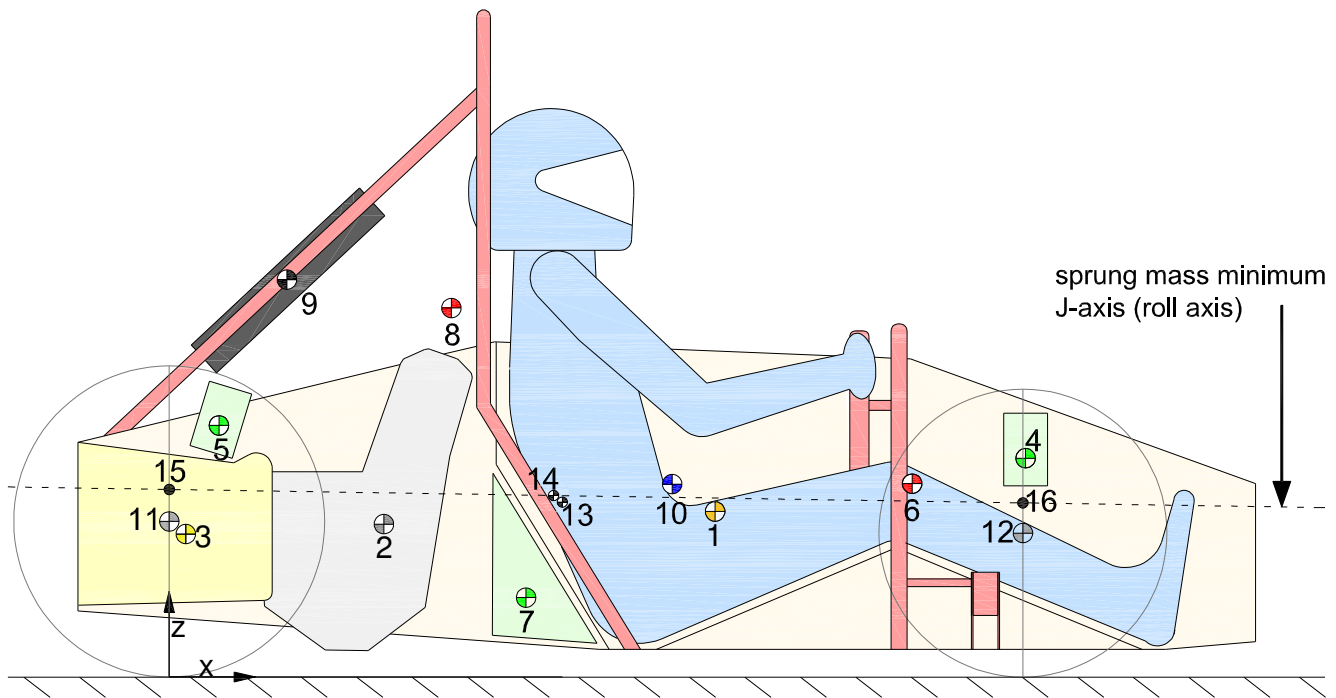
Figure A.1: Car side view with all parts over 5 kg

Number (fig A.1)	Part name	Mass [kg]	x-coordinate [mm]	z-coordinate [mm]
1	Chassis and small components	26.5	990	300
2	Engine (exhaust included)	60	400	275
3	Drivetrain	17	30	260
4	Suspension system front	8	1550	400
5	Suspension system rear	8	90	460
6	Steering, dashboard and front rollhoop	10	1370	350
7	Petrol tank and battery	13	650	140
8	Rear rollhoop	7.5	510	670
9	Radiator	5	210	720
10	Driver	80	910	345
11	Both front wheels	30	1550	261
12	Both rear wheels	30	0	282
	Total mass	295		

Table A.2: Sprung and unsprung (front- and rear wheels) masses and positions

A matlab file is used to calculate the resulting center of gravity of the sprung + unsprung mass. This determines the static weight distribution of the car.

Furthermore the sprung mass minimum moment of inertia J-axis is determined; this axis is drawn in figure A.1. The results are plotted in table A.2 below:

Number (fig A.1)	Point name	x-coordinate [mm]	z-coordinate [mm]
13	Combined center of gravity sprung + unsprung mass	713	317 (h_{cg})
14	Center of gravity sprung mass	697	329
15	Acting point centrifugal force rear	0	340 (h_{cg-r})
16	Acting point centrifugal force front	1550	316 (h_{cg-f})

Table A.2: Combined centers of mass

The z-coordinates are used in the lateral load transfer calculation therefore they are called centers of gravity rear and front, h_{cg-r} and h_{cg-f} respectively.
The moment of inertia J_{roll} about the roll axis is approximately 9 kgm^2.

Appendix B: friction coefficients on dry and wet road

The friction coefficient is a linear function of the tire normal force, below the graphs and the functions for the front and rear tires on dry and wet road are depicted.

$$\mu_{lat-f} = \mu_{long-f} = 0.87 - 0.64e\text{-}4 * F_{N-f}$$
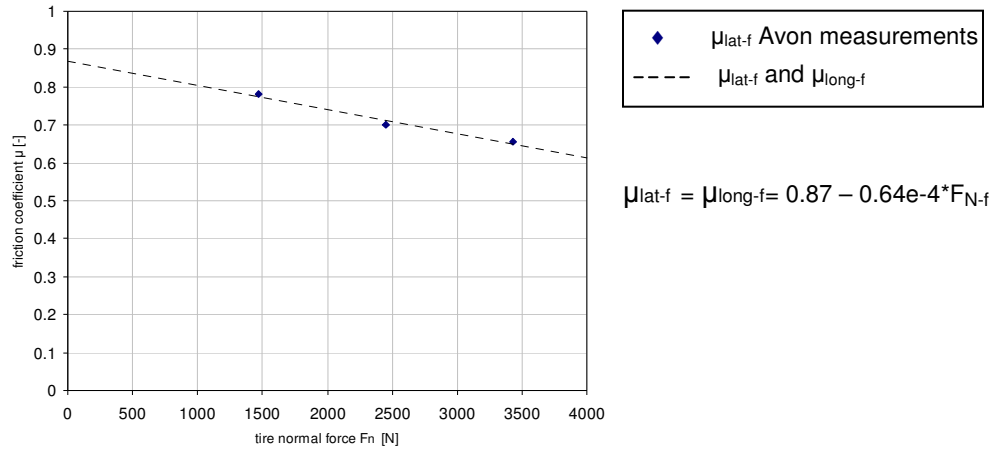
Figure B.1: μ_{lat} **and** μ_{long} **at a slip angle of** 7° **for the front tire on wet road**

$$\mu_{lat-r} = \mu_{long-r} = 2.00 - 1.85e\text{-}4 * F_{N-r}$$
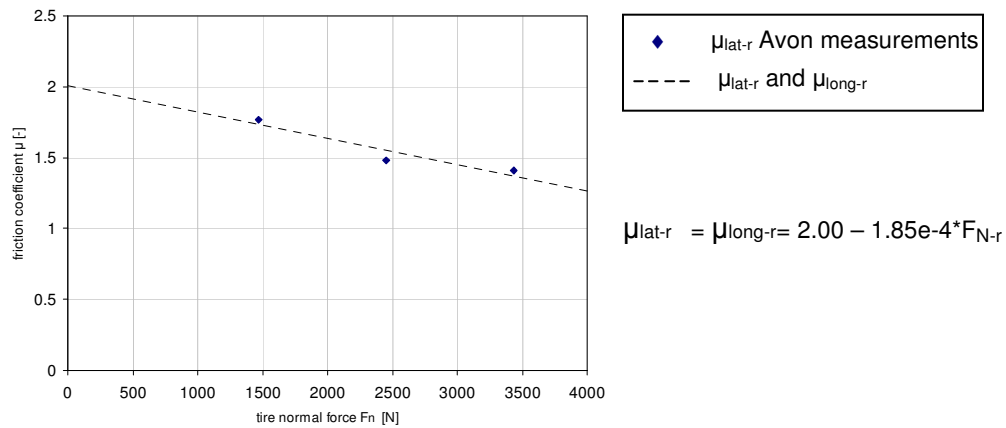
Figure B.2: μ_{lat} **and** μ_{long} **at a slip angle of** 7° **for the rear tire on dry road**

$$\mu_{lat-r} = \mu_{long-r} = 1.00 - 0.93e\text{-}4 * F_{N-r}$$
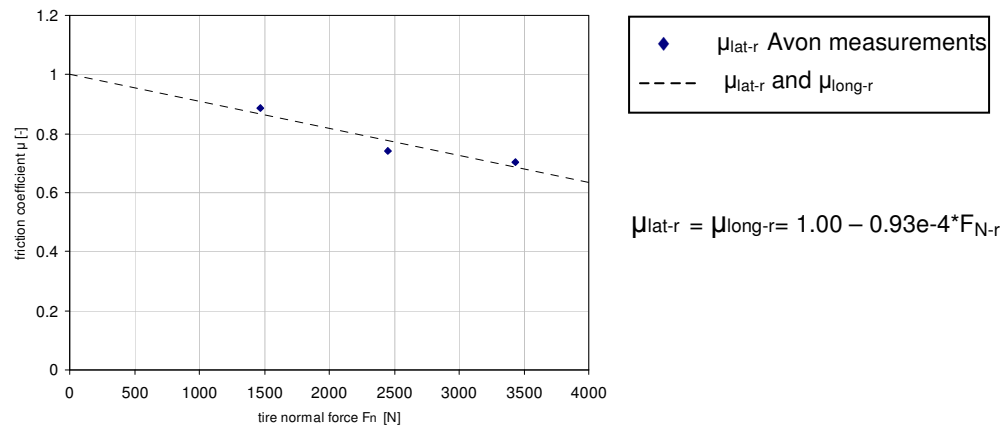
Figure B.3: μ_{lat} **and** μ_{long} **at a slip angle of** 7° **for the rear tire on wet road**

Brand name	Material type	density [kg/m³]	Compression strength [Mpa]	Compression modulus [Mpa]	Tensile strength [Mpa]	Tensile modulus [Mpa]	Shear strength [Mpa]	Shear modulus [Mpa]	Allowable temperature [C]
KAPEX® C51	PU-foam	60	0.45	25	0.55	10	0.45	5.0	140 c°
HEREX® C70	PVC-X-foam	60	0.9	58	1.3	45	0.8	22	-
HEREX® C71 et	PVC-X-foam	60	0.95	70	1.4	38	0.85	20	122 c°
Divinycell HT	PVC-X-foam	50	0.7	75	1.5	95	0.6	19	130 c°
Klegecell	PVC-X-foam	55	0.7	76	1.2	38	0.6	19	130 c°
AIREX® R63	PVC-L-foam	60	0.38	30	0.9	30	0.5	11	-
AIREX® R82	PEI-foam	60	0.6	46	1.7	45	0.8	18	160c°
Rohacell	PMI-foam	51.4	1.01	-	1.68	62.3	0.72	20.43	190 c°
Core-cell	SAN-foam	58.4	0.56	52	0.89	45	0.46	12.9	65c°
Hexweb ACG ACG-3/8-3.3	Alu3000 honeycomb	52.9	2.34	634.3	-	-	0.89	150	Fire resistant and heat conducting
Hexweb HRH HRH-36-3.2-48	Nomex honeycomb	48	2.33	127.5	-	-	0.86	60	Fire resistant and heat isolating

Table C.1: Sandwich core materials

Appendix D: FSRTE02 chassis FEM analysis results

The FSRTE02 chassis strength is analyzed by applying three different load cases, accelerating (figure D.1), braking (figure D.2) and cornering (figure D.3).
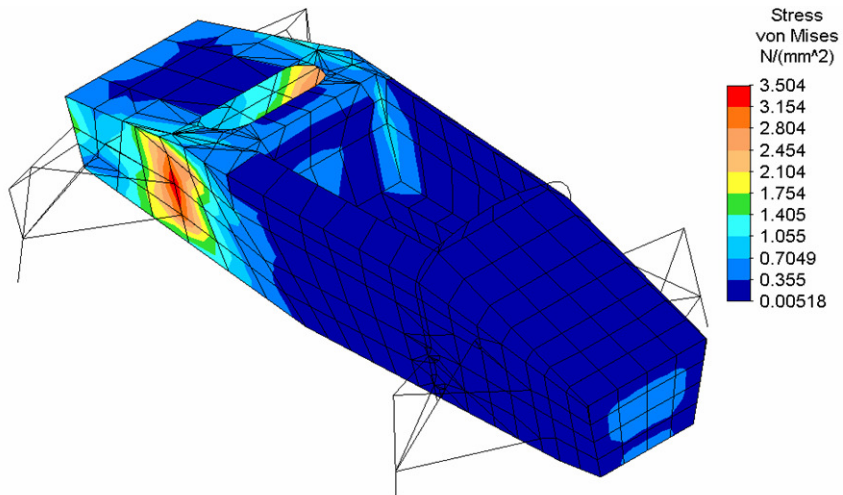
Figure D.1: Stresses during maximum acceleration
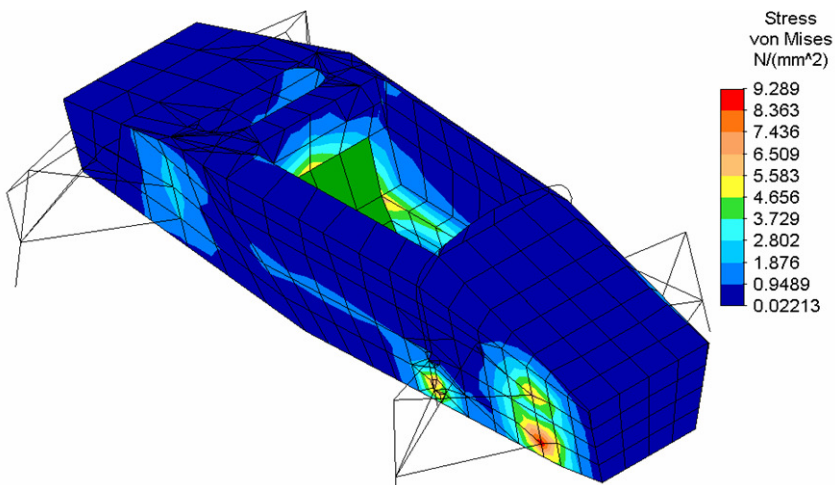
Figure D.2: Stresses during maximum braking
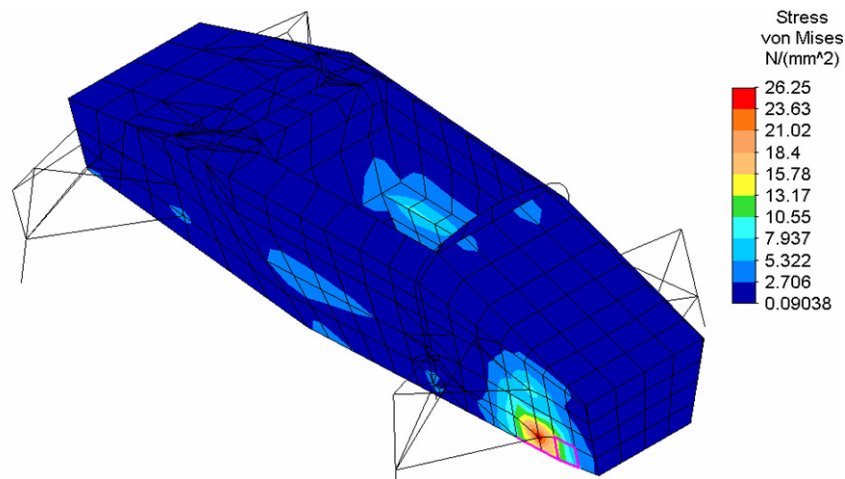
Figure D.3: Stresses during maximum cornering

Appendix E: Radial tire stiffness

The radial tire stiffness is calculated using the tire data and a trendline.
The trendline slope indicates the tire stiffness.
The results for the front and rear tire are plotted in figure E.1 and E.2.
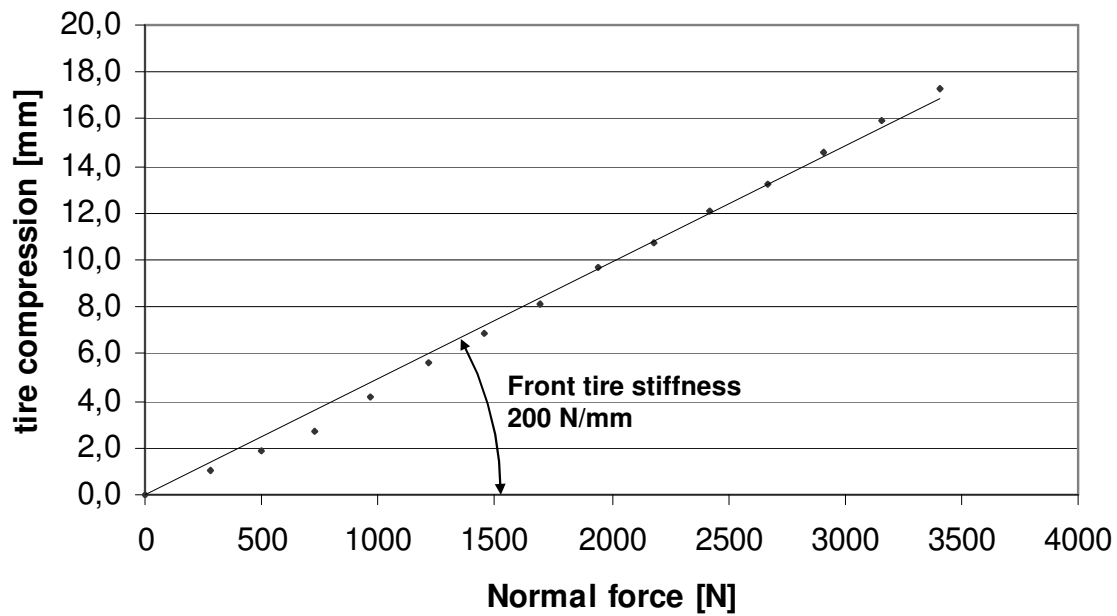
Figure E.1: Tire compression as a function of tire normal force for the front tire
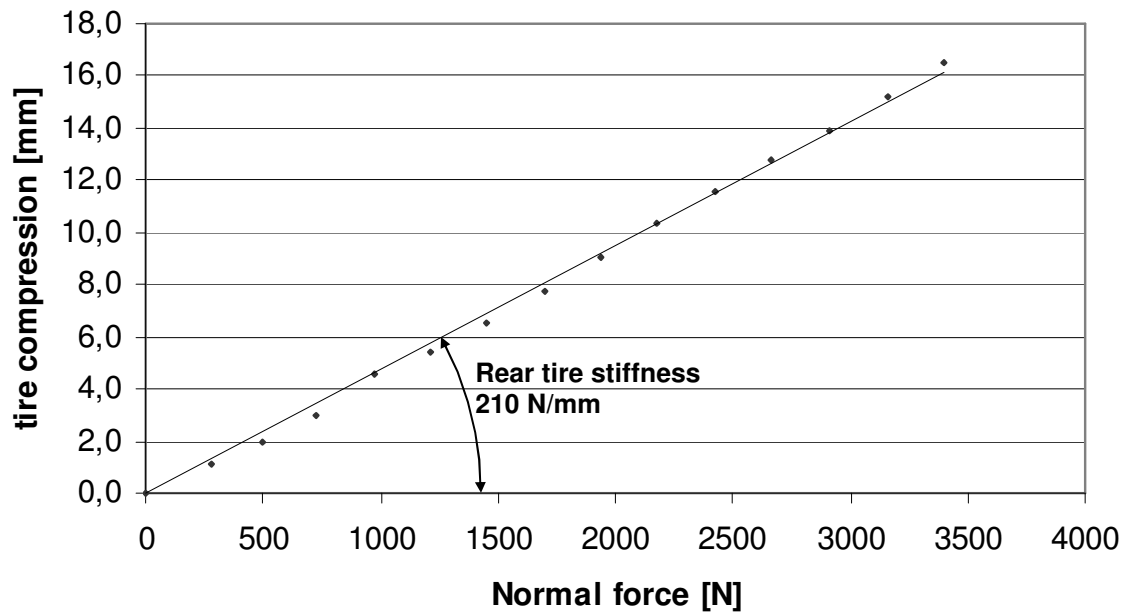
Figure E.2: Tire compression as a function of tire normal force for the front tire

Appendix F: Standard driver seated in FSRTE02 chassis

The rules prescribe a two dimensional driver template. It represents the 95th percentile male. It is quoted below:

A two dimensional template used to represent the 95th percentile male is made to the following dimensions:

- A circle of diameter 200 mm (7.87 inch) will represent the hips and buttocks.
- A circle of diameter 200 mm (7.87 inch) will represent the shoulder/cervical region.
- A circle of diameter 300 mm (11.81 inch) will represent the head (with helmet).
- A straight line measuring 490 mm (19.29 inch) will connect the centers of the two 200 mm circles.
- A straight line measuring 280 mm (11.02 inch) will connect the centers of the upper 200 mm circle and the 300 mm head circle.

This has been used to create a sideview of the driver when seated in the FSRTE02 chassis. Furthermore ergonomic data has been used to finish the legs of the driver and to create the section A-A which.
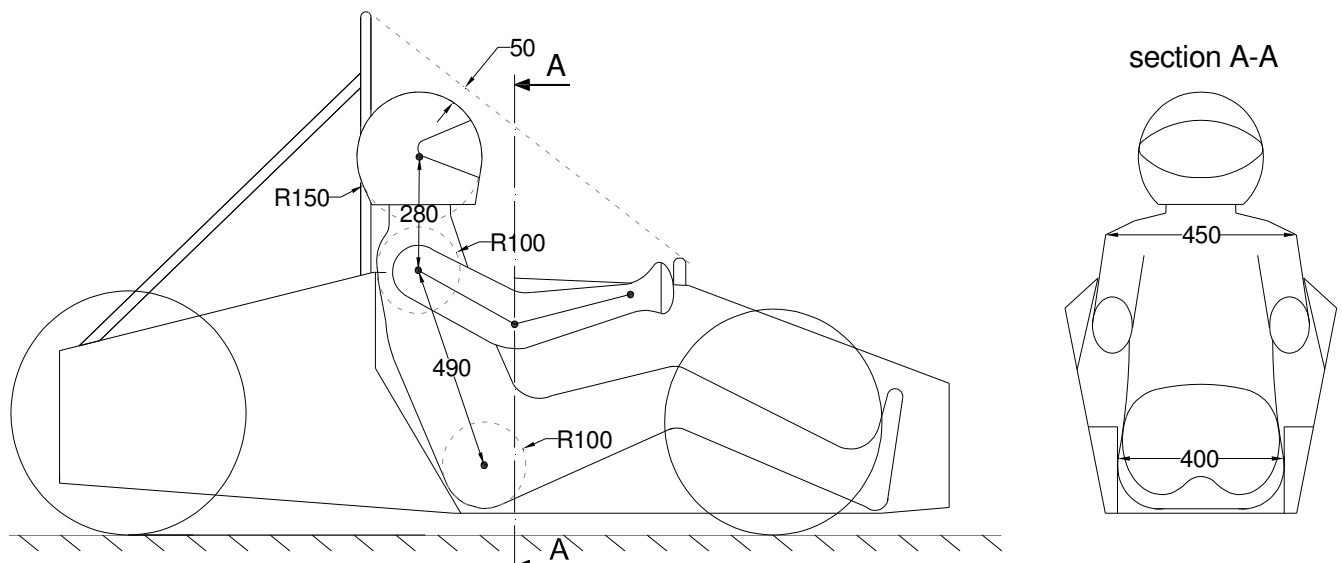
Figure F.1: Sideview and cross section at the elbow of standard driver.

Appendix G: suspension coordinates

The suspension coordinates are determined using Autocad. They are given at ride height. The origin is placed between the rear tires contact points on the road. Figure H1 shows the suspension point naming and table H.1 shows the description and coordinates of each point.
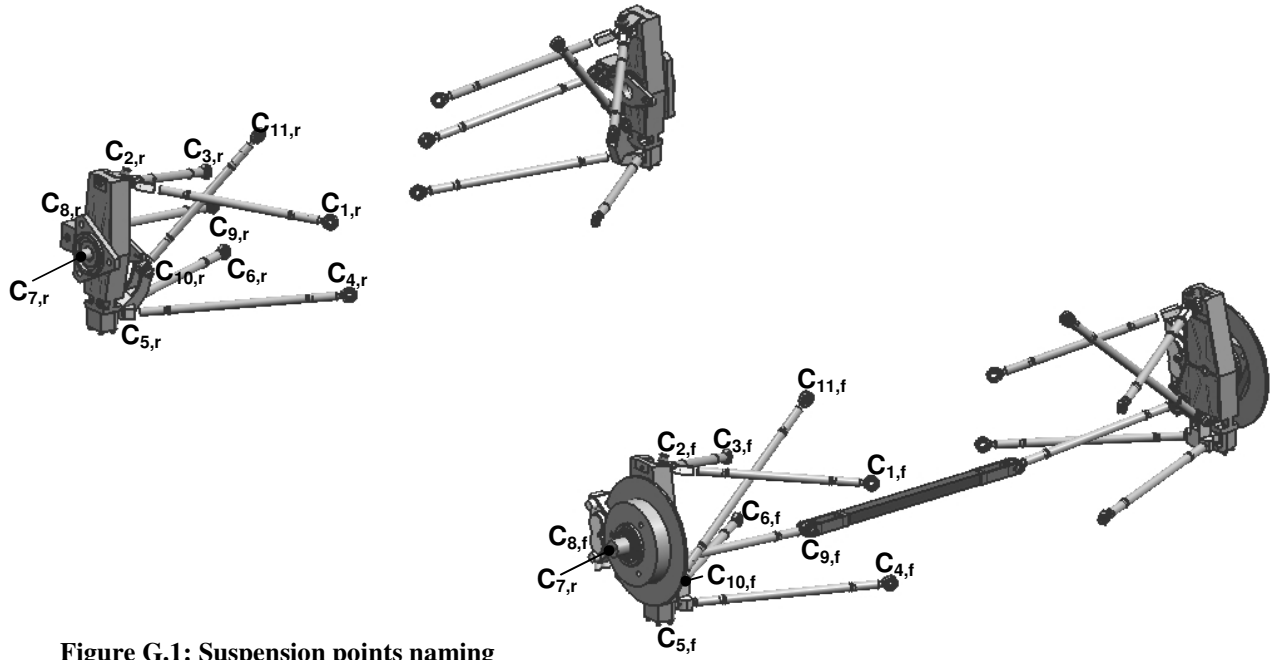
Figure G.1: Suspension points naming

point	description	coordinates x y and z in mm
$C_{1,f}$	connection upper A-arm front - chassis	1718, 277, 315
$C_{2,f}$	connection upper A-arm upright	1523, 596, 363
$C_{3,f}$	connection upper A-arm rear - chassis	1336, 296, 251
$C_{4,f}$	connection lower A-arm front - chassis	1717, 237, 117
$C_{5,f}$	connection lower A-arm upright	1561, 627, 123
$C_{6,f}$	connection lower A-arm rear - chassis	1335, 271, 127
$C_{7,f}$	connection upright - wheel centre	1542, 611, 245
$C_{8,f}$	connection upright - steering rod	1478, 595, 157
$C_{9,f}$	connection steering rod - steering rack	1478, 231, 140
$C_{10,f}$	connection lower A-arm - pushrod	1561, 627, 123
$C_{11,f}$	connection pushrod - rocker	1550, 294, 372
$C_{1,r}$	connection upper A-arm front - chassis	275, 313, 360
$C_{2,r}$	connection upper A-arm upright	0, 566, 402
$C_{3,r}$	connection upper A-arm rear - chassis	-144, 247, 310
$C_{4,r}$	connection lower A-arm front - chassis	275, 274, 215
$C_{5,r}$	connection lower A-arm upright	0, 599, 162
$C_{6,r}$	connection lower A-arm rear - chassis	-136 213, 147
$C_{7,r}$	connection upright - wheel centre	0, 599, 282
$C_{8,r}$	connection upright - tie rod	-86, 570, 282
$C_{9,r}$	connection steering rod - steering rack	-149, 236, 238
$C_{10,r}$	connection lower A-arm - pushrod	0, 599, 162
$C_{11,r}$	connection pushrod - rocker	93, 352, 424

Table G.1: description and coordinates of each suspension point

Appendix H: Rod end specification

This rod end is used for the connection rods, the pushrods and for the anti-roll system. Specifications are stated in figure H.1

INA Rod ends GAKR8-PW
maintenance-free, to ISO 12 240-4, right hand thread
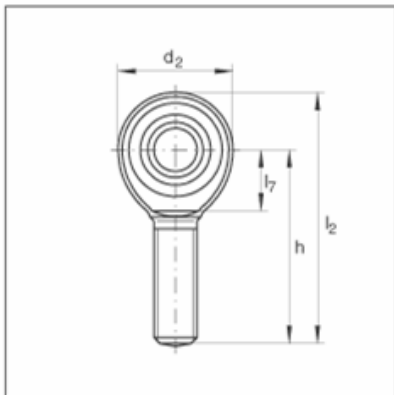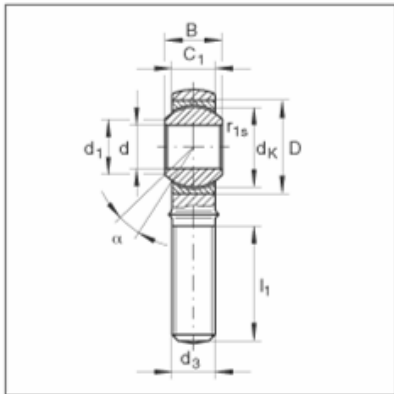
d	8 mm	Bore tolerance: H7 (arithmetic mean value)
		Tolerance: +0,057 / 0
d_2	24 mm	
l_2	54 mm	

B	12 mm	Tolerance: 0 / -0,12
C_1	9 mm	
D	19 mm	
d_1	10,3 mm	
d_3	M8	
d_K	15,875 mm	
$G_{r\,max}$	0,035 mm	Max. radial internal clearance
$G_{r\,min}$	0 mm	Min. radial internal clearance
h	42 mm	
l_1	25 mm	
l_7	0 mm	
$r_{1s\,min}$	0,3 mm	
α	14 °	

		For a left hand thread, R is replaced by L - (example: GAKL); For a right hand thread, L is replaced by R - (example: GAKR)
m	0,038 kg	Mass
C_r	12900 N	Basic dynamic load rating, radial
C_{0r}	12900 N	Basic static load rating, radial
		Basic load rating of housing

Figure H.1: Rod end specifications

Appendix I: Third rocker ballbearing specifications

For the third rocker in the front and rear suspension box INA 60002RS ball bearings are used. Specifications from INA are stated in figure I.1.

FAG Radial ball bearings 6000-2RSR
main dimensions to DIN 625-1, lip seals on both sides
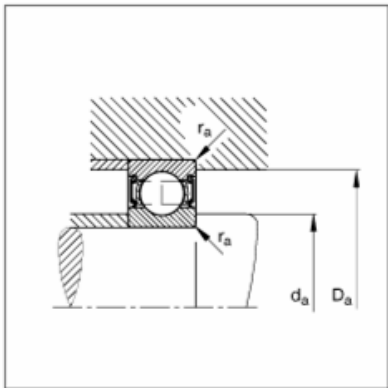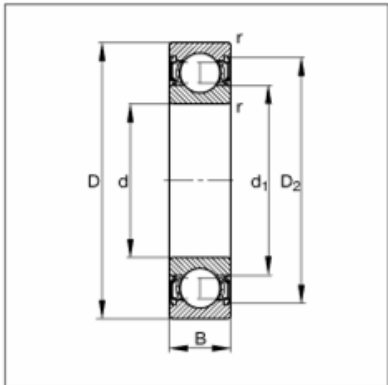
d	10 mm	
D	26 mm	
B	8 mm	

D_2	22,5 mm	
$D_{a\ max}$	24 mm	
d_1	14,7 mm	
$d_{a\ min}$	12 mm	
$r_{a\ max}$	0,3 mm	
r_{min}	0,3 mm	

m	0,02 kg	Mass
C_r	4550 N	Basic dynamic load rating, radial
C_{0r}	1960 N	Basic static load rating, radial
n_G	19000 1/min	Limiting speed
n_B	0 1/min	Reference speed
C_{ur}	93 N	Fatigue limit load, radial

Figure I.1: Suspension box third rocker ballbearing specifications

Appendix J: Suspension box mainshaft ball bearing specifications

INA 61806-2Z ball bearings are used for the front and rear suspension box mainshaft. Specifications from SKF which are equal to INA are stated in figure J.1.

Principal dimensions			Basic load ratings dynamic	static	Fatigue load limit	Speed ratings Reference speed	Limiting speed	Mass	Designation
d	D	B	C	C₀	Pᵤ				* - SKF Explorer bearing
mm			kN		kN	r/min		kg	-
30	42	7	4,49	2,9	0,146	32000	16000	0,027	61806-2RZ
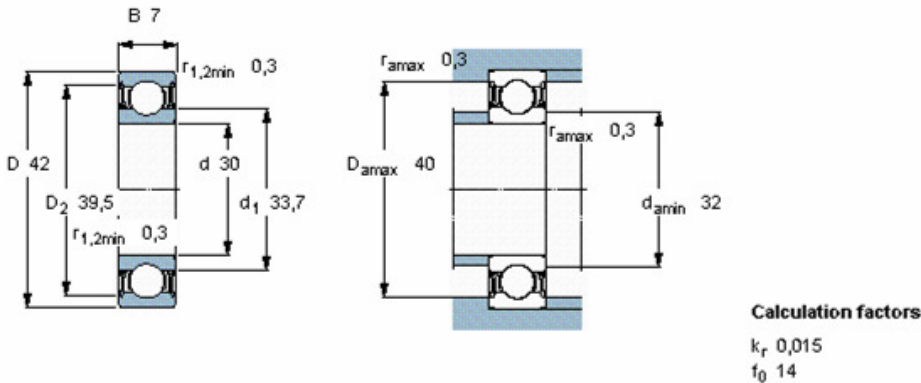
Figure J.1: Suspension box mainshaft ball bearing specifications

Appendix K: Ball monorail guidance system specifications

A ball monorail guidance system will be used for the linear translation of the third rocker in the suspension box front and rear. The monorail length is chosen minimal (100 mm). Specifications are stated in figure K.1

INA Ball monorail guidance systems KUE15
standard carriage, two-row; corrosion-resistant design possible

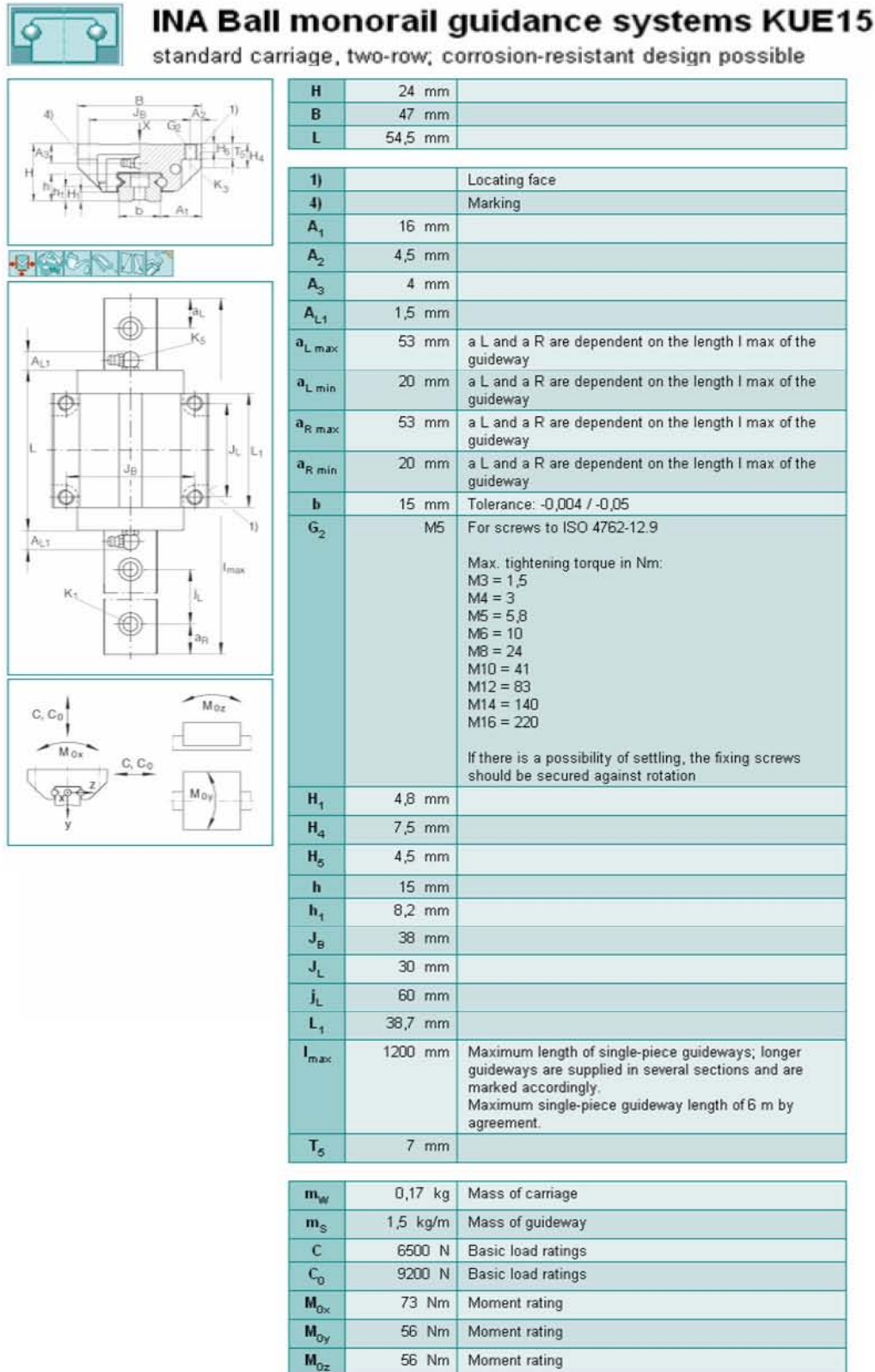|		
H	24 mm	
B	47 mm	
L	54,5 mm	
1)		Locating face
4)		Marking
A_1	16 mm	
A_2	4,5 mm	
A_3	4 mm	
A_{L1}	1,5 mm	
$a_{L\ max}$	53 mm	a L and a R are dependent on the length l max of the guideway
$a_{L\ min}$	20 mm	a L and a R are dependent on the length l max of the guideway
$a_{R\ max}$	53 mm	a L and a R are dependent on the length l max of the guideway
$a_{R\ min}$	20 mm	a L and a R are dependent on the length l max of the guideway
b	15 mm	Tolerance: -0,004 / -0,05
G_2	M5	For screws to ISO 4762-12.9 Max. tightening torque in Nm: M3 = 1,5 M4 = 3 M5 = 5,8 M6 = 10 M8 = 24 M10 = 41 M12 = 83 M14 = 140 M16 = 220 If there is a possibility of settling, the fixing screws should be secured against rotation
H_1	4,8 mm	
H_4	7,5 mm	
H_5	4,5 mm	
h	15 mm	
h_1	8,2 mm	
J_B	38 mm	
J_L	30 mm	
j_L	60 mm	
L_1	38,7 mm	
l_{max}	1200 mm	Maximum length of single-piece guideways; longer guideways are supplied in several sections and are marked accordingly. Maximum single-piece guideway length of 6 m by agreement.
T_5	7 mm	
m_W	0,17 kg	Mass of carriage
m_S	1,5 kg/m	Mass of guideway
C	6500 N	Basic load ratings
C_0	9200 N	Basic load ratings
M_{0x}	73 Nm	Moment rating
M_{0y}	56 Nm	Moment rating
M_{0z}	56 Nm	Moment rating

Figure K.1: Ball monorail guidance system specifications

Appendix L: WP steering damper measurements

The damping has been measured with the test setup shown in paragraph 6.5.3 figure 6.31. The measuring data is plotted in a graph and an exponential function is fitted through the data points. This is shown in figure M.1
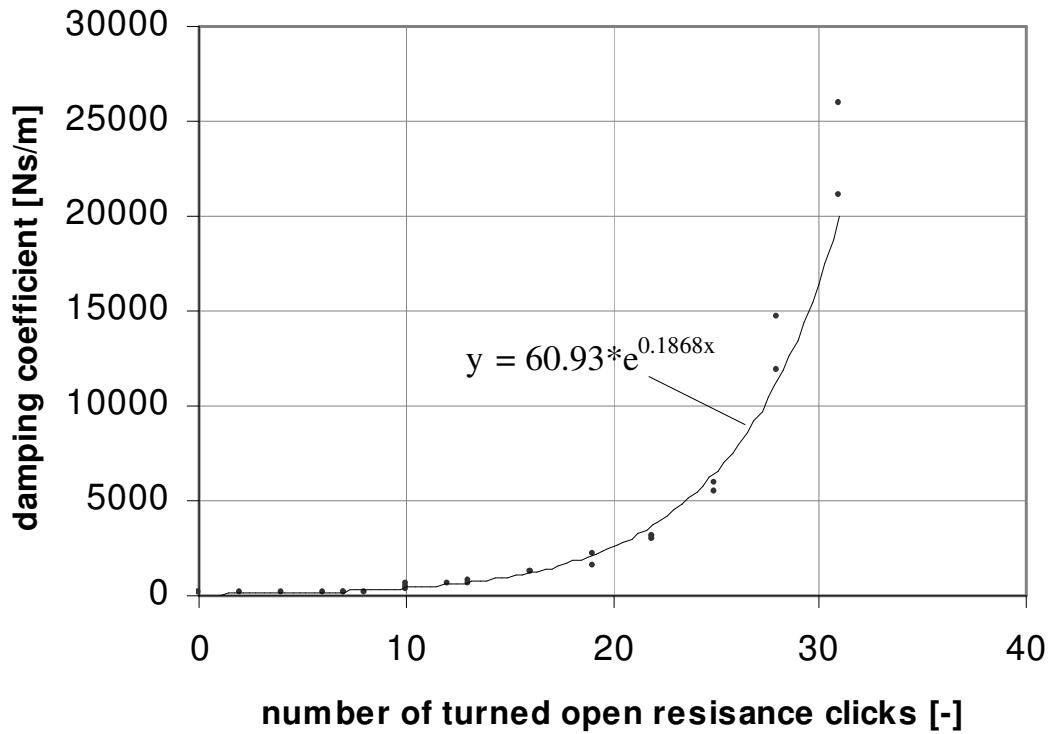
The graph shows damping coefficient [Ns/m] on the y-axis (0 to 30000) versus number of turned open resisance clicks [-] on the x-axis (0 to 40).

$$y = 60.93 * e^{0.1868x}$$

Figure N.1: WP steering damper measuring data

Appendix M: Chassis construction sequence

Table M.1 shows an overview of the building operations in chronological order.

	Action
1	Gluing the bottom seam
2	Glue in the milled rectangular tubes at the front and rear of the chassis on the ALUCORE edges
3	Glue in the rearframe
4	Glue in the frontpanel
5	Glue in the corner profiles to reinforce the bend ALUCORE edge
6	Glue in the outer insert parts using the front hoop to align them
7	Weld the square 30x30x2 mm tubes onto the inner insert parts
8	Glue in the inner insert parts with the welded on square 30x30x2 mm tubes
9	Glue in the side impact and the sloped floorpanel assembly
10	Glue on the torsion tubes
11	Place the traverse beam behind the seatpanel
12	Glue in the seatpanel
13	Place the front roll hoop
14	Assemble the dashboard by gluing in the polyurethane core
15	Glue in the assembled dashboard
16	Glue in the milled rectangular tubes for the placement of the rear and front cover plates on the ALUCORE edges.

Table M.1: Chassis construction sequence